ФИЗИКА ЭЛЕМЕНТАРНЫХ ЧАСТИЦ И АТОМНОГО ЯДРА
2010. Т. 41. ВЫП. 2

PROPERTIES OF INDIUM PHOSPHIDE AND SELECTED COMPOUNDS UNDER IRRADIATION WITH SWIFT HEAVY IONS

A. Yu. Didyk[*]

Joint Institute for Nuclear Research, Dubna

A. S. Khalil[**]

Tabbin Metallurgical Institute, Cairo, Egypt

---

[*] E-mail: didyk@jinr.ru
[**] E-mail: askhalil2004@yahoo.com

ФИЗИКА ЭЛЕМЕНТАРНЫХ ЧАСТИЦ И АТОМНОГО ЯДРА
2010. Т. 41. ВЫП. 2

PROPERTIES OF INDIUM PHOSPHIDE AND SELECTED COMPOUNDS UNDER IRRADIATION WITH SWIFT HEAVY IONS

A. Yu. Didyk,*

Joint Institute for Nuclear Research, Dubna

*A. S. Khalil***

Tabbin Metallurgical Institute, Cairo, Egypt

Surface and bulk properties of indium phosphide single crystals with initial and previously irradiated by 25 MeV electrons structures were irradiated with ^{86}Kr (253 MeV) and ^{197}Au (200 MeV) up to various fluences. The modern methods of condensed matter studies such as scanning (SEM) and high resolution transmission electronic microscopy (HTEM), Rutherford backscattering spectroscopy (RBS/C), and atomic force microscopy (AFM) were used for research of InP property changes before and after irradiation. The comparison of obtained results with the results of other authors is carried out. The surface structure change of InP single crystal irradiated by high-energy ^{86}Kr ions and electrons is studied. It is shown that the changes of the InP surface have complicated character and are caused by inelastic sputtering processes. It is observed that the twice irradiated layer swells with the cracks creation on the surface. The swelling with cracks and strong sputtering of twice irradiated by electrons and high-energy ions of the InP and GaAs surfaces layers are explained using the model based on the influence of ionizing energy loss of swift ^{86}Kr ions. The small crystalline objects are detected on the InP surface irradiated with ^{86}Kr ions which may be nano- and microcrystals of InP. All obtained effects are discussed in the frame of models based on ionizing energy loss of swift heavy ions.

Представлены результаты по изменению структуры поверхности и объемных свойств монокристаллического фосфида индия, как исходного бездефектного, так и предварительно облученного электронами с энергией 25 МэВ, после облучения ионами ^{86}Kr (253 МэВ) и ^{197}Au (200 МэВ) до различных флюенсов. Для исследования изменений были использованы современные методы физики конденсированного состояния, такие как сканирующая электронная (СЭМ), атомно-силовая (АСМ) и просвечивающая микроскопии высокого разрешения (ПЭМ), а также резерфордовское обратное рассеяние (РОР). Проведено сравнение полученных результатов с данными других авторов. Исследования изменений структуры поверхности монокристалла InP, облученного ионами ^{86}Kr высокой энергии и электронами, показали, что изменения поверхности InP ионами носят сложный характер и обусловлены процессами неупругого распыления. Обнаружено, что двукратно облученные электронами и тяжелыми ионами высоких энергий слои InP и GaAs распухают с образованием трещин и разломов на поверхности. На облученной поверхности обнаружены отдельные монокристаллы, по-видимому, представляющие собой нано- и

---

[*] E-mail: didyk@jinr.ru

[**] E-mail: askhalil2004@yahoo.com

микрокристаллиты InP. Обнаруженные эффекты в InP после облучения обсуждены с применением моделей, основанных на роли ионизационных и ядерных потерь энергии тяжелых ионов высокой энергии.

PACS: 34.50.-S; 61.80.Lj; 61.80.-x

INTRODUCTION

Indium phosphide is an important III–V semiconductor compound, with a variety of applications, for example, in light emitting diodes (LED), in photonic crystals and in semiconductor lasers, heterojunction bipolar transistors in integrated circuit applications and in transistors for microwave and millimeter-wave systems. The optical and electrical properties of this semiconductor crystal can be further tailored by ion implantation or by swift heavy-ion beam irradiation.

Unique properties of nanometer structures such as quantum dots, wires and so on have attracted a great interest for some decades [1, 2]. One way of nanometer structuring of solids is swift heavy-ion irradiation. Under the definite conditions, it creates an ion tracks system in the form of narrow cylinders or nanometer cluster chains with modified structure embedded into undamaged matrix. The study of interaction of swift heavy ions with semiconductor single crystals is very important both for the fundamental investigations of radiation effects in condensed matter and for the creation of ion tracks in semiconductor materials, which can be used in modern nanotechnologies of electronics [3–6].

Thus knowledge of ion-induced disorder in this material is of important fundamental and practical interest. However, the disorder produced during swift heavy-ion irradiation and the subsequent damage accumulation is far from being completely understood. In terms of the damage accumulation mechanisms, the conclusions drawn in the numerous studies performed have often been in conflict with one another. A factor contributing to the uncertainties associated with these conflicting results is a lack of information and direct observation of the «*building blocks*» leading to the ultimate damage created at high ion fluences as an amorphous layer. These «*building blocks*» formed at lower fluence regimes by single ion impacts can be directly observed as isolated disordered zones and ion tracks for low-energy and swift heavy-ion irradiation, respectively.

The main purpose of this review is to present last experimental results of swift heavy-ion action on InP complex semiconductor and related materials through investigations of ion track and damage creation with the use of Scanning (SEM) and High Resolution Transmission Electron Microscopy (HRTEM), Rutherford Backscattering Spectrometry (RBS/C) and Atomic Force Microscopy (AFM).

Ion tracks due to swift heavy-ion irradiation were observed in this material and the interesting track morphology was described and discussed. The surface nanotopographical changes due to increasing fluence of swift heavy ions were observed by AFM where the onset of large increase in surface roughness for fluences sufficient to cause complete surface amorphization was observed.

1. SWIFT HEAVY-ION IRRADIATION OF InP. SHI DAMAGE AND ION TRACKS: DESCRIPTION OF TRACK FORMATION

The energy loss of swift heavy ions (SHI) can be presented and separated on two parts: inelastic energy loss of ions S_{inel} and elastic energy loss S_{el}. Inelastic energy loss is the direct energy transfer to electrons by scattering of ions on electrons of solids, and elastic energy loss is the ion energy transfer by elastic scattering of ions on lattice atoms.

The energy loss along an ion trajectory leads to a very local and very high excitation of the lattice atoms [14, 15]. Figure 1 illustrates a schematic of the

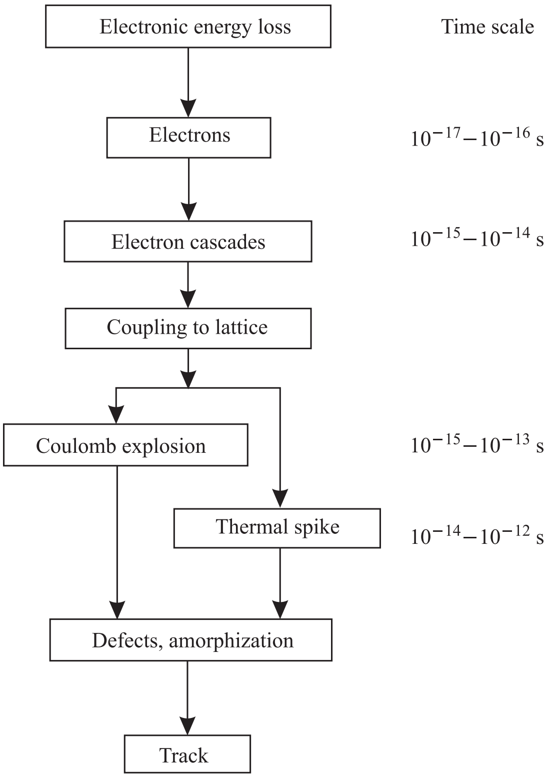

Fig. 1. Schematic representation of the extreme short temporal development of processes which might lead to ion track registration in solids

temporal development of such processes. In the case of SHI irradiation, elastic energy loss of ions becomes only about a few per cent (2–10%) from the total ion energy, and the energy loss of ions is practically almost transferred to target exclusively by electronic excitation or ionization of the electron system of the target atoms [16].

Thus, in general, when a SHI enters a solid, it may produce the so-called heavy ion track with an approximate cylindrical geometry, which will have another electrical, chemical and structural properties than balk target sometimes due to the large electronic excitations which *may* result in ion-track registration. Figure 2 pictorially depicts what is thought to be a highly excited cylinder around the SHI trajectory immediately following SHI penetration into matter. TEM observations of individual ion tracks clearly prove that defects giving rise to the tracks can result from the high electronic excitation energy deposition; part of this high

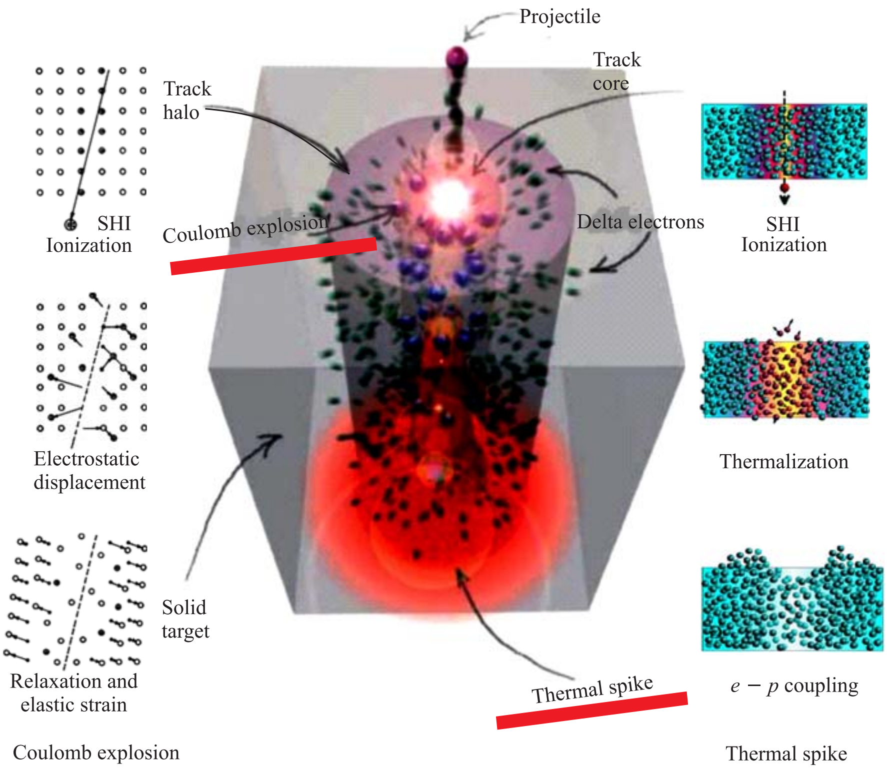

Fig. 2. A pictorial representations of the highly excited cylindrical region created immediately along the SHI trajectory through a medium which may lead to ion track registration. Also schematics of both Thermal Spike and Coulomb Explosion are presented

electronic excitation is transferred into kinetic energy of the target atoms and atomic additional motion which give rise to a defect rich region and frequently the registration of a latent ion track. Such behavior previously has been explained by essentially two different models: the *Thermal Spike* [17–21] and *Coulomb Explosion mechanisms* [22, 23]. In Fig. 2. schematic representation of these two models is also shown.

In the Thermal Spike model [15, 17–21], cooling (thermalization) of the electronic system within approximately $\sim 10^{-12}$ s is assumed, i.e., the transition of the electron energy distribution from Fermi–Dirac statistics towards Maxwell–Boltzmann statistics. In several picoseconds, electrons will equilibrate their energy with the nuclei by electron–phonon (e–p) scattering which results in heating of the lattice and the generation of a Gaussian-like temperature profile around the ion trajectory, leading to transient atom temperatures of the order of several 1000 K lasting for several 10^{-15} s [5].

The energy transfer process from excited electrons is usually described by two coupled equations [5] expressing the energy transfer from the hot electron subsystem to the atomic lattice subsystem of the crystal, considering the electron gas and the atomic lattice as *continuous* media. This energy-transfer process from excited electrons to the lattice depends on the coefficient of electron–phonon interaction g [5–8], which is inversely proportional to the square of the mean free path λ of the electrons, the only free parameter invoked in this model, while macroscopic thermodynamical parameters intrinsic to the target material are used to calculate the heat transfer. The spike temperature into swift heavy ion track mainly depends on this coefficient of electron–phonon interaction. If the electronic energy deposition density is sufficiently high, the temperature may rise above the melting point and a molten cylinder several nanometers in diameter can be formed.

After several tens of picoseconds, rapid quenching (quenching rates of $\sim 10^{13}$–10^{14} K/s) of the melt to the ambient temperature may result in the formation of an amorphous track if the rate of resolidification exceeds that of recrystallization. However, imperfect recrystallization can result in the formation of a track consisting of a defect-rich disordered but not amorphous material [24].

On the other hand, for the case of SHI irradiation, Thermal Spikes are regarded to be high aspect ratio zones of highly concentrated electronic energy transfer along the trajectories of ions, this leads primarily to extremely high electron temperatures (typically of the order of several times 10^3 up to 10^4 K), and at a later stage due to e–p coupling to still high atomic temperatures of typically several 1000 K. The original concept of Thermal Spike and its underlying mechanisms (e.g., the e–p coupling and lattice relaxations) are based on thermodynamic considerations assuming a thermal equilibrium [25].

Another mechanism, which may stem from the Thermal Spike and which is sometimes overlooked, is plastic deformation due to the high pressure on the material surrounding the ion path [9, 10, 26]. Indeed, heating of the track core material, after electrons transfer their energy to the lattice, results in thermal expansion and an associated stress field from a transient pressure spike [26].

The Coulomb Explosion model [22, 23] is based upon the assumption that the hot electrons can leave the volume around ion trajectory and electrostatic repulsion occurs between the positively charged remained atoms along the ion path. And as a result, an explosion-like atomic motion overcomes the local atomic bonding and propagates in explosive manner radial from the ion path imparts large kinetic energy to the surrounding lattice atoms and thus displaces them from their normal lattice sites. This in turn leads to the formation of a core with strongly reduced atomic density surrounded by a densified shell. Since this is not a stable state, the dense region collapses back into the central core and, in the absence of recrystallization processes, generates a heavily perturbed or even amorphous latent track of several nm in diameter. Another approach is the lattice relaxation model which may be regarded as a combination of both Thermal Spike and Coulomb Explosion models, where the intense electronic excitation weakens the covalent bonds and causes a repulsive force between atoms, resulting in collective atomic rearrangement and track formation [16, 27]. Track formation in insulators has generally been explained with the Coulomb Explosion approach due to the fact that there are no free electrons to compensate for the transitory build up of positive charge after the passage of SHI in an insulator. This seems to be supported by a number of experiments [22, 23, 28]. Tracks in semiconductors, which typically have chemical bonds with relatively low multiplicity [29], have been attributed to the formation of thermal spikes [30]. However, the exact processes following SHI irradiation of semiconductors are generally unclear [31].

In a review by Miotello and Kelly [32], a detailed discussion of difficulties associated with using the thermal spike approach to describe the formation of latent tracks in solids under SHI bombardment has been given. They pointed out that due to large kinetic energies of inner-shell electrons excited by a SHI, a large part of the energy deposited by the ion is carried away from the ion track volume and dissipated over larger distances, not confined by the ion trajectory. Nevertheless, despite these difficulties, insight may be gained from investigation of the key parameters of practical interest including the following:

(i) Threshold values of the stopping power required for track registration.
(ii) Track diameter.
(iii) Defect structure inside the track.
(iv) Track morphology.

As many studies have observed tracks in different kind of materials, it is assumed that track formation only occurs if a material-dependent threshold $S^{\mathrm{th}}_{\mathrm{ioniz}} = -(dE/dx)^{\mathrm{th}}_{\mathrm{ioniz}}$ of electronic stopping is exceeded, where the superscript (th) refers to the threshold value of electronic energy deposition. Near $S^{\mathrm{th}}_{\mathrm{ioniz}}$, discontinuous tracks of irregularly separated small spherical volumes may be observed. These spheres elongate with increasing deposited energy density and finally tracks are formed [33]. Nevertheless, the conditions of track formation and the inner structure of tracks in different materials differ substantially.

Several studies developed criteria which could predict the threshold values for energy deposition required for track formation in different materials [34, 35]. Attempts were made to correlate the efficiency of track formation with several fundamental parameters of the solid, such as the band gap, multiplicity of chemical bonds, thermal conductivity, etc. [36]. However, none of these attempts can adequately or universally explain the influence of fundamental material parameters on track formation in different crystalline materials.

For a long time the Thermal Spike and Coulomb Explosion models were regarded as competing and contradicting models to describe ion-track formation. In spite of many clever discussions, a final decision could not be brought about through experimental evidence, as both models predict a square dependence of the damage cross sections on $S_x \equiv -(\partial E/\partial x)_{\rm ioniz}$. Furthermore, both models have their disadvantages. For example, in the Coulomb Explosion model the possibility of quenching of this effect in its very initial stage by the rapidly returning electrons was never treated in a convincing way, while the Thermal Spike model neglected both surface pressure and shock wave effects and phase changes, which made its unconditional application doubtful [14, 25].

Track registration phenomenon represents a multifaceted, very complex process. The absence of tracks in certain materials, and their size/morphology/structure in others suggests that phase transformations are important, but simple target amorphization is the exception and not the rule in track registration phenomena [37]. As noted in this work; a simple melt model of the Thermal Spike or the radial motion of the Coulomb Explosion model cannot account for the multitude of observed track effects in different materials, and especially in semiconductors.

This suggests that these models no longer compete but instead a composite of both models may be more realistic, i.e., a «compound spike» may account for the active processes. It has also to do with defects and their dynamics. Since some materials were found to be insensitive to track registration while others can register tracks following the same conditions of SHI irradiation. A model of projectile assisted prompt anneal (PAPA) in times of the order of $\sim 10^{-11}$ s, either partial or complete, and often by a very rapid *in-situ* homoepitaxial recovery was proposed [37]. This process may depend on defects specific to the target on either elemental or compound sublattices of the material. This may further point to the central role of atomistic characteristics of the target, i.e., the point defects, their motion and interaction, stability and the electronic band structure unique to every target, for the determination of the resultant track detail.

It is more important to note that both the Coulomb Explosion and Thermal Spike models were developed especially for dielectrics or for solids with high level of defects of various origin.

1.1. Ion Tracks in SHI Irradiated Elemental and Compound Semiconductors: Direct TEM Observations. Regardless of the details of the track formation mechanism, it is clear that the track consists of a tapering defect-rich cylinder, i.e., high aspect ratio region of atomic disorder embedded in otherwise perfect lattice. Associated with this disorder is a radial strain field. It is the radial strain field which provides the diffraction contrast in the image of tracks in crystalline material, as electrons are scattered from the transmitted beam as they pass in the vicinity of the track. Thus tracks generally appear as features of dark contrast with a radial symmetry on a light background when the thin crystal is viewed in BF TEM mode [38].

Surprisingly, no tracks have been found in SHI irradiated easily amorphizable elemental semiconductors (by the conventional low energy heavy-ion irradiation) such as Si or Ge [39, 40]. Nevertheless, formation of amorphous tracks was observed in Si [41, 42], Ge [43], and GaAs [44] bombarded with 20–40 MeV C_{60} cluster ions (fullerenes).

The absence of tracks in the case of SHI irradiations may be explained by the differences in damage production between 30–40 MeV fullerene and SHI irradiation regimes. Factors such as the total electronic energy loss, the great difference in the velocities of SHI and C_{60} ion clusters for the same energy loss, and the very limited range of the delta electrons (electrons which move away radially from the ion path after intense ionization) in the case of cluster irradiation, can greatly localize the energy around the cluster path [45]. In this context we have to mention that other investigators reported track formation under specific conditions in Si and Ge by SHI [46] but the samples were either extremely thin films of ~ 5 nm thickness or were amorphous thin films obtained by vacuum evaporation.

For the case of compound semiconductors, SHI-induced lattice damage and track formation have been observed by TEM over a broad range, including InP, InSb, GaSb, InAs, GeS, SiGe, GaAs, and GaN [11, 30, 31, 34, 47–50].

However, no tracks were observed in GaP [51, 88]. Ion tracks in several compounds such as InP, GaSb, and GeS [34, 49, 52] were reported to contain an amorphous core, as in the case of many insulators [36]. In semiconductors such as InSb and GaN [34, 47], track cores consist of disordered but not amorphous material.

Cross-section TEM (XTEM) investigations of InP single crystals irradiated by 250 MeV Xe ions [52–55] showed that basically two zones of damage are formed by the impinging SHI as illustrated in Fig. 3.

The observed defects were correlated with the energy losses of the 250 MeV Xe ions in the crystal giving rise to both ion tracks from electronic energy loss and defect clusters from nuclear energy loss near the end of range.

The first zone (regions: I–III) extends down to $\sim 10\ \mu$m and contains defects in the form of latent tracks of diameters $\sim 7-15$ nm; from SADP the

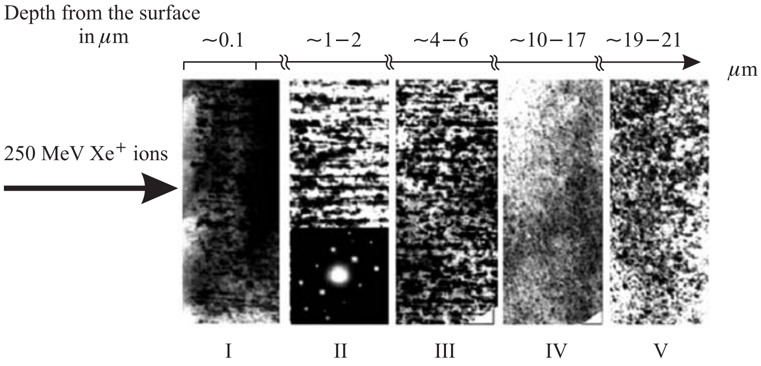

Fig. 3. XTEM micrograph of InP irradiated by 250 MeV Xe at $7.0 \cdot 10^{12}$ cm^{-2} showing defect structures at different depths from the surface, and the observed type of defects: Areas 1–V correspond to: I) slightly damaged layer at the top ~ 0.035 μm in depth and then discontinuous ion tracks starting from depth ~ 0.1 μm; II–III) ion tracks in the form of straight lines of dark contrast to depth ~ 10 μm. The inset in II is the corresponding selected area diffraction pattern (SADP) of that region; IV) a band of damaged region containing agglomerates of small point defect clusters; V) a band of heavily damaged region at the end of range, containing agglomerates of amorphous and crystalline material which coincides with the maximum nuclear energy deposition of the irradiating ions

authors concluded that these tracks are amorphous. These tracks are continuous at depths ranging from $\sim 0.1{-}7.0$ μm and then discontinuous in depth range of $\sim 7{-}10$ μm. Tracks are also discontinuous and consist of a chain of spherical defects located at $\sim 0.035{-}0.1$ μm from the surface. One interesting observation is the slightly damaged top layer near the surface at depths of $\leqslant 0.035$ μm. The second zone (regions: IV–V) consists of a band of damage containing small defect clusters 10–17 μm in depth and then a heavily damaged band which almost coincides with the position of the maximum of the nuclear energy deposition as calculated by TRIM simulations (near the end of the ion range). This heavily damaged zone is a mixture of crystalline and amorphous InP and extends from $\sim 19{-}21$ μm in depth. Another observation was that the track density and ion fluence differed by approximately one order of magnitude ($\sim 2.0 \cdot 10^{11}$ cm^{-2} versus the irradiating ion fluence of $7.0 \cdot 10^{12}$ cm^{-2}). Also, with fluences lower than $5.0 \cdot 10^{12}$ cm^{-2}, no tracks were observed in InP and only small defects and clusters were detected.

Based on the Thermal Spike model and the above observations, it has been suggested that the critical (threshold) value of electronic energy loss for track formation in crystalline InP is ~ 13 keV/nm. The difference between the observed track density and the ion fluence was explained by the accumulation of defects created by a certain incubation fluence that modify the surrounding matrix, which in turn affects the process of quenching and subsequent imperfect resolidification of the melted region surrounding the ion path to form a track.

Irradiation of InP at both low (80 K) and high (400 K) temperature suppressed the formation of tracks. In the case of irradiation at 80 K this was attributed to greater thermal conductivity of InP at lower temperatures which promotes a rapid dissipation of the generated heat and hence suppression of track formation. For irradiation at 400 K the absence of tracks has been attributed to the process of dynamic recovery of the initially SHI generated point defects during irradiation and their subsequent rearrangement to more stable extended defects [31, 52–55].

Komarov et al. [55–59] explained the discontinuous nature of tracks which appeared as dot-like string of defects in these experiments. The fluctuation of the ion charge state upon entering the target depends on the number of captured or lost electrons during ion passage. There are statistical increases and decreases in the electronic energy deposition by several keV/nm around the threshold value $-(dE/dx)^{\mathrm{th}}_{\mathrm{ioniz}}$ of $\sim$ 13 keV/nm. This in turn determines the creation of defects along the ion trajectory and the length of registered defective regions along the trajectory and the separation distances between such regions.

HRTEM of tracks [30, 55] revealed that 250 MeV Xe ion irradiation generates defects around the ion path. Even in the absence of an amorphous core, defects such as microtwins, stacking faults and dislocation loops were observed near the tracks. Amorphous cores and Wurzite phase nanocrystals have been reported inside the cores of several tracks which were attributed to an intense pressure spike during the transitory formation phase of the track [30, 60, 61].

1.2. Ion Track Registration in InP. In the course of our investigations, ion tracks were observed in 200 MeV Au ion irradiated InP. The observed defect-rich regions were delineated by sharp contrast of circular features superimposed on unperturbed matrix as shown in the BF TEM image in Fig. 4, *a*. This observed TEM contrast is due to the large radially symmetric strain field $u(r)$ usually associated with the track core which can be generally expressed as:

$$u(r) = E_{\mathrm{eff}}(R^2/r), \tag{1.1}$$

where E_{eff} is the effective strain which depends on the elastic constants of the material and R is the assumed *radius* of the track [38, 62]. In addition to the sharp contrast of each track relative to the surrounding matrix as shown in Fig. 4, *b* for higher magnification TEM, it also shows that the density of the tracks $\sim 5.2 \cdot 10^{10}$ cm^{-2} which generally agrees with the irradiation fluence of $\sim 5.0 \cdot 10^{10}$ cm^{-2}, as measured by charge integration during SHI irradiation, also by observations of hole density in samples of the MoO_3. By tilting the sample with respect to the illuminating electron beam to $\sim 30°$, we were able to reveal the lengthwise track morphology (i.e., along the ion trajectory and not only perpendicular to it, so we can obtain almost complete information 3D about the

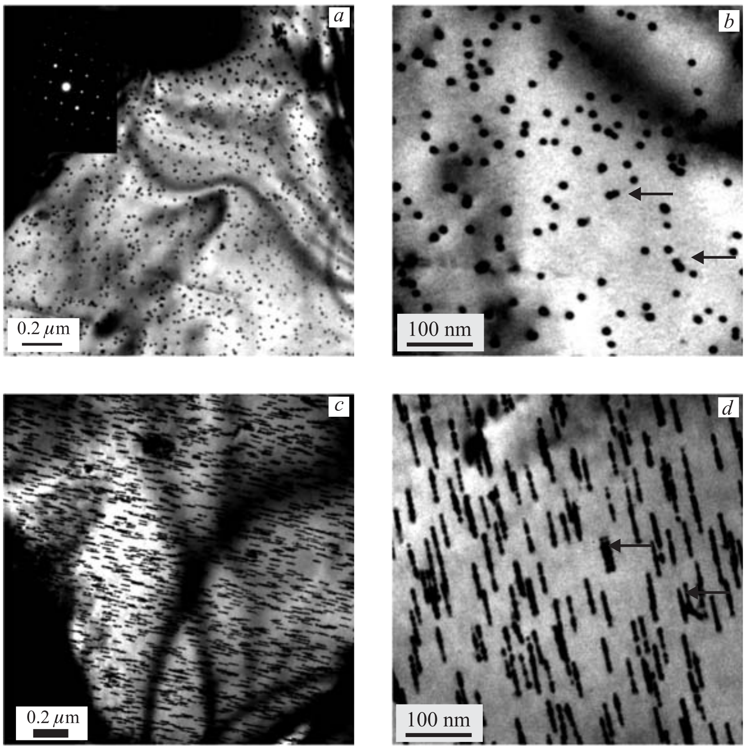

Fig. 4. BF TEM images of tracks in a thin foil InP irradiated with 200 MeV Au ions to fluence of $5.0 \cdot 10^{10}$ cm^{-2}. Tracks are shown at two different magnifications in plots *a* and *b*. The inset in *a* is the selected area diffraction pattern (SADP) of the corresponding imaged area. Arrows in micrograph *b* point to track overlap even at this relatively low fluence. And *c* is an ensemble of many tracks as revealed lengthwise by tilting the sample $\sim 30^\circ$ with respect to the imaging electron beam. Plot *d* gives closer observation of the interesting morphology of the tracks, comprising strings of nanospheres (arrows point to what is perceived as overlap when the sample is not tilted and what might be a *relic* of a scattering event during irradiation)

tracks rather than only observing the cross sections of the tracks). Tracks found to consist of beaded strings or nanospheres of disorder (see in Fig. 4, *c* and for closer view in Fig. 4, *d*).

In Fig. 5 the measured ion track diameters from micrograph with an area of 550×550 nm such as in Fig. 4, *b*, are shown. Here it should be mentioned the straightforwardness of track diameter determination relative to the disordered zones size determinations, because of the well defined track borders in addition to the stronger uniform contrast arising *equally* from *all* the observed tracks.

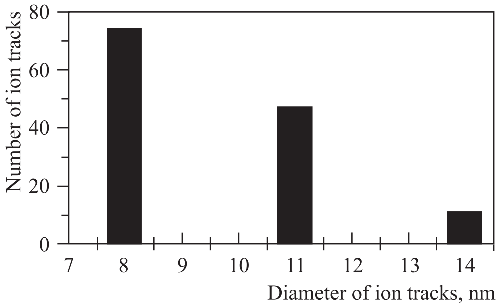

Fig. 5. Measured track diameters in 200 MeV Au ion irradiated InP, at a fluence of $5.0 \cdot 10^{10}$ cm^{-2}

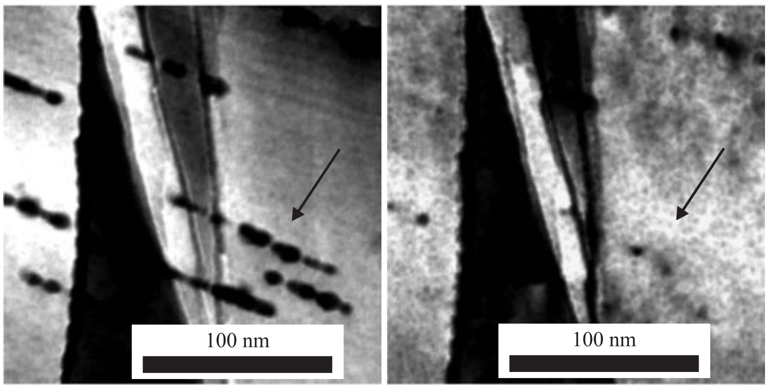

Fig. 6. Track disappearance under prolonged 300 keV TEM observation

During TEM observations it was found that the tracks are sensitive to the electron beam. They tend to fade away (anneal) with a loss of contrast and eventually disappear upon prolonged TEM observation (Fig. 6). HRTEM observations at low temperature (liquid nitrogen) to be discussed later confirmed that observation. Therefore the illuminating electron beam has to be well spread and it is necessary to move to different areas of a sample in order to obtain an informative image before the track fading. This fading behavior may be attributed to the electron beam-induced annealing of tracks similar to the low energy disordered zones created by 100 keV Au observed earlier in InP. Similar observations of fading under prolonged observation in TEM have been reported without explanation for 1.85 MeV/nucleon Pb ion irradiated InP [34].

Now, it should be emphasized here that the impact of 200 MeV Au ions onto a target is a natural statistical process at the nanometrical level. The tracks follow Poisson distributions for the probabilities of i-fold ion-track overlapping with $i \geqslant 0$, where $i = 0$: no track, $i = 1$: individual tracks, $i = 2$: double ion-track overlapping. A given unit area of the target may be hit once, twice or even multiple times, or not at all.

For a certain ion fluence F (and hence the areal track density), the probability to find individual W_1, double W_2 impacts in the unit area is given by [63]:

$$W_1 = \exp(-\xi), \tag{1.2}$$

$$W_2 = \xi \exp(-1.185\xi). \tag{1.3}$$

Here $\xi = 4P$, with $P = \sigma_t F$ being the total area covered with tracks without taking into account track overlapping; $\sigma_t = \pi \times r^2$ is the cross-sectional area of an individual track, and F is the ion fluence. For the lowest value of $P = \sigma_t F$, the unirradiated areal fraction dominates, followed by some areas with individual ion tracks. With increasing $\sigma_t F$, the unirradiated fraction vanishes, and the areal fraction of individual tracks reaches its maximum. At the same time, the first unit areas with double and even triple overlapping tracks are expected. With increasing fluence the fraction of individual tracks decreases and double overlapping tracks can reach their maximum in non-negligible fractions, and triple or more overlapping tracks are found. According to Eqs. (3.2) and (1.3), the ratio W_2/W_1 will increase by one order of magnitude for each ten-fold increase in irradiating 200 MeV Au ion of InP. And it should be noted that each ion does indeed registers a track in the InP lattice. This is clearly confirmed by comparing the irradiated sample to simultaneously irradiated $\mathrm{MoO_3}$ crystallites. However, even at the lowest fluence of $5.0 \cdot 10^{10}$ cm^{-2}, there exists a finite probability for observation of track overlap. These overlapping events are pointed by the arrows in Fig. 4, *b*. The arrows point to double overlapping (two track overlaps). However, one-to-one correspondence was always found between ion fluences and track densities (see Fig. 7) where areas of irradiated InP are selected and compared with similar areas of $\mathrm{MoO_3}$ irradiated simultaneously by 200 MeV Au ions.

Consequently, an interpretation based on the thermal spike was proposed from previously reported TEM observations [31, 52–55] of tracks in InP in order to account for the discrepancy between the ion density of tracks relative to the ion fluence (tracks were less than ion fluence by a factor of ~ 100). In this interpretation each single ion creates not a track but only point defects and/or clusters of defects. Therefore in order to form a track it was assumed that the ion must impact a predamaged area with already existing point defects (i.e., an imperfect InP lattice), i.e., there exists a critical primary concentration of defect centers, necessary for track formation in InP, as defect-rich area can then impede the perfect recrystallization front of the molten region surrounding an ion path. When further ions impinge on these imperfect defect-rich areas, the recrystallization of the molten core may be hindered because the surrounding

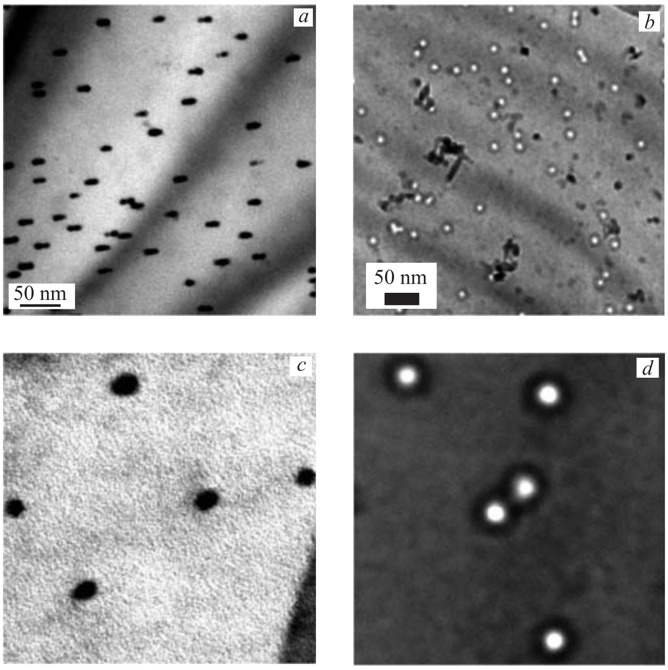

Fig. 7. *a*) BF TEM of ion tracks in $5.0 \cdot 10^{10}$ cm^{-2} irradiated InP sample slightly tilted with respect to the illuminating electron beam, *b*) holes in MoO$_3$ crystallite for the same irradiation fluence, *c*) representative area — element of unit area or can be considered as the most probable *picture* for that fluence — area of 100 × 100 nm for InP, and *d*) 100 × 100 nm area in MoO$_3$. Agreement between ion track density and the SHI ion fluence indicates that each ion creates a track in InP

crystal is now less perfect. Thus, ongoing irradiation leads to defect accumulation and the recrystallization speed may become smaller than the resolidification speed, leading to a freezing-in of a continuous *amorphous* track [54]. An incubation fluence of $\geqslant 2.0 \cdot 10^{10}$ cm^{-2} was to be claimed necessary for SHI track formation in InP.

Another assumption, set forth by Szenes et al. [34], was that the *threshold energy* $S^{\rm th}_{\rm ioniz} \equiv -(dE/dx)^{\rm th}_{\rm ioniz}$ for track registration in InP can be lowered due to the introduction of predamage. Disorder can modify the electronic properties of the material and thus the value of the $e-p$ coupling factor «g». Our observations contradict both assumptions, since each impinging ion forms a track in a pristine InP thin foil sample. Any need for predamaging in the formation of tracks in InP is therefore excluded.

1.3. On the Track Morphology in InP. Many tracks in InP appeared as strings of beads of defects or nanospheres (see Fig. 4, *d*). Each track consists of $\geqslant 4$ nanospheres of disorder with regular spacing. Other tracks showed the same pattern but with a larger spacing between the beads. The exact nature of defects inside the tracks (nanospheres) cannot be revealed by RBS/C, TEM or HRTEM. SADP did not reveal the presence of diffuse halos characteristic of any amorphous phase for samples irradiated at fluences of $5.0 \cdot 10^{10}$ cm^{-2}. This is most probably due to the fact that there is an insufficient volume fraction of tracks in the material and/or that tracks are not amorphous. However, in the SADP for $1.0 \cdot 10^{13}$ cm^{-2}, where extensive overlap of tracks is expected, some crystallinity is still preserved as indicated by the appearance of diffraction spots synonymous with crystallinity (shown later in Fig. 22, *b*).

We now proceed to discuss factors which may give rise to the peculiar of the beaded track morphology, these can be the following:

1.3.1. Phenomenological Model for Track Morphology (Threshold Energy of Track Formation). The observed morphologies of tracks in different SHI irradiated materials have been discussed in many works based on RBS/C investigations in SHI irradiated magnetic insulators and oxide materials [33, 64, 65]. Let us introduce values $S_x \equiv -(\partial E/\partial x)_{\text{ioniz}}$ and $S_{\text{ioniz}}^{\text{th}} \equiv -(dE/dx)_{\text{ioniz}}^{\text{th}}$. In these works, observations of the dependence of track morphology on the electronic energy deposition S_x lead to a proposed phenomenological description of track morphology as identified from plots of the *effective radius* of tracks determined by RBS/C as a function of S_x. Basically four characteristic morphologies were characterized as shown in Fig. 8. First, at low values of S_x, there is the formation of spherical defects along the ion path which corresponds to the case where electronic (inelastic) energy deposition starts to prevail over the nuclear energy deposition (*regime* II).

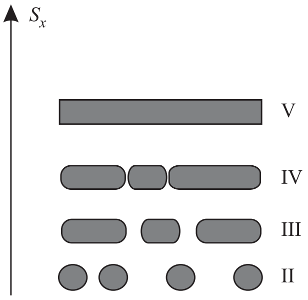

Fig. 8. Development of SHI tracks morphology versus electronic energy loss S_x according to the above-discussed phenomenological model for track formation

Then with increasing S_x these spherical defects start to overlap, giving rise to elongated segments of defect-rich regions along the ion path but still forming discontinuous tracks (*regime* III). These segments in turn start to overlap with increasing S_x to form segmented cylindrical tracks (*regime* IV), which in turn form continuous cylindrical tracks where the damage is homogeneous when S_x exceeds a critical value for most investigated materials [33, 64, 65] (*regime* V). In these studies it is also noted that, for equal values of S_x, the estimated damage cross section was larger for low (1–2 MeV/amu) compared to high (10–12 MeV/amu) ion velocities. This so-called «velocity effect» takes into account not only the electronic energy loss but the fact that there are two ion velocities for the same stopping power around the Bragg peak, and therefore different energy densities. The appearance of the velocity effect under constant S_x is probably related to the radial distribution of the initial energy deposition and/or the energy sharing within the electron system which in turn can affect the observed damage cross sections for the same S_x but different ion velocities [66].

1.3.2. The Charge Fluctuation Model (Komarov's Model for Beaded Tracks). To explain track morphology in SHI irradiated semiconductor materials in general, and particularly in InP, Komarov et al. [30, 59, 67] proposed a model which can arise from primary processes related to the statistical fluctuation of the ion charge state moving inside a solid due to the electron stripping and capture processes [68].

As a SHI penetrates a crystal, the elastic energy loss plays a minor role and most of the energy ($> 90\%$) is lost in inelastic collisions with electrons. The electronic energy loss in solids is described by the well-known Bethe's formula [59]:

$$S_x = -\left(\frac{\partial E}{\partial x}\right)_{\text{ioniz}} = \frac{4\pi Z_2 Z_{1,\text{eff}}^2 \, e^4 N}{mV^2} \ln \frac{2mV^2}{I}, \qquad (1.4)$$

where $Z_{1,\text{eff}}$ is the average effective ion charge; Z_2 and N are the atomic number and atom density of the target, respectively; e and m are the electron charge and mass; V is the ion velocity and I is the average ionization potential of the target atoms.

The ion loses part or all of its electrons within the first few nm upon impact onto matter, and it maintains only those electrons whose orbital velocity exceeds the ion velocity inside the matter. Thus, the ion acquires an effective charge that is described by the empirical relation [26]:

$$Z_{\text{eff}} = \gamma Z_p, \qquad (1.5)$$

where $\gamma^2 = 1 - \exp\left(-125\,\beta/Z_p^{2/3}\right)$ and Z_p is the original ion charge; and $\beta = V/c$, where V is the ion velocity and c is the speed of light.

The numerical integration of Eq. (1.4) gives a dependence of the inelastic energy loss on depth. According to this equation even a small fluctuation of the effective charge of a penetrating ion can cause a considerable change in energy deposition. However, the role of these processes becomes noticeable when the energy of the ion is close to the threshold value $S_{\text{ioniz}}^{\text{th}}$of the mean energy loss required for track formation (i.e., $\sim$ 13 keV/nm in InP).

Therefore, according to Komarov [30, 59, 67], the discontinuous tracks observed in TEM can be caused by *statistical fluctuations during charge exchange*, when an ion loses one or several electrons and the value of S_x becomes greater at a certain part of the ion path than the value of $S_{\text{ioniz}}^{\text{th}}$ required for the track registration. When $S_x > S_{\text{ioniz}}^{\text{th}}$, a continuous segment of track is registered, thus track registration generally is determined by the charge state. This determines both the length of the observed defect region in a discontinuous track and the intervening distance between the defect regions. The diameter of the defect created and its geometry is determined by the number of stripped electrons. For example, the loss or capture of one electron results in oscillations of $\sim 8\%$ of energy loss, i.e., $S^{\rm th}_{\rm ioniz}(q_{\rm max}/q_{\rm min}) \approx 1.08$, where $q_{\rm max}$ and $q_{\rm min}$ are the ion charge after the charge exchange with the electron loss or capture, respectively, whereas the loss or capture of three electrons causes even greater oscillations of $\sim 30\%$. This arises from the square of the effective charge dependence of the energy loss in solids (see Eq. (1.4)). The probability of charge-exchange processes for the ion penetrating a material mentioned above is [60]:

$$P(x) = N_a \sigma_{\pm} x, \tag{1.6}$$

where P is the probability of the process at a depth x; N_a is the atomic density in the target and $\sigma_{\pm}$ is the probability of electron capture or loss. Hence the length of the defect region in discontinuous track can be defined by $\lambda = 1/N_a\sigma_{\pm}$ [59].

However, it should be noted that near the surface ($\sim$ several nm) the ion charges within the ion flux distribution have yet to reach equilibrium till charges acquire the effective charge (this was the account given [32] for the absence of defects at $\leqslant 0.035$ μm in 250 Xe ion irradiated InP as shown in Fig. 3). The mechanism responsible for the discontinuous nature of a track may potentially operate deeper inside the irradiated material from the surface as the probability P for charge-exchange process is directly proportional to the distance traversed by the ion inside the material. This may occur deeper in the material as the ion loses its energy till S_x reaches a value equal to or smaller than the $S^{\rm th}_{\rm ioniz}$ for track formation so that discontinuous tracks registration can take place [32].

Thus, the relative probability for multielectron charge-exchange processes with a SHI, compared to one-electron charge exchange processes, is about 60% for the loss or capture of two electrons, 40% for three-electron processes, 20% for four-electron processes and so forth [68]. TEM observations by Gaiduk et al. [52] on 250 MeV Xe irradiated InP [69] showed that there are continuous track regions at depths 0.1–7.0 μm. However, the intermittent tracks observed as a chain of spherical defects at depth $x \geqslant 7$ μm to a depth of 10 μm may be due to the very phenomenon of statistical charge exchange we have explained. For those trajectory segments for which $S_x > S^{\rm th}_{\rm ioniz}$, a defect is registered and can be observed by TEM.

In our case (200 MeV Au ion irradiation of InP) the thin foils thickness ($\leqslant 200$ nm) is much less than the 200 MeV Au ion range into InP (~ 20 μm). Therefore it can safely be assumed that the energy loss is almost entirely electronic deposition along the entire thickness of the thin foil. Furthermore, the energy loss along the entire foil thickness is well above the threshold energy for track formation in InP ($\sim$ 13 keV/nm) as calculated from SRIM 2003 ($\sim$ 21.3 keV/nm) thus excluding the first phenomenological model. Therefore no fluctuation of S_x can arise along the foil thickness. This also totally excludes the phenomenological fluctuation model. In fact the probability of a charge fluctuation process for this thickness is very low since it is directly proportional to depth. In addition there is an important point which is often overlooked, namely the complete *statistical* nature of Komarov's [30, 59, 67] charge fluctuation so that our TEM observations of regularly intermittent beaded track morphology cannot be simply explained by invoking this mechanism. Charge fluctuation operates potentially at depths of several microns deep inside irradiated InP when the value of S_x approaches the $S^{\mathrm{th}}_{\mathrm{ioniz}}$ giving rise to tracks consisting of separated strings of defects without any spatial regularity and with separation distances between these defect beads up to $\sim$ tens of nm as was clearly observed in the case of SHI irradiated Ge [56]. The remarkable regular track structures, we observe, therefore require a new and probably different *dual* explanation (either atomistic or continuum). We consider two possibilities as follows:

1.3.3. Sink-Modified Subsurface Tracks (Skin Effect). The influence of the surface on the formation and stability of defects is an important concern when irradiating crystals, especially thin foil samples, as the two surfaces are in proximity to each other ($\leqslant$ 200 nm for electron transparent samples). Therefore, surfaces are expected to act as strong sinks for defects [70–73]. An interesting demonstration is the TEM observation by Ohtsuka et al. [74] for SHI irradiated Au nanocrystals. Here the defect density was found to fall with decreasing nanocrystal size, that is, surface to volume ratio increased. During the ion-track formation phase in InP, when defects abound, it is clear, then, that strong surface effects as sinks for formed defects are to be anticipated. In the case of a thin foil sample the existence of two close surfaces must lead to depletion or «*draining*» effects on defects formed during the extreme short transient time of the *compound spike* [37], within the volume around the ion trajectory. In consequence *condensation* of the remaining defects into a beaded structure must be seriously considered.

1.3.4. Hydrodynamic Instability of Ion Tracks (Rayleigh Instability in Tracks). The intermittent nature of tracks in InP where tracks are pinched off along their axes giving rise to a beaded structure of nanospheres (see Fig. 9 for different ensembles of tracks in InP), also immediately points us to classical hydrodynamics and, in particular, to the criteria for Rayleigh [75] instability leading to linear fractionation. This break-up was first described by Rayleigh in 1887 for capillary-driven falling liquid columns and jets [75] (see Appendix for a general synopsis).

Basically, for systems with isotropic surface tension, the equilibrium shape in the absence of external fields is spherical (the sphere of all volumes has the minimum surface to volume ratio). A cylinder of isotropic material will eventually become a sphere (Fig. 10). This arises from a peculiar property of cylinders;

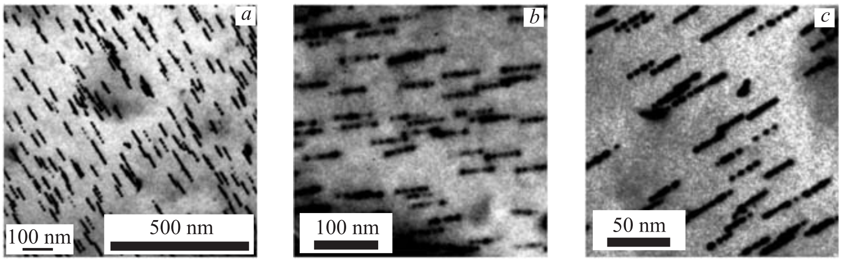

Fig. 9. A closer TEM observations of ion track morphologies distinguished by the intermittent beaded structures (nanoshperes of lattice disorder) deemed to be analogous to the classical Rayleigh instability leading to break-up into nanoshperes of lattice disorder

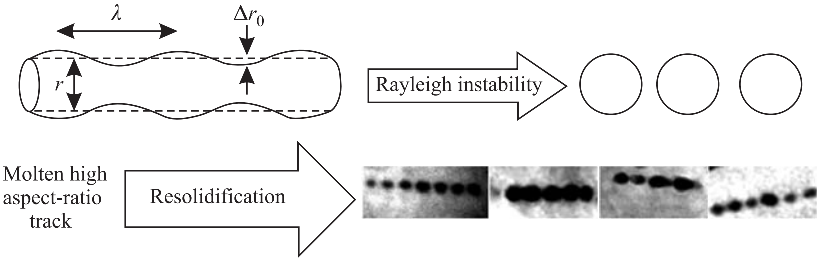

Fig. 10. A schematic representation of a molten cylinder of radius r with instability of magnitude Δr_0 and wavelength λ along its axis and the eventual break-up into a string of spheres after the onset of Rayleigh instability driven by capillary effects (whereby the volume is conserved and remains the same but the surface tension of the system is reduced). This instability amplifies and leads to constriction and fragmentation and eventual break-up into array of spheres. A track can follow the same scenario during the short transient time of its molten state. Morphologies of several single ion tracks suggest that instability

when slightly distorted in axisymmetric fashion at constant volume, they present a smaller surface area than the original area of the straight cylinder, at least for a range of longitudinal perturbations whose longitudinal wavelength is larger than the circumference of the cylinder. This drives the cylinder toward a configuration that minimizes its net energy, thus causes instability in the form of constriction, fragmentation and the eventual break-up to spheres. The time to attain this equilibrium may be extremely long unless physical dimensions, such as radius and length, are very small (similar to our tracks). The smaller the radius, the faster the Rayleigh instability will develop.

Generally, the final equilibrium shape of a cylinder stems from minimization of the surface energy at surfaces and interfaces, which can be expressed in the form of

$$\psi^{(s)} = \int \gamma \, dA, \tag{1.7}$$

where the elements *dA* of surface area and the integral runs over a closed surface where γ — the surface tension — must be a stationary at this surface area element. In the final equilibrium state $\psi^{(s)}$ will be minimized with respect to all changes in the form of the surface/interface at constant volume of the cylinder. Thus a cylinder of radius r may be unstable with respect to longitudinal variations in radius. The anticipated intermediate morphology, between a single cylinder and a single sphere, is a linear array of smaller spheres. The fluctuation in the shape of a cylinder which produces a small sinusoidal variation in radius Δr of amplitude Δr_0 and period λ, is indicated in Fig. 10. The cylinder then has a curvature variation K, which will vary along the length of the cylinder x, so that [132]:

$$K = \frac{1}{(r + \Delta r)} + \left(\frac{2\pi}{\lambda}\right)^2 \Delta r_0 \ \sin\left(\frac{2\pi x}{\lambda}\right). \tag{1.8}$$

There will be nodal points of minimum radius, where the chemical potential is higher than that at the antinodal points of maximum radius, assuming $(\Delta r_0/r)$ is significantly less than unity, so that the onset of the instability (Rayleigh criterion [75]) occurs (leading to the morphological transformation from a cylinder into a string of arrayed spheres with radii not much different than the radius of the precursor cylinder, the volume is conserved, hence only the surface is minimized) when

$$\lambda/r > 2\pi. \tag{1.9}$$

Thus, small variations of the cylinder's initial radius r with wavelength λ longer than the circumference of the cylinder will be unstable. Generally, the excess chemical potential $\Delta\mu$ at any given point on the surface of the cylinder relates to the curvature K, the surface tension γ, and atomic volume Ω by the expression

$$\Delta\mu = K\gamma\Omega. \tag{1.10}$$

Fluctuations with sufficiently large wavelength λ will be unstable, and material will tend to migrate from minima to maxima (i.e., constriction along the longitudinal axis).

The Rayleigh criterion [75] applies for all values of r, but, due to kinetic limitations, it is only for small radii that such fluctuations will ever be observable. Instabilities arising from thermal instability of nanostructures with large aspect ratios have been reported recently in several observations of the morphology of metallic nanowires and Si/SiO wires [76, 77]. Figure 11 illustrates the instability of a Cu nanowire upon heating where the resultant break-up into Cu droplets has undeniable morphological similarity to the case of ion tracks. These nanostructures exhibit variations along their length when relaxing towards thermal stability by constriction and sectioning into extended cylindrical segments. At finalizing stage these fragments pinch off and break up into a chain of nanospheres.

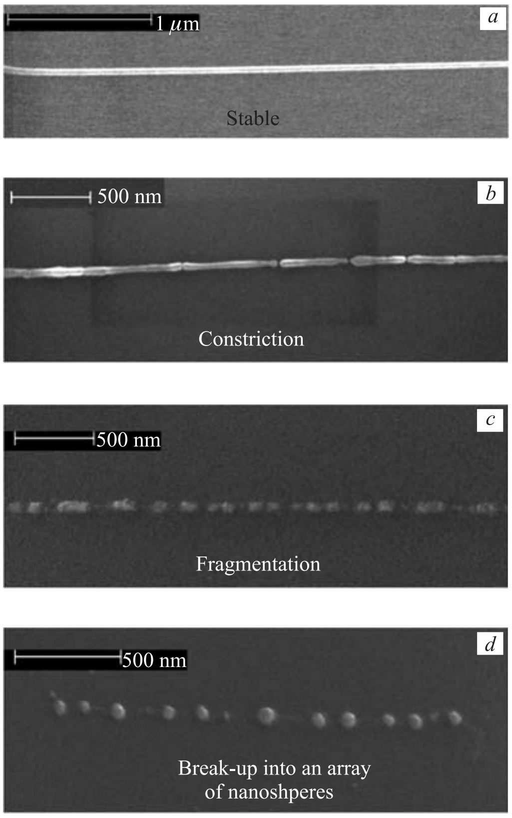

Fig. 11. A sequence of scanning electron microscopy (SEM) micrographs illustrating the fragmentation and eventual break-up of a Cu nanowire of 40 nm diameter on a SiO_2 substrate as a result of thermal annealing: *a*) room temperature; *b*) anneal at 400 °C for 30 min; *c*) anneal at 500 °C for 30 min and *d*) anneal at 600 °C for 30 min. No fragmentation occurred for wires larger than 60 nm in diameter at temperatures up to 500 °C [77]

It is relevant to note that recent calculations based on the Thermal Spike model for SHI irradiated (710 MeV Bi ions) InP showed that the calculated lifetimes of molten regions around the ion wake supports the existence of a transient liquid-like phase during track formation. The calculated temperatures exceed 1200 K in a cylindrical region of $\leqslant$ 12 nm in diameter [78], and the melting point of InP ($T_m = 1333$ K) can be exceeded. Rayleigh mechanism [75] is indeed plausible for ion tracks. Similar to the case of nanowires, ion tracks are characterized by large aspect ratio, i.e., a surface to volume ratio — which increases considerably with decreasing diameter of the cylinder. And given the fact that high temperatures may be present during their formation, there will be a need to minimize the energy of these high aspect ratio molten entities.

Mullins and Nichols [79] have given an extensive treatment of the kinetics of morphology changes in multiphase alloy systems in terms of Rayleigh instabilities [75] and ascribed the shape change to atomic surface diffusion. Similar factors can strongly affect the free energy of molten nanocylinder during the extreme short transitory period of track formation as it is driven towards relaxation and final thermodynamical equilibrium state within the surrounding lattice. Capillary forces and chemical potential minimization effects combined with defect diffusion on a local scale and very rapid quench, can render it unstable and drive the Rayleigh instability [75] along its length, giving rise to fragmentation, pinching, and the eventual break-up into the observed *registered* nanoshperes of disorder along the longitudinal axis of a precursor continuous track.

1.4. HRTEM of Ion Tracks Cores in InP. To elucidate the nature of the 200 MeV Au ion tracks in InP, they were investigated using HRTEM. For such imaging it is necessary to utilize very thin areas of the crystal which includes ion tracks and make the necessary perfect alignment of the crystal along a low-index zone axis (axis which coincides with a major crystallographic axis) to be parallel to the illuminating electron beam and allow for electron multibeam interference to form a lattice fringe image of the track core under very stable and rigorous illuminating electron beam and objective aperture conditions.

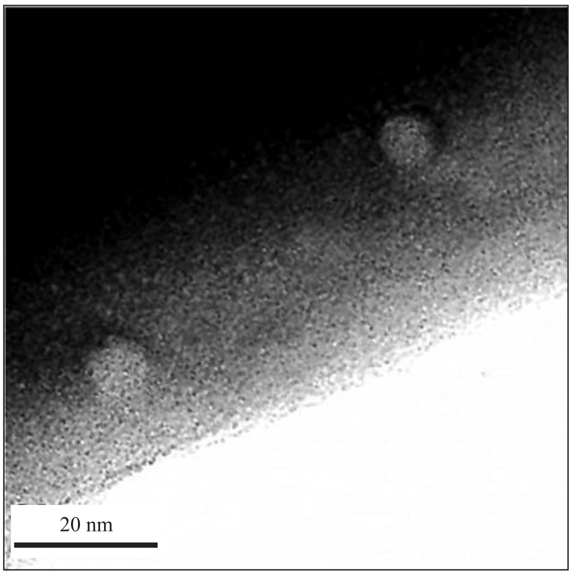

Fig. 12. High magnification BF TEM image of two tracks close to the edge of a thin foil of 200 MeV Au ion irradiated InP

Figure 12 is a high magnification BF TEM illustrating such a thin area containing two ion tracks with *apparent diameters* $= 8$ nm. This agrees well with the measurement estimated from BF TEM. On the other hand, in HRTEM lattice fringe images, the track cores of $\geqslant 5$ nm widths encompass $\sim 16{-}19$ lattice

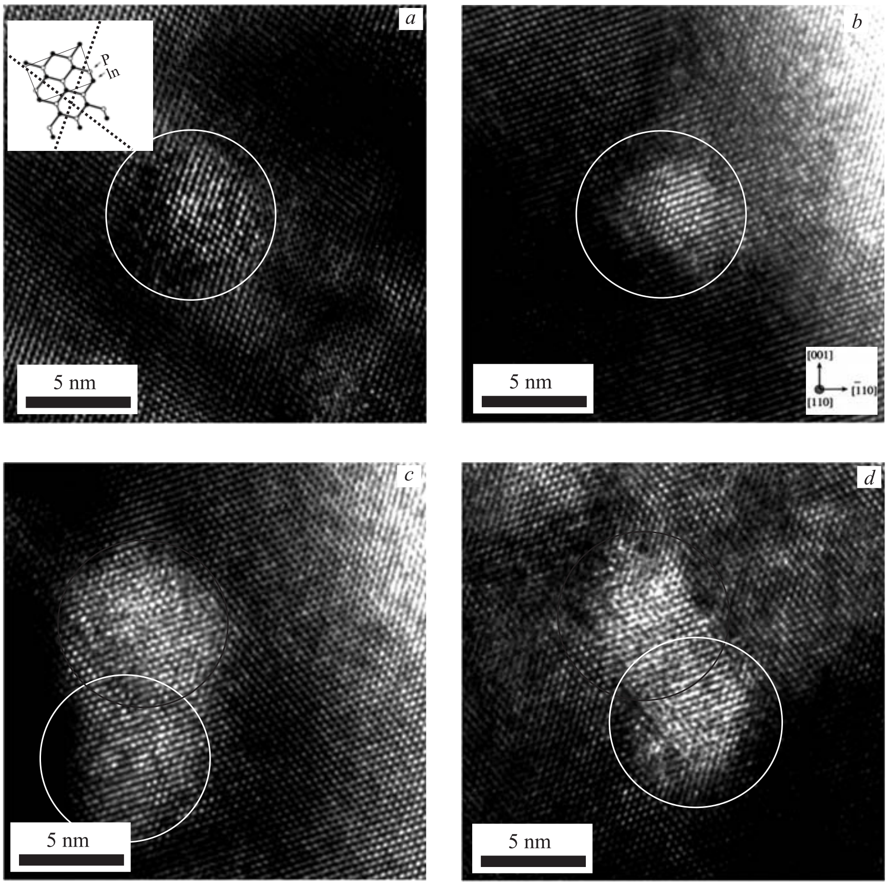

Fig. 13. HRTEM along [49] zone axis of ion track cores in InP. In all the micrographs fringes appear over the cores which suggest that the tracks are not amorphous in nature. In parts *a* and *b* are shown two HRTEM images of two different track cores. The inset in micrograph part *a* shows a unit cell and the corresponding atomic planes and open channels in the InP lattice as seen along the [49] orientation. And in *c* and *d* are two HRTEM images of two different adjoining track cores which render track overlap observations in conventional BF TEM images (as pointed by arrows in Fig. 4, *a*). Circles defining 8 nm diameters as track diameter estimated from BF TEM images (Fig. 4, *b* and Fig. 12). Note: part of the upper track in *d* might be amorphous

fringes and appear to retain crystallinity as evident from the imaged lattice fringes over the tracks (see Fig. 13).

The [49] lattice fringe images in Fig. 13 were formed by seven beams around the [49] zone axis, near the Scherzer defocus condition, i.e., the objective aperture admits two sets of $\langle 111 \rangle$, one set of $\langle 200 \rangle$, and the transmitted electron beam $\langle 000 \rangle$. Therefore the spot patterns in these images are the result of interference of the three sets of planes rendering the observed lattice fringes images. The observed contrast, however, changes across the imaged areas; the contrast depends on stringent microscope conditions such as beam coherence, divergence, alignment and defocus conditions as well as sample flatness and thickness uniformity.

Therefore these images may not be real structure HRTEM images (accurate mapping of the projected atomic potentials distribution of the [49] planes from the phase relationships of diffracted electron beams accommodated by the objective aperture where every projected atom column of the structure along the zone axis is seen as a separate spot without any lateral shifts between spots and relevant atom column). Only under aberration-free conditions, and in extremely thin areas where the kinematical phase relationship between the diffracted electron beams is maintained, do the atomic columns of In and P appear as dark spots and the open channels appear as white spots as shown schematically in the inset and we obtain a real structure HRTEM image.

Despite all these factors and irrespective of whether all proper conditions for structural imaging have been met, these lattice fringe images give us very useful qualitative information on the track cores. Generally, random noise-like contrast typical of amorphous materials does not appear inside the track cores and crystallinity «inside» the cores remains which might suggest recovery by homoepitaxial regrowth in the aftermath of the compound spike resulting in only disordered crystalline and defect rich InP but not a complete amorphous matter inside the core [94]. In this context, we have also carried *in-situ* electron beam burning of a nanohole (width ~ 5 nm) in unirradiated thin foil InP sample by converging and focusing the 200 keV electron beam (flux $\sim 1.4 \cdot 10^{19}$ $\mathrm{cm}^{-2} \cdot \mathrm{s}^{-1}$) for 5 seconds on a small spot near the edge of the sample. Evidence of the amorphous structure as a result of intense local heating near the edge of the hole is therefore expected. This was confirmed by the observation of the nonperiodic contrast associated with amorphous matter (which was not observed in the track cores) in the lattice fringe image in Fig. 14.

Despite, we did not observe any clear sign of amorphousness in our HRTEM investigation of the track cores (i.e., in evidence of aperiodic fringes which might indicate that there is amorphous matter) we also exercise an element of caution, since lattice fringes may also arise from crystalline material lying above, below, or between the nanospheres of disorder comprising the ion tracks in InP if they were indeed amorphous (see Fig. 15).

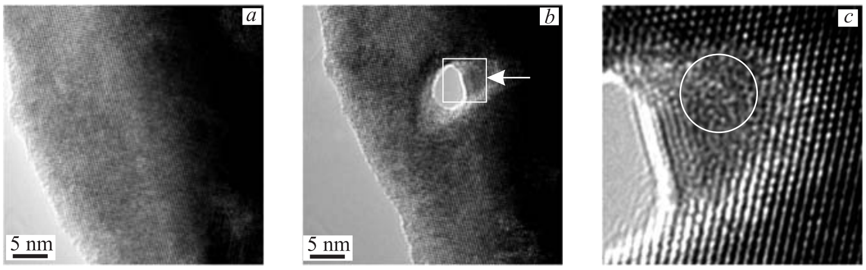

Fig. 14. Evidence of amorphous structure near an electron-beam-drilled hole in InP thin foil specimen: *a*) before electron beam-burning; *b*) after focusing the electron beam for 5 s; *c*) an enlarged image of the area pointed by arrow showing the typical HRTEM contrast synonym for amorphous material (circled)

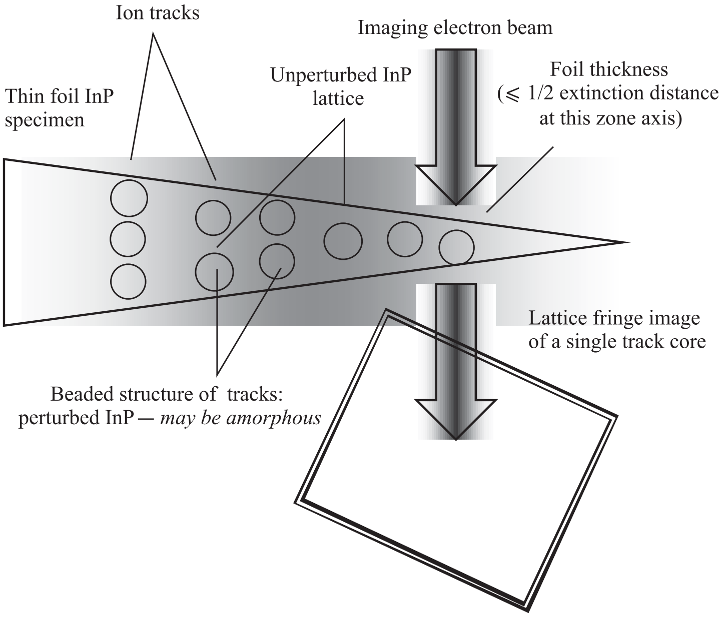

Fig. 15. Schematic representation of HRTEM imaging of a InP thin foil containing ion tracks which consist of strings of nanoshperes (if the nanoshperes are amorphous, lattice fringes in HRTEM images might still arise due to *undisturbed* lattice in-between)

Another interesting observation is that in the vicinity of several tracks, features of what appear to be dislocation or interstitial loops were observed (Fig. 16). These defects can be created during the track formation process due to large shear stress generation in the surrounding matrix. Indeed, stress can result from the

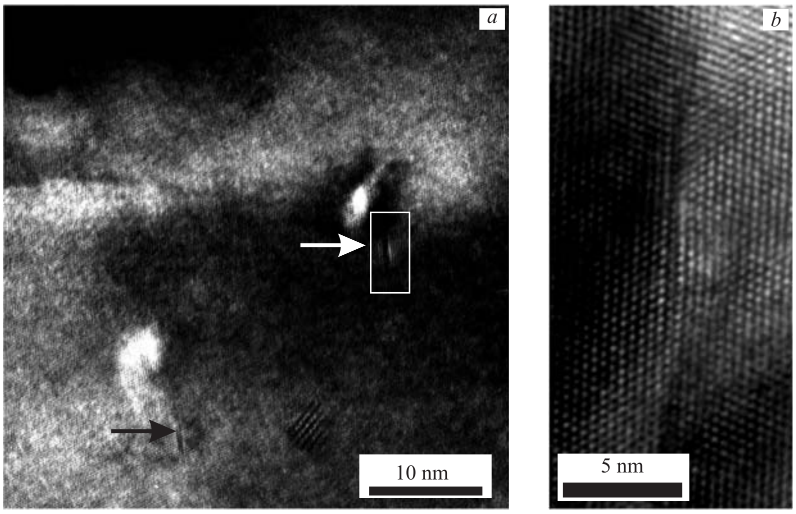

Fig. 16. *a*) High magnification TEM (× 400 K) of defects — possibly dislocation loops or stacking faults in close proximity (< 10 nm) to ion tracks. *b*) HRTEM lattice fringe image of such a defect (enclosed in a box in Fig. 16, *a*)

emission of pressure shock waves around the ion trajectory [80, 81] which propagate radial and affect the lattice order in the neighborhood of a track giving rise to formation of dislocation loops, microtwins and stacking faults in the vicinity of ion tracks [30]. Also, if we infer the existence of a transient liquid-like state for InP during the track formation [78], a volumetric density change must be expected, which may also give rise to a transient large pressure spike. Similar observations of such defects were reported by Gaiduk et al [60, 61] for 250 MeV Xe ion irradiated InP single crystals.

1.5. Inelastic Collision-Induced Amorphization in SHI Irradiated InP. The progression of inelastic-energy-loss-induced amorphization was investigated for InP by means of RBS/C and TEM. RBS/C spectra of 2 MeV He^+ ions backscattered from 200 MeV Au irradiated InP for different ion fluences are shown in Fig. 17. The observed yield over the energy range increases with increasing fluence, which is consistent with an increase in the amount of disorder. At fluences $\geqslant 1.0 \cdot 10^{13}$ cm^{-2}, the spectrum has reached the level of the random spectrum. This is consistent with the surface layer becoming completely amorphous.

The amount of relative disorder $(\Delta\chi)_{\rm min}$ calculated over an energy range of 1600–1800 keV in InP due to 200 MeV Au ion irradiation is plotted as a function of the fluence in Fig. 18.

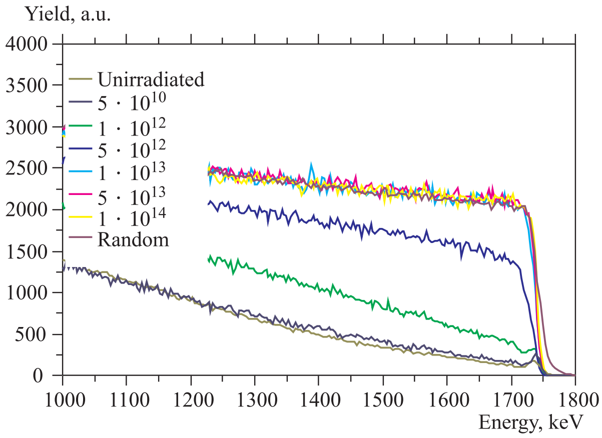

Fig. 17. RBS/C spectra of backscattered 2 MeV He ions from 200 MeV Au ion irradiated InP for different ion fluences

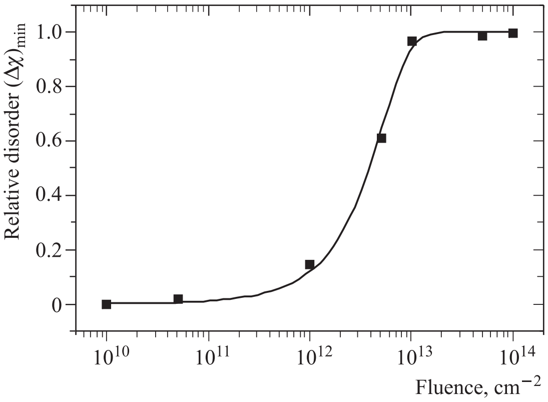

Fig. 18. A plot of relative disorder $\Delta\chi_{\min}$ versus ion fluence for 200 MeV Au ion irradiated InP. The best fit is obtained by using the modified Hecking model. The uncertainty for each ordinate data point is $\leqslant 5\%$

The modified Hecking model [12, 82, 83], which takes into account both direct impact amorphization and stimulated defect amorphization, was used to fit the data. The best fit parameters for the $\Delta\chi_{\min}$ versus ion fluence are $\sigma_a = (1.0917 \pm 0.22) \cdot 10^{-13}$ cm^{-2} and $\sigma_s = (2.9028 \pm 0.79) \cdot 10^{-13}$ cm^{-2}. This again stresses the role of both heterogeneous and homogeneous mechanisms for reaching complete amorphization in InP due to 200 MeV Au irradiation. However, σ_s is higher than σ_a which suggests some dominance of SHI simulated defect production rather than direct amorphization inside track cores (no amorphous tracks appeared by HRTEM).

Again it should be emphasized that the RBS/C technique cannot reveal the fundamental nature of damage *inside* track cores. TEM observations of thin foil InP irradiated at different fluences reveal that for a fluence of $5.0 \cdot 10^{10}$ cm^{-2} the tracks are well separated (see Fig. 19, a) and that for increasingly higher fluences overlapping tracks start to be more frequent. TEM observations for a $1.0 \cdot 10^{13}$ cm^{-2} irradiated sample (see Fig. 19, b) show that individual tracks can no longer be distinguished. The overlap of tracks results in modified material regions which are amorphous. This is supported by the faint diffused halo appearing in the corresponding SADP (inset).

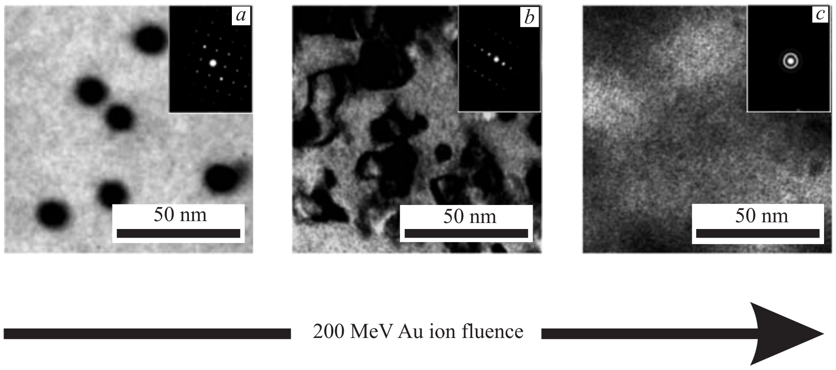

Fig. 19. TEM images showing amorphization in 200 MeV Au ion irradiated InP. The fluences are: $5.0 \cdot 10^{10}$ (a); $1.0 \cdot 10^{13}$ (b), and $5.0 \cdot 10^{13}$ cm^{-2} (c). Insets are the corresponding SADPs

However, there is a slight discrepancy between the amorphization fluence revealed by RBS/C and TEM observation (see Fig. 19, b) which shows that at $1.0 \cdot 10^{13}$ cm^{-2} the material still retained some crystallinity and is not fully amorphous whilst it certainly appears to be amorphous from RBS/C. This difference may be due to the influence of dechanneling in the RBS/C analysis and probably to the need for a slightly higher fluence to completely amorphize the thin foil relative to the bulk InP samples due to stronger surface(s) sink effects. Nevertheless, both techniques show complete amorphization for the fluence of $5.0 \cdot 10^{13}$ cm^{-2}. From TEM observations (see Fig. 19, c) for the $5.0 \cdot 10^{13}$ cm^{-2} irradiation, this sample becomes completely amorphous as indicated by both the strong diffuse rings in SADP, and in the absence of any diffraction spots synonymous with crystalline material.

Our observation is in agreement with previously reported observations for 250 MeV Xe irradiated InP for which complete amorphization occurs at fluences $> 1.0 \cdot 10^{13}$ cm^{-2} [111]. Likewise Komarov et al. [78] report on 710 MeV Bi ion irradiated InP, and find an amorphous layer by means of optical microscopy using selective chemical etching of high fluence irradiated samples.

It should be noted that the apparent *width* of the track cores from our HRTEM observation is $\sim$5 nm. Therefore, taking this as the *effective diameter* of the damaged area due to single 200 MeV Au ion, and basing on *very simple* argument that each irradiating ion creates this damage, one can conclude that this is valid since each 200 MeV Au ion creates a track in InP as mentioned earlier. Then the minimum fluence required to cover an area of 1 cm^2 with damage *without taking any overlap into account* is $1\ \text{cm}^2/\pi\,(2.5\ \text{nm})^2 \sim 5.0 \cdot 10^{12}\ \text{cm}^{-2}$. However, for a $1.0 \cdot 10^{13}\ \text{cm}^{-2}$ irradiated InP (i.e., at fluence which is twice that required for complete cover of the surface by these damaged areas as the simple calculation based on the above simple assumption) the sample is still not completely amorphous and SADP shows that some crystallinity still remains as evident from the Bragg spots (see inset of Fig. 19, *b*) This simple argument may also corroborate our HRTEM observations of track cores. In a very real sense this points to a more complex amorphization process for InP and that multiple 200 MeV Au ion impacts are indeed required to complete amorphization in this material.

1.6. Thermal and Electron Beam-Induced Annealing of Tracks in InP.

1.6.1. Thermal Annealing of Tracks. The thermal stability of tracks was investigated by heating the sample *in-situ* in the TEM. In this experiment, the electron beam was shifted from the area under investigation to minimize any effect of electron-beam-induced-annealing and returned back to the same area for TEM imaging upon reaching the required temperature.

A sequence of micrograph depicting thermal annealing of tracks is shown in Fig. 20. The associated strain fields due to lattice disorder inside the tracks appeared as dark contrast areas in the BF TEM images start to disappear upon heating, many tracks disappear upon reaching 440 K, and for 470 K almost all the tracks and associated dark contrast attributed to strain in lattice disappear, indicating almost full annealing of the damage. Figure 21 is a plot of the total area of dark contrast normalized to the area at RT (i.e., the area at which the disorder is maximum), as a function of reciprocal temperature.

We note here that an activation energy of 1.54 eV was reported for thermal annealing of residual *amorphous* damage in InP [84].

However, broad annealing stages ranging from 100–400 K have been reported in a variety of III–V compounds [85]. This may be due to recombination and reconfiguration of a variety of defects with different activation energies. The fact that a wide annealing stage exists for III–V compounds also suggests that a variety of trapping centers of both kinds of interstitials are involved. Despite that the nature of disorder/defects inside the tracks in InP is not known, thermal anneal of disorder is expected at these range of temperature. In the case of irradiated InP there may be generally two types of defects in the two types of sublattices (in addition to the antisite defects, e.g., In_P and P_In in InP) which

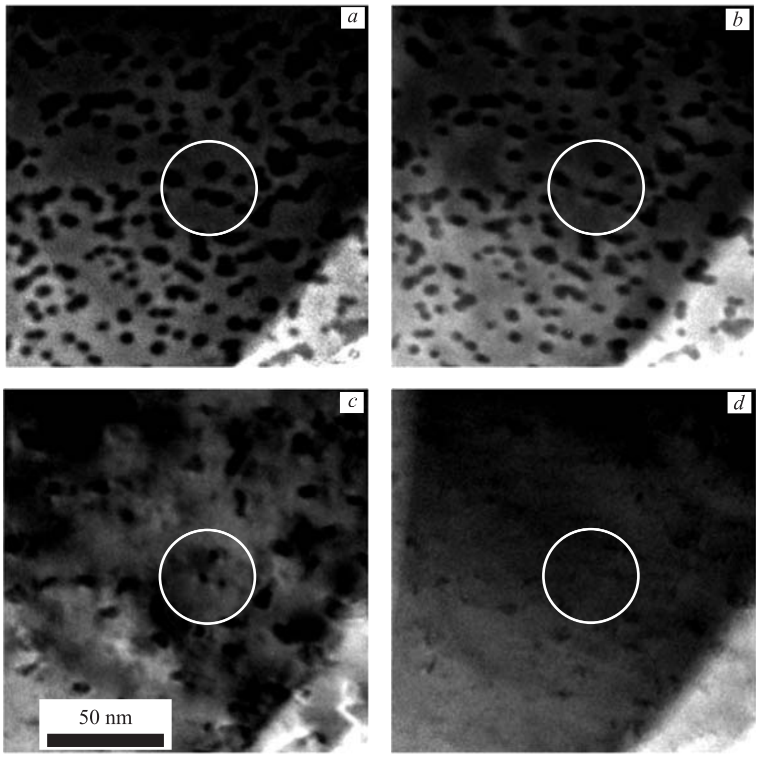

Fig. 20. Sequence of BF TEM images, illustrating the thermal stability of ion tracks in InP (*a*) RT annealed for 10 min at 330 K (*b*), 440 K (*c*), and 470 K (*d*)

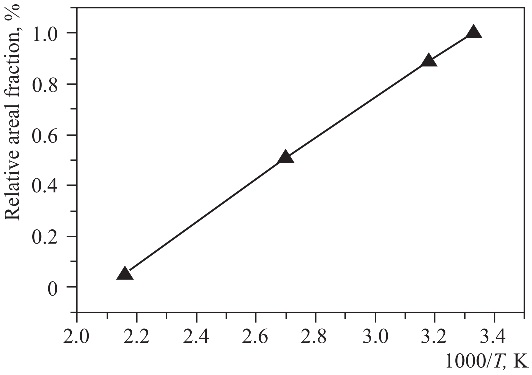

Fig. 21. Plot of the decrease of the relative areal fraction of tracks versus the inverse of temperature for 10 min annealing steps. The uncertainty for each ordinate data point is $\leqslant 10\%$

react independently. Those that anneal below room temperature are related to group III (i.e., In in InP) sublattice, whereas these defects related to group V (i.e., P in InP) are interstitials and become mobile at ~ 500 K as suggested by Turos et al. [140].

1.6.2. Electron-Beam Induced Annealing of Tracks. The electron beam-induced annealing of single tracks was carried out using HRTEM imaging at 200 keV energy and the sample temperature was maintained at liquid nitrogen temperature. The electron beam current was measured directly by a picoameter attached to the microscope (JEM-2010 F) and scaled to the irradiated area of the sample. The electron flux rate was $\sim 1.4 \cdot 10^{19}$ cm$^{-2} \cdot$ s^{-1}.

Figure 22 shows lattice fringes images of an area which contain three single tracks. The tracks were found to disappear with increasing 200 keV electron flu-

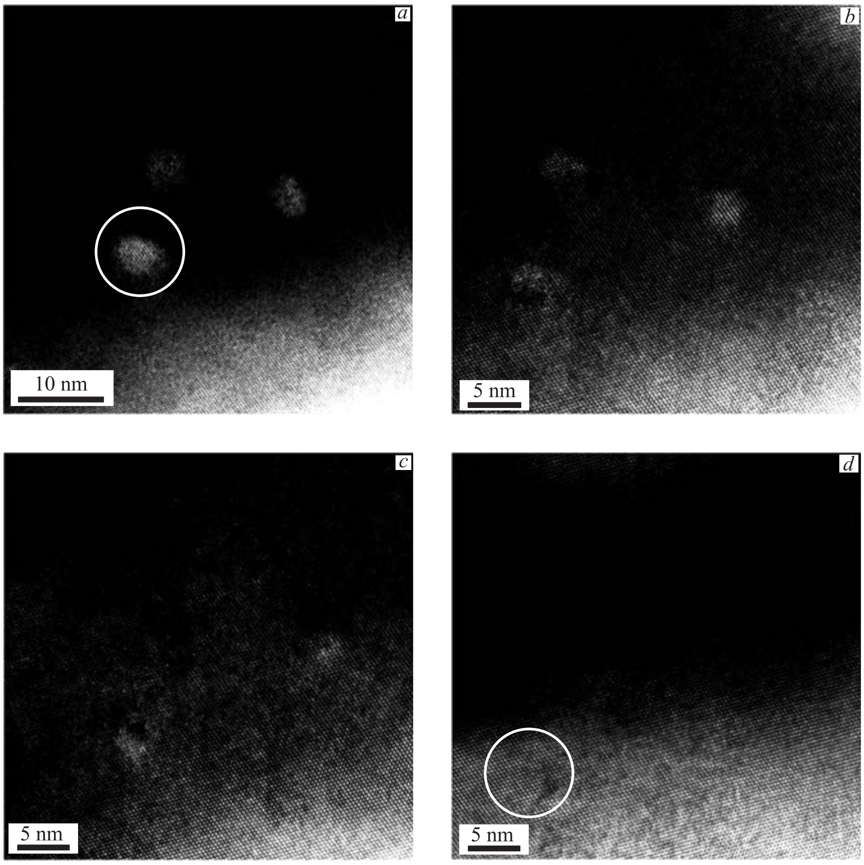

Fig. 22. Electron beam-induced annealing of ion tracks in InP before electron irradiation (*a*), $\sim 2.5 \cdot 10^{21}$ cm^{-2} (*b*), $\sim 9.3 \cdot 10^{21}$ cm^{-2} (*c*), and $\sim 2.4 \cdot 10^{22}$ cm^{-2} (*d*)

ence, and complete lattice recovery occurred as evidenced from our observations when the electron fluence reached $\sim 2.4 \cdot 10^{22}$ cm^{-2}.

This is clearly shown in the enlarged sequence of HRTEM image of the single ion track circumscribed by a circle in Fig. 22. When electron fluence reaches $\sim 2.4 \cdot 10^{22}$ cm^{-2}, the lattice is almost completely restored as revealed by the completely ordered lattice fringes in the final image relative to the previous images in the sequence.

This HRTEM observations may be the reason behind the track fading as shown in Fig. 23 in conventional BF TEM, where after reaching certain electron fluence (during prolonged observation, for example) the lattice disorder inside the track core is *repaired* by the imaging electron beam (electron beam-induced annealing). This in turn leads to the observed fading of the dark contrast in BF TEM image of the track synonym for disappearance of disorder inside the track core and consequently the associated strain giving rise to the dark contrast in BF TEM.

Whilst the atomistic nature of defects inside the track core is not yet known, the recovery of the track cores can be explained by electron beam-induced recovery and by anneal of disorder inside the core (see Eqs. (7) and (9) in [13]). The recovery processes may proceed by electron beam-induced bond breaking and rearrangement at the interface between the track core and the intact surrounding matrix.

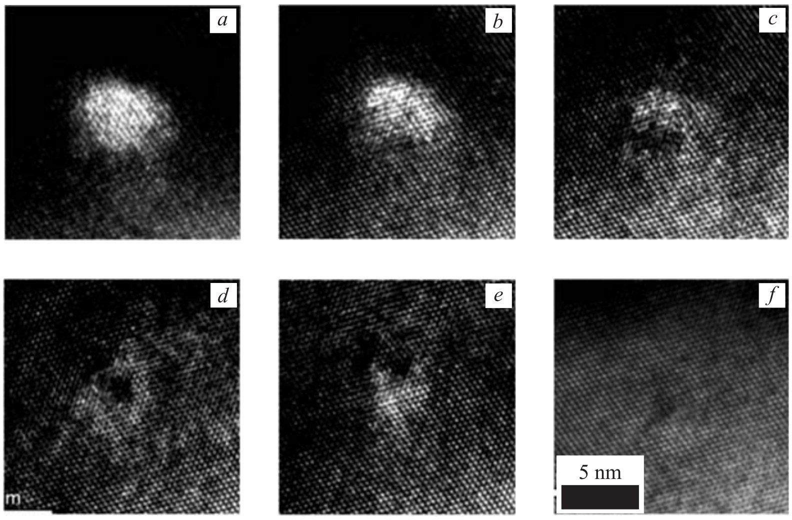

Fig. 23. HRTEM images time sequence of electron-beam-induced annealing of a single track core (circled in Fig. 22, *a*): *a*) before electron irradiation; *b*) $\sim 8.4 \cdot 10^{20}$ cm^{-2}; *c*) $\sim 2.5 \cdot 10^{21}$ cm^{-2}; *d*) $\sim 7.6 \cdot 10^{21}$ cm^{-2}; *e*) $\sim 1 \cdot 10^{22}$ cm^{-2}, and *f*) $\sim 2.5 \cdot 10^{22}$ cm^{-2}

1.7. Observations of Track Peculiarities: Do Close Tracks Interact? Our observations of «*bending*» of one track towards another which either might be due to elastic scattering process between the irradiating ion and a *struck* lattice atom. Or, on the other hand, might point to a rather fundamental intrinsic effect due to point defects mobility in the overlapping «*halos*» or the associated large stress field around each track. Figure 24 illustrates two such observed track events in InP.

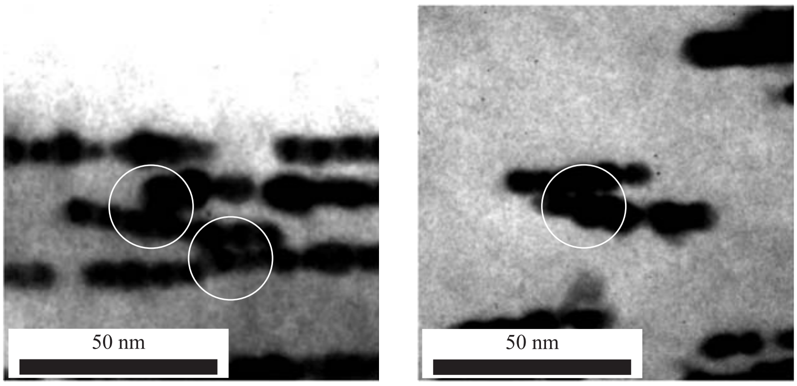

Fig. 24. TEM images showing track «*bending*» in InP

Point defects interaction between an early track and one formed later but close enough to it (as track registration by its nature is an extremely swift process (see Fig. 1) relative to ion irradiation duration therefore not all the observed tracks form simultaneously at one point in time), seems to be rather clear.

It is a known fact that damaged or disordered regions in a crystal including extended defects (e.g., dislocations, stacking faults, vacancy clusters, precipitates, grain boundaries, etc.) can act as effective sinks. For example, tracks elastic field strength diminishes as $(1/r)$ (see Eq. (1.1) in Subsec. 1.2). The extent of disruption associated with the track may be much greater to that of dislocation. Whereby a simple edge dislocation, for example, introduces half a plan of atoms into a lattice and thereby distorts the surrounding lattice, tracks are a heavy trail of damage which expects to leave a strong disruption around its close vicinity.

Thus we anticipate that tracks, considered as simple cylindrical agglomerates of disorder in otherwise perfect crystal, will act as mutual sinks for each other and thus, as a consequence, track «*bending*» is a real microscopic consequence of this, concomitant with an ongoing minimization of the total aggregate energy.

1.8. Summary. Our observations of 200 MeV Au ion tracks in InP indicate that each ion creates a track, track morphology revealed by tilting the sample in TEM shows beaded structure of tracks; this might be due to Rayleigh instability or to the effect of surfaces as sinks for defects ultimately responsible for track formation. The track cores are not amorphous as HRTEM observation shows, and complete amorphization must be due to track overlap similar to the case of disordered zones. This is best described by invoking the modified Hecking model. Tracks anneal thermally and completely disappear when temperature reaches ~ 470 K. In addition tracks anneal under electron beam as evidenced by HRTEM observation. Evidence of possible intertrack interaction was presented.

2. SURFACE MODIFICATIONS DUE TO HIGH INELASTIC ENERGY LOSS IN InP

2.1. SHI Induced Modifications of Semiconductor Surfaces. Spectacular topography and surface changes occur when irradiating semiconductors with SHI [86–88]. In the 1980s it was discovered that amorphous materials bombarded with SHI depositing large electronic energies into the material exhibited dramatic surface and shape changes or macroscopic plastic deformations [89, 90]. This effect was termed ion-induced plastic flow and was found to occur in amorphous or amorphizable solids (after reaching the fluence sufficient to cause amorphization) but was not observed in materials which remain crystalline during SHI irradiation. In Figure 25 there is an observation by AFM of a topographical change as observed in 200 MeV Ag irradiated Si (111) surface as a function of ion fluence [91] where at $5.0 \cdot 10^{13}$ cm^{-2} the surface becomes completely amorphous as separately revealed by X-Ray Diffraction (XRD). The observations showed a large increase in the surface roughness for the SHI irradiated surface (despite no SHI tracks were observed yet in this material) when it became amorphous as is evident from hillock-like features observed for the higher fluences of irradiation shown in Fig. 25.

As reported for several irradiated semiconductors, such as Si subjected to MeV ion irradiation, stresses of the order of $\sim 10^8$ N/m^2 can occur transiently in the ion wake, leading to density changes and plastic phenomena [92, 93]. Once an amorphous layer is formed, radiation-induced plastic flow of material out of the plane of the irradiated surface occurs, and this relieves the stress created by the changes in density and the elasticity of the amorphous material. Moreover, if the irradiated semiconductor is in the form of a thin wafer, the stress generated will be manifested as a curvature of the wafer's surface after complete amorphization [92, 94].

The elastic constants (such as shear moduli, etc.) change only when the sample becomes amorphous in the case of many semiconductors. For example, the shear modulus of irradiated Si only showed a drastic change when it became completely amorphous and very little softening was observed even for heavily damaged Si [95]. Also it is interesting to note that covalent materials which exhibit irreversible density changes due to amorphization such as Si [96] prominently exhibit plastic deformation under SHI irradiation.

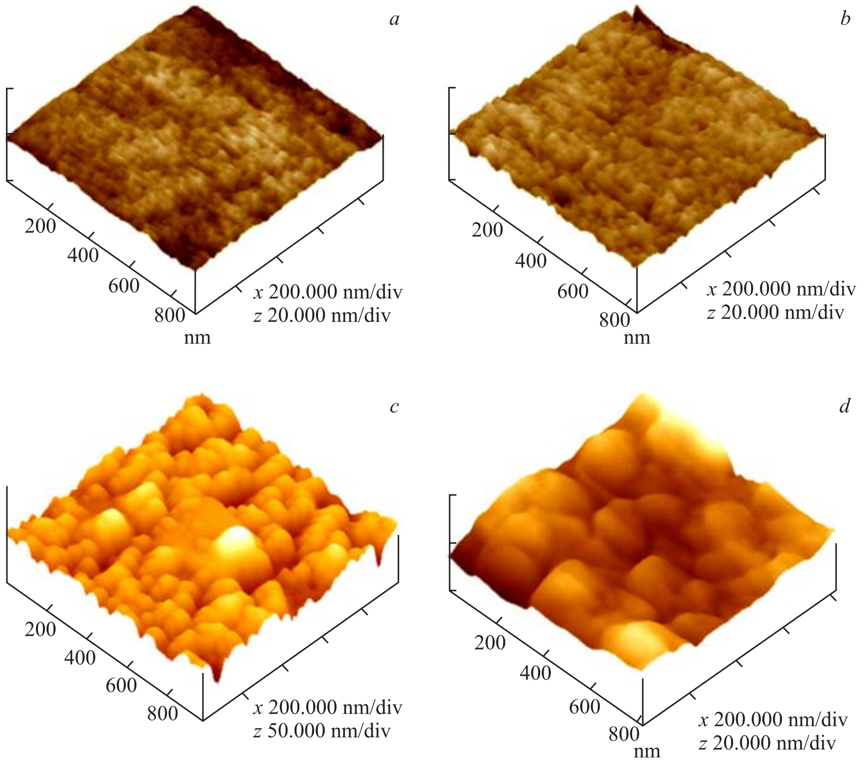

Fig. 25. AFM of 1×1 μm areas of a Si (111) surface unirradiated (*a*), and after irradiation with 200 MeV Ag^+ ions at fluence of $1.0 \cdot 10^{13}$ (*b*), $5.0 \cdot 10^{13}$ (*c*), and $1.0 \cdot 10^{14}$ cm^{-2} (*d*). Note that the vertical scale for *a*, *b* and *d* is 20 nm/division and for *c* is 50 nm/division [91]

Similar density changes occur in the case of InP, as this material compacts when amorphous. In a relaxed state, amorphous InP is $\sim 0.17\%$ more dense than crystalline InP and it increases by $\sim 7\%$ when in a molten state [97, 98]. This may be the case inside the track core during the very short transient time ($\sim$ ps) of track registration which leads to large transient stresses during the lifetime of the core whilst still in a liquid-like state. Once more it should be stressed that SHI induced mass transport and flow arising from plastic behavior in semiconductors is a phenomenon observed only when the materials become amorphous. Also, for irradiated amorphous materials, the transient tracks cannot recrystallize by homoepitaxial recrystallization and this itself may lead to transient stress build-up giving rise to prominent macroscopic plastic changes observed after reaching complete amorphization [26].

In addition, formation of an amorphous state becomes a crucial parameter in elastic and mass transport phenomena since an amorphous state has different elastic and transport constants compared to a crystalline or even heavily damaged surface. As recently shown by Hedler et al. [99] Si under 350 MeV Au ion irradiation flows plastically when the ion fluences reach $\sim 1.7 \cdot 10^{15}$ cm^{-2}. In another interesting observation, 30 MeV Cu ions induced anisotropic deformation in amorphous Si micron-sized structures whilst the crystalline counterparts showed no change [100]. And, observations of Si wafers irradiated with 100 MeV Au ions showed that a large increase of roughness occurs on the irradiated surface for higher ion fluences sufficient to cause amorphization [86]. A similar behavior was observed for InP irradiated with 24 MeV Se ions where deformation under the energetic ions only begins when InP becomes amorphous and where oblique conditions of irradiation can create structures such as «*ditch*» and «*dike*» after amorphization, due to macroscopic surface collective displacements. These observations were attributed to the electronic excitation SHII induced shear flow of the surface [98].

Trinkaus and Ryazanov [26] have discussed plastic deformation of amorphous solids under SHI bombardment, attributing this phenomenon to the thermal spike induced by intense electronic excitation and the consequent relaxation of the thermoelastic shear stress in hot cylindrical regions of the track. These authors presented a model based on viscoelastic considerations for plastic flow for amorphous solids under SHI bombardment. This model, known as the effective flow temperature approach, describes the viscous relaxation of shear stresses brought about by the rapid thermal expansion of the highly anisotropic heated region around the ion track. Relaxation occurs on a picoseconds time scale. Complete shear relaxation in this region is assumed to take place when the ion track temperature exceeds a certain flow temperature T^*, which should be close to the liquidus temperature for the amorphous phase. The response of the material will be fully elastic as long as the temperature inside the track is below T^*. When T exceeds T^*, the system becomes fluidic and mechanically unstable. Trinkaus and Ryazanov invoked the theory of elasticity and treated transient tracks in amorphous materials as ellipsoidal elastic inclusions in elastically isotropic media to calculate the viscous shear strains. They assumed that the corresponding strain increment will be quenched-in upon rapid cooling of transient track so as to produce the overall anisotropic deformation.

2.2. SHI Induced Modification of the InP (001) Surface. One can quite generally utilize AFM observations for illustrating the effects of the large electronic energy loss on the surface of the irradiated InP. Therefore, the evolution of the InP (001) surface as a function of the 200 MeV Au ion fluence was followed by AFM. The chosen variable was the root-mean-square roughness (RMS) which is the standard deviation of height values Z within the probed scanned area. This quantity is defined as

$$\mathrm{RMS} = \sqrt{\sum_{i=1}^{N} \frac{(Z_i - Z_{\mathrm{ave}})^2}{N}}, \tag{2.1}$$

where Z_{ave} is the average height within the scanned area; Z_i is the measured height at a given point i; and N is the number of points within the scanned area.

Different areas of 1×1 μm and less were scanned in the irradiated and unirradiated regions of the sample under ambient conditions in contact mode. The scanned AFM images had 512×512 point resolution. The RMS values were obtained after first-order image «flattening» for each acquired AFM image. The flattening routine basically removes noise in the form of observed *bow* introduced into the AFM image due to the tip-scanner configuration by calculating least-squares fitted second-order polynomial for each scan line, then subtracting it from the scan line, thus leveling the background of the image without any loss of information. The RMS determination was performed using the attached commercial Nanoscope III (R) software.

Figure 26 illustrates two-dimensional AFM images of scanned 500×500 nm areas for unirradiated and SHI irradiated InP for different ion fluecnes. The AFM image for unirradiated InP, showed a relatively smooth (001) surface profile on that scale (2 nm/division) as indicated by the sectional analysis across the surface. For the lowest ion fluence ($5.0 \cdot 10^{10}$ cm^{-2}) the surface profile is also relatively smooth with very small observed change as evidenced in the accompanied sectional analysis. Also, no large change in roughness occurs when the ion fluence reaches $5.0 \cdot 10^{12}$ cm^{-2} except the observed finer crinkling across the surface profile as evident in the sectional analysis in Fig. 26, *c*. This implies that the roughening on that scale is due to the increased ion impacts on the surface as expected. And, for the $1.0 \cdot 10^{13}$ cm^{-2} irradiated surface almost no change is evident (Fig. 26, *d*). Conversely, for the highest fluence irradiated InP surface ($1.0 \cdot 10^{14}$ cm^{-2}) which is now completely amorphous (as shown by RBS/C and TEM), the surface becomes very rough compared to the unirradiated and low fluence irradiated surfaces. The AFM observations reveal hillock-like features or protrusions (as the one pointed by the white arrow) accompanied by troughs-like features (pointed by black arrows).

This nanoscale topographical change for the amorphous surface is illustrated more clearly in Fig. 27, where three-dimensional projections of AFM images of both unirradiated and the highest ion fluence irradiated InP are shown together. The observed nanotopography change is clear and might imply nanoscopic material transfers evident from the rugged surface comprising protruded hillocks accompanied by troughs.

In Fig. 28, we show three-dimensional projections AFM images of two areas of the same irradiated InP sample ($1.0 \cdot 10^{14}$ cm^{-2}), the unirradiated area of the

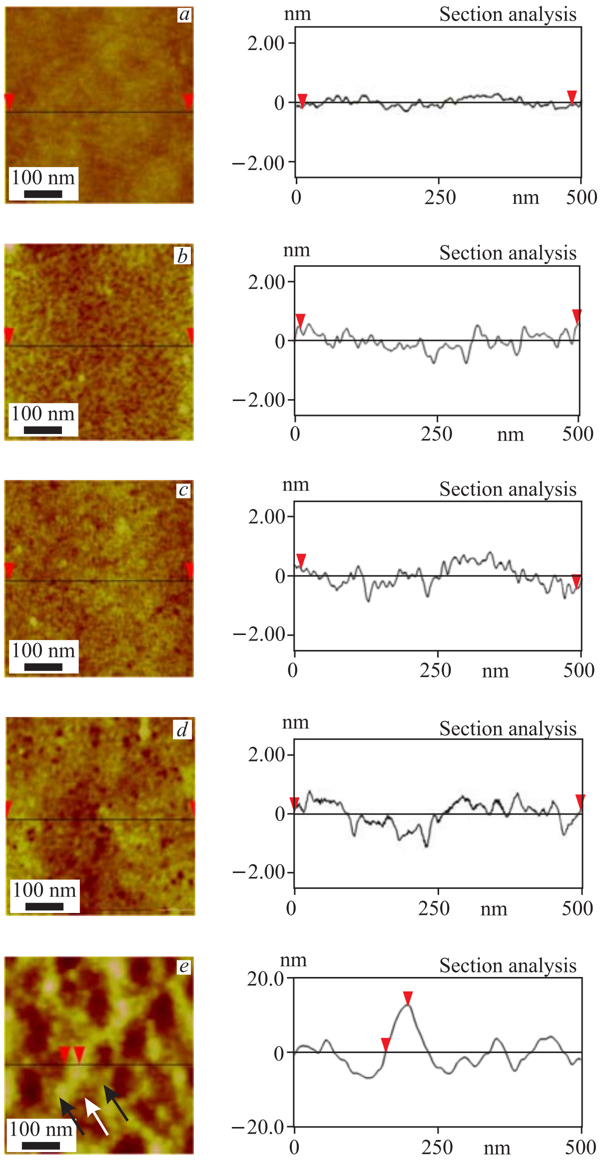

Fig. 26. AFM images of 500×500 nm scanned areas and sectional analyses across the surface of unirradiated InP (*a*), for $5.0 \cdot 10^{10}$ cm^{-2} (*b*), $5.0 \cdot 10^{12}$ cm^{-2} (*c*), $1.0 \cdot 10^{13}$ cm^{-2} (*d*), and $1.0 \cdot 10^{14}$ cm^{-2} (*e*) irradiated InP. The surface roughness increases for the highest fluence. Note that the vertical scale for *a* to *d* is 2 nm, while it is 20 nm for *e*

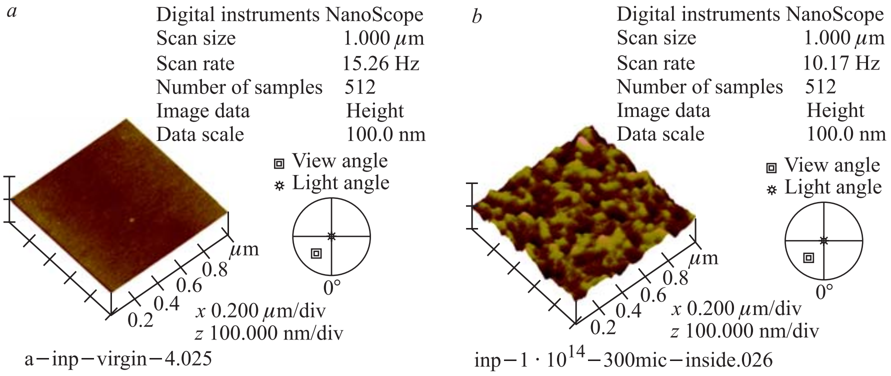

Fig. 27. AFM images of 1×1 μm scanned areas unirradiated InP (*a*) and $1.0 \cdot 10^{14}$ cm^{-2} irradiated InP (*b*) surfaces. Vertical scale = 100 nm/div

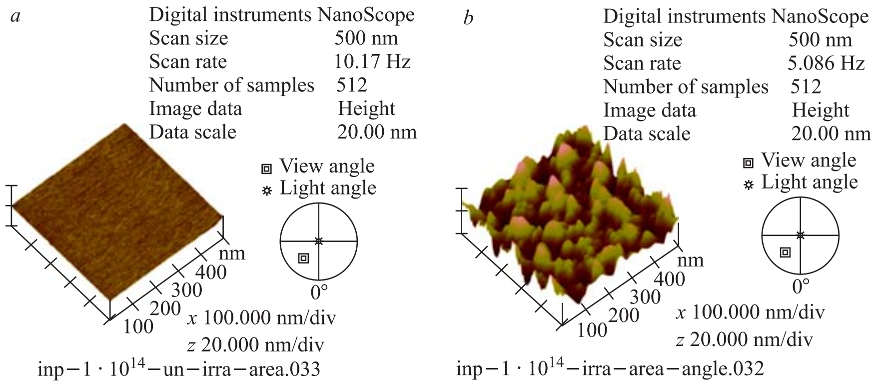

Fig. 28. AFM images of 500×500 nm scanned areas of: *a*) an area unexposed to the ion beam for the $1.0 \cdot 10^{14}$ cm^{-2} irradiated InP sample (i.e., still crystalline) and *b*) irradiated area of the same sample (amorphous). Vertical scale = 20 nm/div

sample (i.e., an area unexposed to the beam, and therefore remains crystalline) which is still smooth whereas the irradiated area of the same sample is rough. The now amorphous surface comprises many protruding hillock features.

On the other hand, for the low fluence ion irradiated surfaces, we have not observed well defined surface ion tracks (a surface ion track is the *imprint* of a single SHI impact onto the surface which can be observed, for example, as a hillock, crater or *cannot be observed at all*) instead we have observed pit-like features for the lower fluences irradiated InP surfaces. These pits thought to be surface ion tracks in InP as a result of 200 MeV Au ion impacts. This is shown in the AFM scans performed on smaller scanned areas as shown in Fig. 29, where

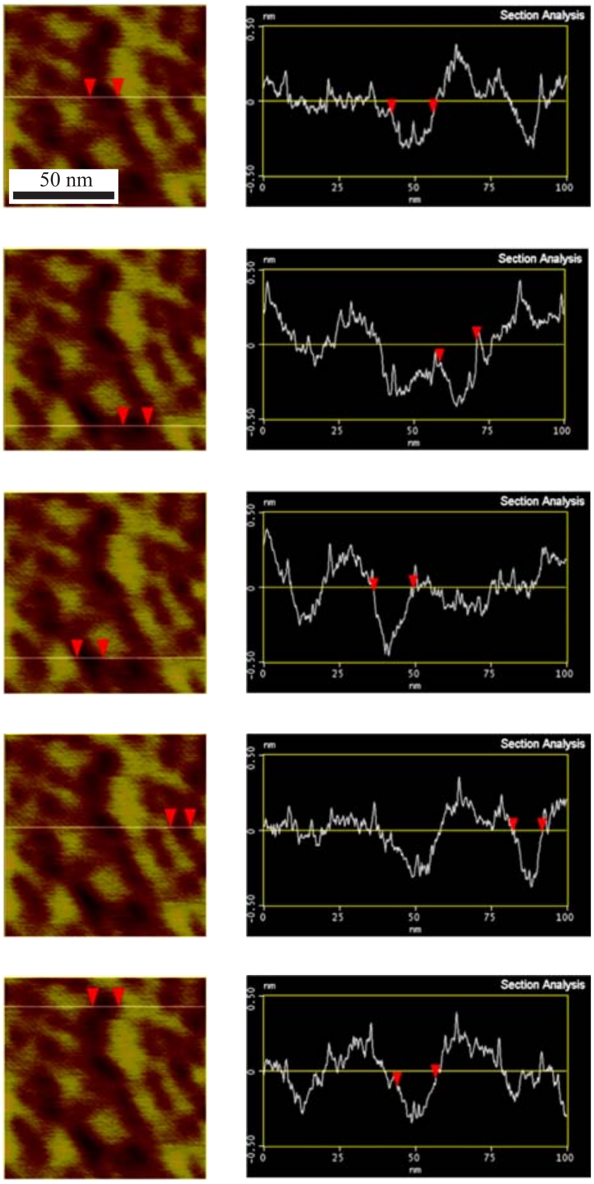

Fig. 29. AFM image of 100×100 nm scanned area of InP irradiated with fluence of $5.0 \cdot 10^{10}$ cm^{-2} and corresponding sectional analysis across the pit features which might be identified with surface ion tracks due to single 200 MeV Au ion impacts on the surface

the sectional analyses across such pits show that the average pit width to be equal to (12.3 ± 2.3) nm. These widths are in good agreement with our observation of the ion tracks in InP as revealed by TEM (track diameters of ~ 8 nm as shown in Fig. 5 and Fig. 12). In this scanned area of 100×100 nm we expect to find on the average ~ 5 pits (since at this ion fluence of $5.0 \cdot 10^{10}$ cm^{-2} we expect on the average ~ 5 tracks per each 100×100 nm area as shown in Fig. 7, *c*). The difficultly of observing the anticipated *well defined* surface ion tracks (identified with these nanoscale pits) in InP may be due to AFM tip convolution. This combination of tip-surface effects attributed to the geometry, shape and fineness of the tip apex relative to the imaged features can affect the final resolution (both lateral and depth) and the final observed appearance in AFM imaging of small nanoscale features like surface ion tracks in InP. The widths of surface ion tracks in InP might not be different than the tracks inside the material, in this case they are comparable in size to the AFM scanning tips (the Si tip apex radius of curvature ~ 10 nm). In addition to that, another factor can simply explain the

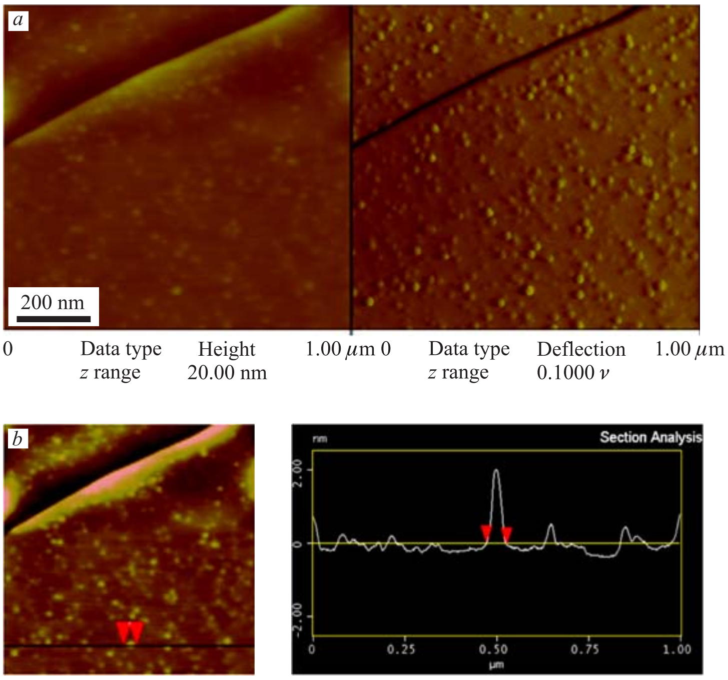

Fig. 30. AFM image of 1×1 μm area for 200 MeV Au ion irradiated muscovite mica (fluence of $5.0 \cdot 10^{10}$ cm^{-2}). The surface ion tracks are prominent and in the form of hillocks of widths of ~ 60 nm and ~ 2 nm in height. *a*) AFM images for both height (left) and deflection (right) modes and *b*) AFM sectional analysis through a surface track

lack of observing well-defined and prominent surface ion tracks in InP, mainly that, there is no strong 200 MeV Au ion-surface effects when an ion impacts the crystalline InP surface (e.g., Coulomb explosion or large sputtering yields which can result, for example, in an observation of hillock or crater, respectively).

For example, and contrary to the observed pits thought to be surface ion tracks in irradiated InP, large and well-defined prominent surface ion tracks were observed for both mica (hillocks) and MoS_2 (craters) as shown respectively in Fig. 30 and Fig. 31, the difference in sizes and forms of surface ion tracks again suggests the different behavior of surfaces of different materials upon SHI ion impacts.

Previous AFM observations on 100 MeV Au ion irradiated (111) InP surface to a fluence of $1.0 \cdot 10^{12}$ cm^{-2} due to Singh et al. [101], revealed similar features to our observed pit-type features but with larger *diameter* of ∼ 24 nm than our observations with an areal density corresponding to the ion fluence. They were

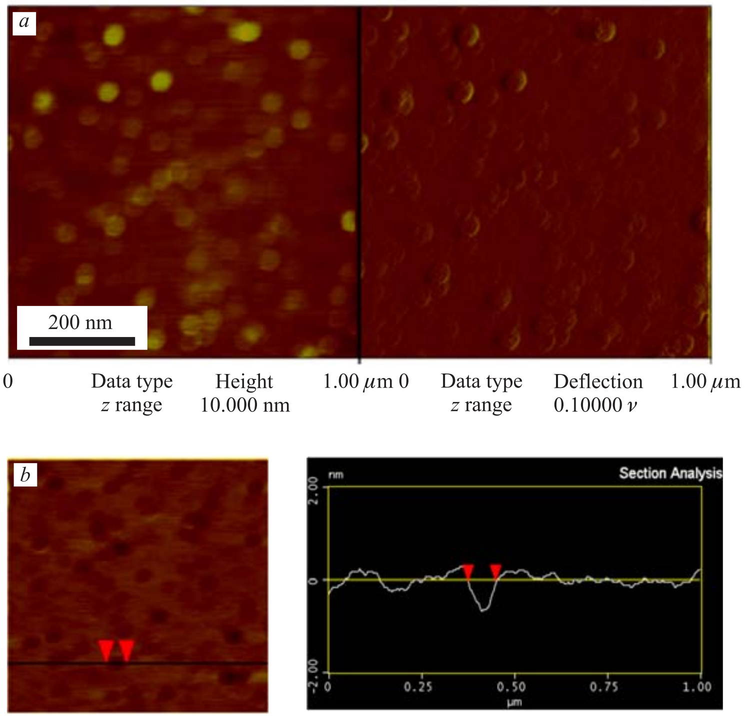

Fig. 31. AFM image of 1 × 1 μm area for 200 MeV Au ion irradiated MoS_2 (fluence of $5.0 \cdot 10^{10}$ cm^{-2}). The surface ion tracks are well defined craters with diameters of ∼ 70 nm and depths of less than ∼ 1 nm. *a*) AFM images for both height (left) and deflection (right) modes and *b*) AFM sectional analysis through a surface ion track

identified as surface ion tracks while no such features were observed for 180 MeV Ag^{+} irradiation of (111) InP.

As mentioned above, the important observation revealed by AFM is the development of large increase in surface roughness when the irradiated surface becomes completely amorphous.

Figure 32 shows a typical sequence of projected AFM scans for InP (001) irradiated surfaces at different ion fluences which clearly demonstrate the observed surface evolution with increased ion fluences. The large change only occurs for higher fluences $\geqslant 5.0 \cdot 10^{13}$ cm^{-2}, where a drastic increase takes place revealed as the multiple protrusions of hillock on nanoscale. A plot of RMS roughness as a function of fluence is shown in Fig. 33.

The RMS roughness increases dramatically for higher fluences at $5.0 \cdot 10^{13}$ cm^{-2} with a slight decrease for the $1.0 \cdot 10^{14}$ cm^{-2} ion fluence.

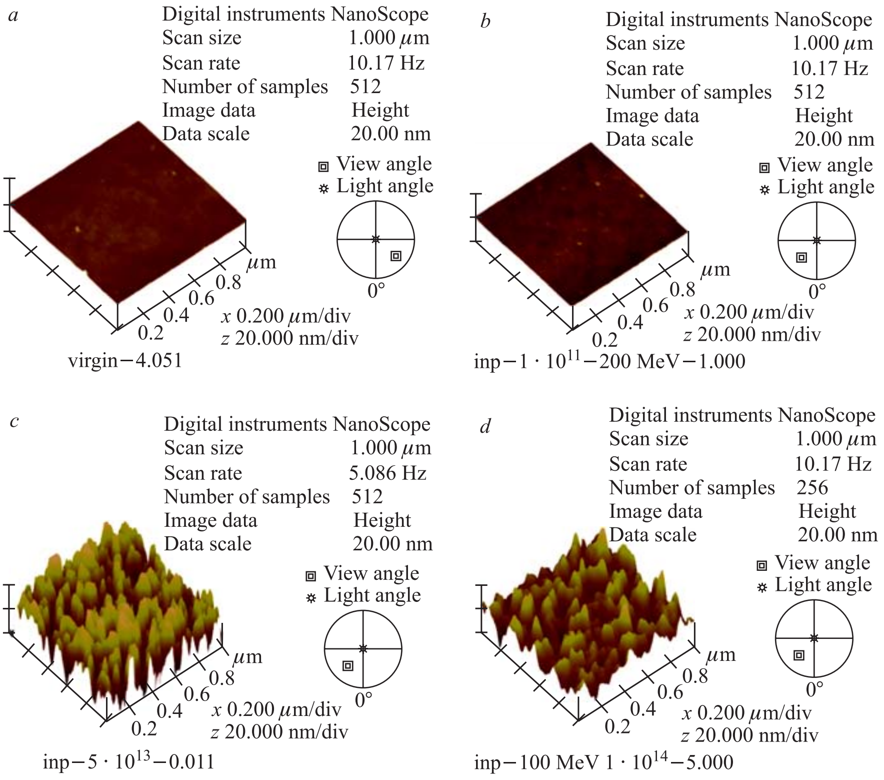

Fig. 32. Three-dimensional projected AFM of 1×1 μm scanned areas of unirradiated surface (*a*), $1.0 \cdot 10^{11}$ (*b*), $5.0 \cdot 10^{13}$ (*c*), and $1.0 \cdot 10^{14}$ cm^{-2} (*d*) irradiated (001) InP surfaces

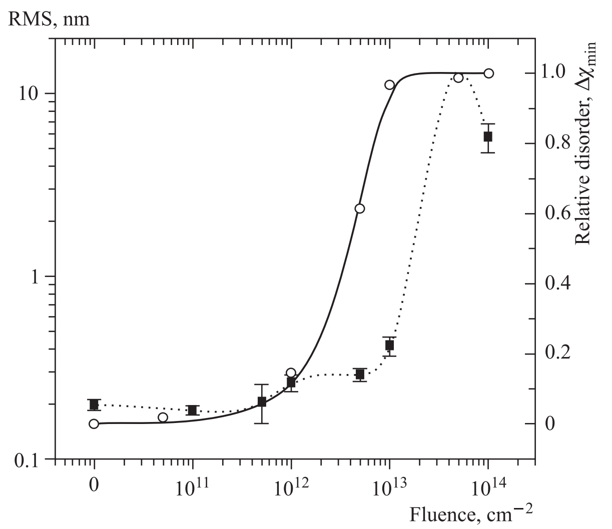

Fig. 33. RMS roughness (nm) as a function of 200 MeV Au ion fluence in InP (dotted line), also plotted is the relative disorder induced by irradiation (solid line)

This decrease may be attributed to slight smoothing of the hillock because of local variation in the angle of ion incidence due to the already developed nanoroughness. This is similar to the observation in SHI irradiated Si (in Fig. 25) where the height of the hillock-like features decreases for the highest fluence at $1.0 \cdot 10^{14}$ cm^{-2} [91]. Similar observations where reported for surface topography of GaAs (110) after high fluence low energy Si ion irradiation where the height of the observed hillock-like protrusions increases up to a certain fluence saturation level [102]. Also plotted in the same plot for RMS is the amount of relative disorder estimated from the RBS/C data illustrating the progression towards amorphization (from Fig. 18). In Fig. 34 we show our TEM observation for the $5.0 \cdot 10^{13}$ cm^{-2} irradiated InP (which is completely amorphous) compared to an unirradiated sample to confirm the observation of the developed nanoscale rugged topography of the surface as it became completely amorphous (as revealed by electron diffraction in TEM for that ion fluence). It should be noted that the contrast is reversed in case of the BF TEM micrograph relative to that for AFM image as the darker regions are thicker (the protrusion of the hillock-like features) than the lighter regions due to electron absorption contrast in TEM imaging.

The surfaces for lower fluence irradiations are smooth on that scale (the height scale for all scans is 20 nm/division). The significant increase in surface roughness only occurs for higher fluences when the surface becomes completely

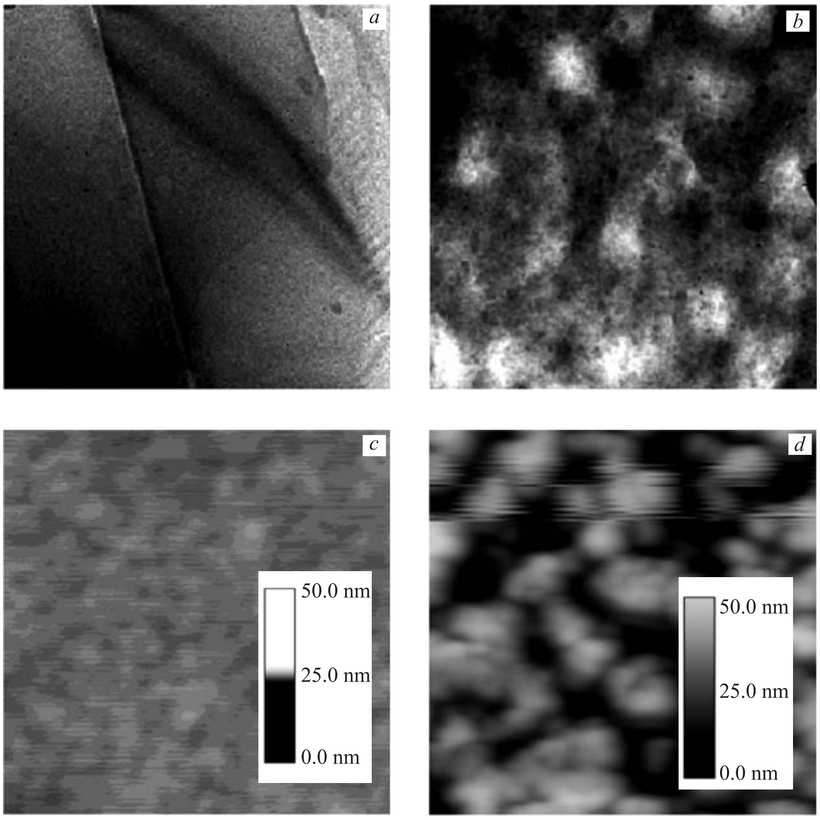

Fig. 34. BF TEM micrograph of unirradiated (*a*), $5.0 \cdot 10^{13}$ cm^{-2} irradiated (*b*) InP. The depicted areas are 500×500 nm, revealing the rugged topography of the irradiated sample relative to the unirradiated sample. Similar areas scanned by AFM of unirradiated (*c*) and of $5.0 \cdot 10^{13}$ cm^{-2} irradiated (*d*) samples, insets are scaling bars for height level in nm for the AFM micrographs

amorphous. The observed surface modification in the form of hillock-like features is evident for the two highest ion fluences.

A similar trend of RMS roughness increase in 100 MeV Au ion irradiated InP (111) surfaces at room temperature was observed by Singh et al. [103]. They attributed this to thermal spike induced effects and subsequent relaxation. In their observations for irradiation at lower temperature (96 K) the increase in roughness was less pronounced than at room temperature, due to the suppression of track formation at 96 K because of the high thermal conductivity of InP at that temperature. As indicated by our TEM observations, each impinging 200 MeV Au ion creates a single track with *core width* of ~ 5 nm. Our HRTEM observations (Fig. 13) showed that the ion tracks might not be amorphous in nature so that, in order to render an area of InP amorphous, multiple ion impacts and track overlap may be required, thus the process of amorphization proceeds with the increasing ion fluence as statistically expected [63, 104], i.e., the amorphous fraction of material must be expected to increase with increasing fluence. The multiple ion impact process required for amorphization in SHI irradiated InP was also reported by O'Herre et al. [53] for 250 MeV Xe irradiated InP where the authors used a simple Gibbons overlap model [104, 105] to fit their $\Delta\chi_{\min}$ data and inferred that at least 3 to 4 ions must impact the same area to produce an amorphous material. This is in general accord with our observations. At $\leqslant 5.0 \cdot 10^{13}$ cm^{-2} an InP surface will be completely amorphized. The observed drastic roughening of the surface after complete amorphization can generally be attributed to the ion-induced plastic deformation phenomenon which invokes the difference in the final elastic and transport constants of the completely amorphized surface from these for crystalline or heavily disordered material.

After complete amorphization, subsequent impinging ions now impact a surface which is in a completely different state than the crystalline surface, whose difference in the final elastic and transport properties may well in turn affect the structural relaxation through stress build-up due to the transient tracks formed in the amorphous material and the associated plastic deformation [106]. For example, it is well known that for the case of metallic glasses (where the first observation of ion-induced plastic deformation was made in the early 1980s) there is a small $\sim 2\%$ difference in densities between the amorphous phases relative to their crystalline counterparts. However, the differences in both the bulk and shear moduli are larger than $\sim 7\%$ and ~ 30 to 50%, respectively [107]. The elastic softening (reduction in elastic constants relative to that of crystalline phase) in amorphous tetrahedral semiconductors (including both elemental and III–V semiconductors such as InP) can be comparable in magnitude and even higher as they have similar origins to that of metallic glasses, i.e., the internal atomic displacements and the existence of a free volume in amorphous phases or internal relaxation process in the disordered atomic network [108]. Theoretical calculations predicted elastic softening for both elemental and compound semiconductors upon amorphization which can be varied over a wide range (from ~ 5 to 50%) depending on the network model and the atomic interaction potential [109, 110]. Therefore softening of elastic moduli is a generic property in both elemental and compound semiconductors [111]. It is not yet clear what exact factors define the magnitudes of the elastic softening effects for amorphous states, nor what features of atomic interactions are important in this respect [112]. However, substantial elastic softening of $\sim 20-50\%$ of both the bulk (Young's) and the shear elastic moduli has been experimentally observed for amorphous phases of different elemental semiconductors such as Si and Ge [95, 96, 113] and compound semiconductors such as GaAs [114], GaSb [112], and GaP [115]. This reduction in elastic constants is expected to greatly affect the elastic behavior of irradiated semiconductors after complete amorphization which can be manifested in the large surface roughening as in our observations. To our knowledge there exists no reliable, comprehensive or experimental data for the elastic moduli or constants in amorphous InP. This makes any quantification of the ion-induced plastic deformation in that material a difficult and challenging problem.

2.3. Summary. The SHI irradiation of InP leads to large nanoscale topographical changes of the surface after ion fluences sufficient to cause complete amorphization of the surface. SHI surface ion tracks are pit-like features and not well-defined features in that material. The large increase of RMS roughness of the surface after ion fluences sufficient to cause complete amorphization of the surface suggests the role of SHI induced plastic phenomena associated with the complete change of the surface properties upon reaching complete amorphous state.

3. INFLUENCE OF PREVIOUS IRRADIATION BY HIGH-ENERGY ELECTRONS ON TRACK FORMATION IN InP AND GaAs UNDER SHI IRRADIATION

During a few last decades of years, the creation of a new technologies with the use of nanostructure began to develop with high efficiency for fundamental studies and applications practically in all the industrial countries. The nanoclusters, nanowires, and nano- and microregular structures which can modify electronic, magnetic, quantum, and optical properties of solids provide new possibilities for the development of an optoelectronics and nanoelectronics and for other important areas of industry. As was mentioned above, one of the ways of nanometer structuring of solids is their irradiation with swift heavy ions. Under such an irradiation the tracks could be formed in the form of a nanometer cylinders or cluster chains with a modified structure embedded into the undamaged matrix. The mechanisms of the track formation under superhigh levels of the crystal electronic subsystem excitations are not clarified in detail until now. The Thermal Spike model is more often used to explain track formation or it is absent in materials under irradiation by high-level ionization energy loss particles [24, 116–118].

3.1. Irradiation of InP and GaAs by 4 and 25 MeV Electrons, and 253 MeV ^{86}Kr and 710 MeV ^{209}Bi [119–127]. The advanced model of thermal spike was presented in the previous articles [122, 123]. Here it is better to repeat the discussion about this model, i.e., to understand which part of the ion energy loss was used for the thermal spike formation (the heating of cylindrical volume around the ion trajectory, with the temperature higher melting or evaporation temperatures, i.e., creation of ion track). This process is determined by electron–phonon coupling constant g characterizing the efficiency of the energy transfer from the excited «hot» electrons to the lattice atoms. The track formation in insulators, semiconductors, amorphous materials, metals, and metallic alloys is observed when the electron energy losses of an ion exceed a certain threshold value $E_{\rm inel}^{\rm thres}$, which is determined by an irradiated material type and its structural features. For semiconductors the value of $E_{\rm inel}^{\rm thres}$ essentially exceeds the corresponding values for insulators and could be more than $E_{\rm inel}^{\rm thres} > 30$ keV/nm.

However, it was demonstrated that track formation in previously disordered InP is possible at $E_{\rm inel}^{\rm thres} \approx 13$ keV/nm [128, 129]. It is very likely that disordering can modify electronic properties of the material thus changing a value of the electron–phonon coupling constant g. The modifying of electronic properties of the crystal due to the controllable embedding of the damages by light particles irradiation could be one of the ways of $E_{\rm inel}^{\rm thres}$ reducing.

The experimental studies of radiation effects in single crystals GaAs and InP were the following ones [119–121, 124–127]. First series of the samples of [100]-oriented n-type GaAs and InP single crystals with 1×1 cm sizes and thickness of ~ 300 μm were irradiated with $E_e = 4$ MeV electrons to a fluence of $(F_e \times t) = 4.0 \cdot 10^{17}$ cm^{-2}. After that, the previously irradiated with electrons samples were bombarded with 710 MeV ^{209}Bi ions up to a fluence of $(F_{\rm Bi} \times t) = 1.0 \cdot 10^{12}$ cm^{-2}. The SEM studies of area near the Bregg peak (the area with the maximum of elastic energy loss and zone of ion stopping) have shown that the processes of individual track overlapping took place, i.e., the diameter of track near the end of projected range is more than $D = 1/[(F_{\rm Bi} \times t)]^{1/2} > 100$ Å. Second series of the single-crystal GaAs and InP samples were irradiated with 23 MeV electrons up to a fluence of $(F_e \times t) = (3.0 \pm 0.5) \cdot 10^{17}$ cm^{-2}. Then a half of the surface area of electron irradiated samples were covered by a nickel foil with the thickness exceeding ion projected range, and the samples were irradiated with 253 MeV ^{86}Kr ions to a fluence of $(F_{\rm Kr} \times t) = 1.3 \cdot 10^{14}$ cm^{-2}. At this fluence the overlapping of individual ion tracks takes place. The temperature of both the series of samples does not exceed 50°C during the electron and ion irradiations. Surface topography of samples was investigated using the scanning electron microscope S-806 (Hitachi production) and atomic force microscope «Femtoscan 001» (SEM and AFM methods).

Depth distribution of the damage was revealed by the selective chemical etching of the crystals cleaved perpendicular to the sample surface (practically cross-section technique). Then the prepared in such a way samples were observed using the optical microscope «Leica INM-100».

The parameters characterizing ion interactions with GaAs and InP were calculated using the SRIM-2007 computer code [130, 131]. The special computer code was written and used for the calculations of the cross section of damage production and inelastic energy loss of electron at these semiconductors.

The main calculated parameters of the process of ion and electron interactions with GaAs and InP are presented in Tables 1 and 2.

Table 1. **Parameters of electron interaction with GaAs and InP crystals**

Crystal	E_e, MeV	Φ_e, cm^2	σ_e, dpa · cm^2	D_e, dpa	$E^{\mathrm{AIII}}_{\mathrm{max}}$, keV	$E^{\mathrm{BV}}_{\mathrm{max}}$, keV	$E^{\mathrm{AIII}}_{\mathrm{mean}}$, eV	$E^{\mathrm{BV}}_{\mathrm{mean}}$, eV
GaAs	23	$(3 \pm 1) \cdot 10^{17}$	$3.1 \cdot 10^{-22}$	$9.3 \cdot 10^{-5}$	16.8	15.7	124	124
GaAs	4	$4 \cdot 10^{17}$	$1.45 \cdot 10^{-22}$	$5.8 \cdot 10^{-5}$	0.61	0.57	59.6	58.5
InP	23	$(3 \pm 1) \cdot 10^{17}$	$3.12 \cdot 10^{-22}$	$9.4 \cdot 10^{-5}$	10.2	37.9	127	136

Note: E_e — electron energy; Φ_e — electron fluence; σ_e — defect formation cross sections; $D_e = \sigma_e \times F_e$ — damage dose; $E^{\mathrm{AIII}}_{\mathrm{max}}$ and $E^{\mathrm{BV}}_{\mathrm{max}}$ maximum and $E^{\mathrm{AIII}}_{\mathrm{mean}}$ and $E^{\mathrm{BV}}_{\mathrm{mean}}$ — their mean energies of displaced atoms.

Table 2. **Parameters of ion interaction with GaAs and InP**

Crystal	R_p, μm	E_{inel}, keV/nm	σ $(z = 0)$, (dpa · cm^2)/ion	σ $(z \approx R_p)$, (dpa · cm^2)/ion	D $(z = 0)$, dpa	D $(z \approx R_p)$, dpa	$S^{\mathrm{AIII}}_{\mathrm{Kr}}$, atom/ion	$S^{\mathrm{BV}}_{\mathrm{Kr}}$, atom/ion
^{209}Bi ($F_{\mathrm{Bi}} = 710$ MeV, $(F_{\mathrm{Bi}} \times t) = 1.0 \cdot 10^{12}$ cm^{-2})								
GaAs	30.6	35.2	$1.96 \cdot 10^{-16}$	$6.8 \cdot 10^{-15}$	$1.96 \cdot 10^{-4}$	$6.8 \cdot 10^{-3}$		
^{86}Kr ($E_{\mathrm{Kr}} = 253$ MeV, $(F_{\mathrm{Kr}} \times t) = 1.3 \cdot 10^{14}$ cm^{-2})								
GaAs	23.3	15.8	$6.7 \cdot 10^{-17}$	$3.2 \cdot 10^{-15}$	$8.7 \cdot 10^{-3}$	$4.2 \cdot 10^{-1}$	0.016	0.017
InP	25.5	12.6	$5.3 \cdot 10^{-17}$	$2.8 \cdot 10^{-15}$	$6.9 \cdot 10^{-3}$	$3.6 \cdot 10^{-1}$	0.017	0.03

Note: R_p — ion ranges; $E_{\mathrm{inel}} = -(\partial E/\partial z)_{\mathrm{inel}}$ — specific inelastic energy loss in the layer near the surface; σ $(x = 0)$ and $(x \approx R_p)$ — defect formation cross sections near the surface and in the Bragg peak, correspondingly; D $(z = 0)$ and D $(z \approx R_p)$ — corresponding damage doses and $S^{\mathrm{AIII}}_{\mathrm{Kr}}$ and $S^{\mathrm{BV}}_{\mathrm{Kr}}$ — sputtering coefficients [130, 131].

As our AFM data show, the electron irradiation does not change surface topography of InP and GaAs samples. The ^{86}Kr ion irradiation leads to some smoothing of the surface relief of the virgin and electron irradiated crystals. At the same time, the «ripples» appear on the irradiated part of InP surface, and (in the case of InP) cones and needles arise (Fig. 35, *b* and Fig. 39). It seems to be due to the nonuniform sputtering during the irradiation.

The thicknesses of sputtered layers ($\Delta H^{\mathrm{InP,GaAs}}_{\mathrm{Kr}}$) of InP and GaAs, irradiated by ^{86}Kr ions for the irradiation conditions, presented above, were calculated using the model of elastic cascade sputtering [61] and expression:

$$\Delta H^{\mathrm{InP,GaAs}}_{\mathrm{Kr}} = \left[S^{\mathrm{AIII}}_{\mathrm{Kr}} + S^{\mathrm{BV}}_{\mathrm{Kr}}\right] \times (F_{\mathrm{Kr}} \times t)/N^{\mathrm{InP,GaAs}}_{\mathrm{atom}}, \tag{3.1}$$

where $N^{\mathrm{InP,GaAs}}_{\mathrm{atom}}$ — atomic densities of InP and GaAs single crystals, correspondingly. Then the thicknesses of sputtering layers have values: $\Delta H^{\mathrm{InP}}_{\mathrm{Kr}} = 9.8 \cdot 10^{-4}$ and $\Delta H^{\mathrm{GaAs}}_{\mathrm{Kr}} = 9.6 \cdot 10^{-4}$ nm. We conclude that inelastic sputtering [131] takes place during the 253 MeV krypton irradiation due to the high inelastic energy loss $E^{\mathrm{Kr}}_{\mathrm{inel}}$ equal to 12.6 keV/nm for InP and 15.8 keV/nm for GaAs.

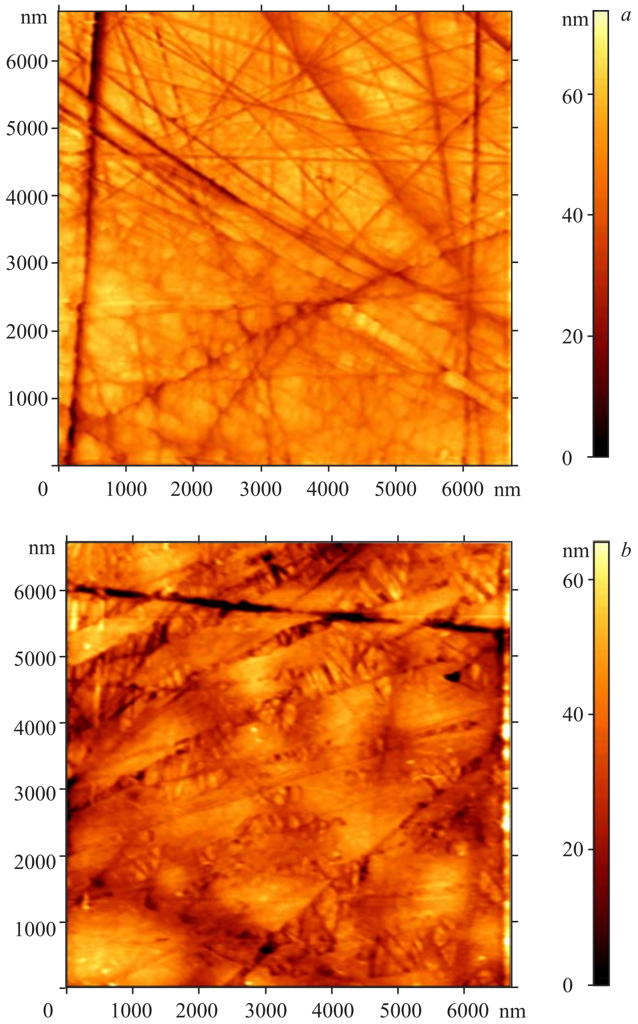

Fig. 35. Surface structure on InP single crystal. *a*) Surface of InP crystal, irradiated by only electrons ($E_e = 23$ MeV, $(F_e \times t) = 3.0 \cdot 10^{17}$ cm^{-2}). *b*) Surface of InP crystal, irradiated with electrons ($E_e = 23$ MeV, $(F_e \times t) = 3.0 \cdot 10^{17}$ cm^{-2}) and ^{86}Kr ions ($E_{\mathrm{Kr}} = 253$ MeV, $(F_{\mathrm{Kr}} \times t) = 1.3 \cdot 10^{14}$ cm^{-2}). AFM images were obtained by using AFM method

For GaAs crystals bombarded with electrons and ^{209}Bi ions, the beginning of the flaking phenomenon has been fixed in our experiments. The region with strong mechanical stress which produced the damaging layer with microcracks has

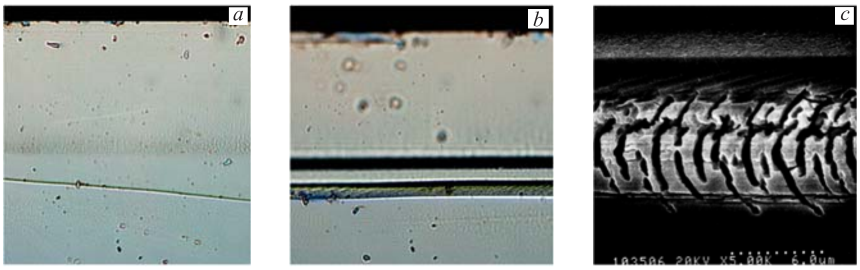

Fig. 36. Radiation damages revealed by selective chemical etching of GaAs samples cleaved perpendicular to the sample surface. *a*) A sample irradiated with only ^{209}Bi ions ($E^{\rm Bi} =$ 710 MeV, $(F_{\rm Bi} \times t) = 1.0 \cdot 10^{12}$ cm^{-2}). *b*) Sample irradiated with electrons ($E_e = 4$ MeV, $(F_e \times t) = 4.0 \cdot 10^{17}$ cm^{-2}) and ^{209}Bi ions ($E_{\rm Bi} = 710$ MeV, $(F_{\rm Bi} \times t) = 1.0 \cdot 10^{12}$ cm^{-2}). *c*) Image with a higher magnification of the microcrack region indicated by arrow in Fig. 35, *b*. Vertical bars in plots *a* and *b* show ion projected range $R_p^{\rm Bi} = (30.6 \pm 1.0)$ μm

been revealed on the cleave of the double-irradiated sample at depths exceeding the ion projected range (see Fig. 36).

We have revealed also that double irradiation of InP and GaAs with electrons and ^{86}Kr ions leads to the swelling of double-irradiated crystal parts and to the formation of the microcracks on the surface and breaks and cleaves in the near-surface layers (Figs. 37–39). In Fig. 39, *a* and *b* the surface of InP with the individual crystallites, produced by swift heavy-ion irradiation, is presented. For

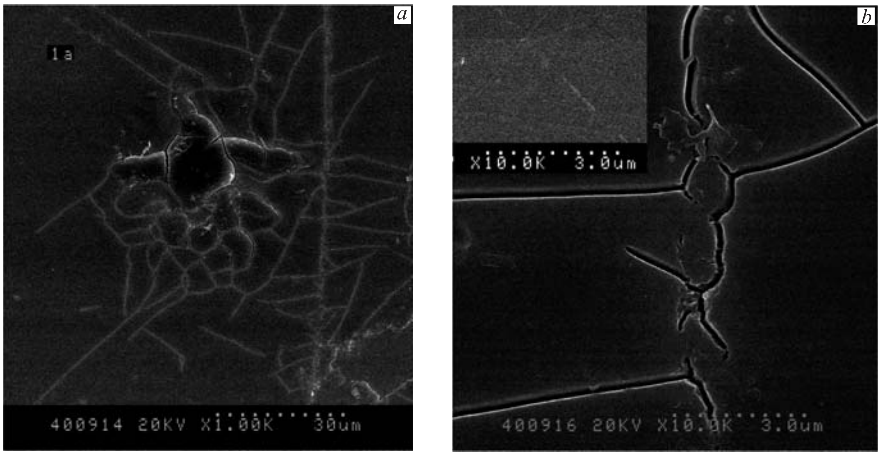

Fig. 37. Microcracks on the GaAs crystal surface irradiated with electrons ($E_e = 23$ MeV, $(F_e \times t) = 3.0 \cdot 10^{17}$ cm^{-2}) and Kr ions ($E_{\rm Kr} = 253$ MeV, $(F_{\rm Kr} \times t) = 1.3 \cdot 10^{14}$ cm^{-2}). Figures *a* and *b* are scanning electron microscopy images with different magnifications

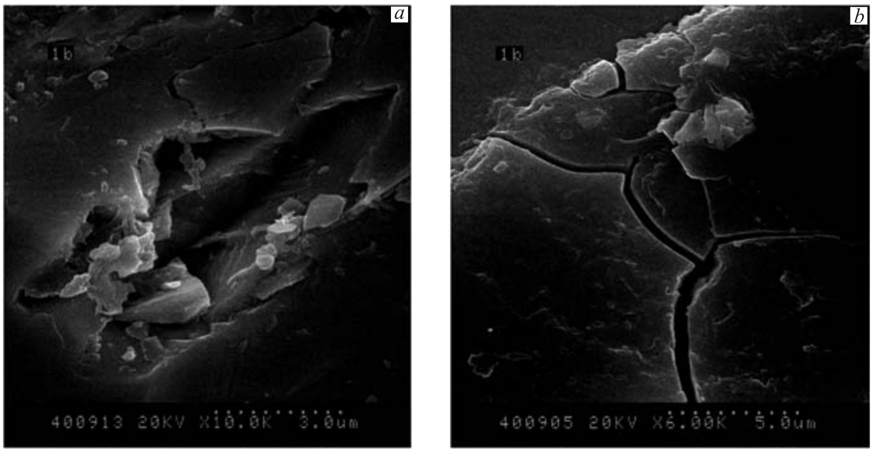

Fig. 38. Cracks and breaks on the InP surface between unirradiated by ions surface (top part of photo *b*) and part irradiated by electrons ($E_e = 23$ MeV, $(F_e \times t) = 3.0 \cdot 10^{17}$ cm^{-2}) and ^{86}Kr ions ($E_{\mathrm{Kr}} = 253$ MeV, $(F_{\mathrm{Kr}} \times t) = 1.3 \cdot 10^{14}$ cm^2)

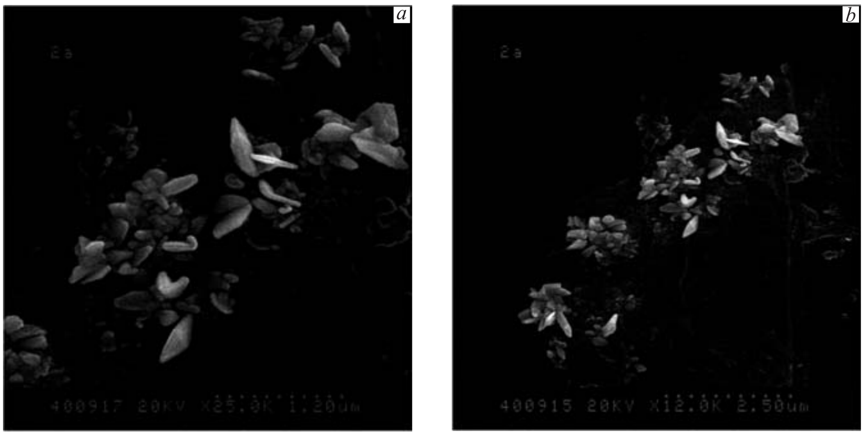

Fig. 39. The irradiated by electrons ($E_e = 23$ MeV, $(F_e \times t) = 3.0 \cdot 10^{17}$ cm^{-2}) and ^{86}Kr ions ($E_{\mathrm{Kr}} = 253$ MeV, $(F_{\mathrm{Kr}} \times t) = 1.3 \cdot 10^{14}$ cm^{-2}) surfaces of InP with the individual crystallites. Magnifications in plots *a* and *b* are ×25000 and ×12500, correspondingly

the explanation of creation of individual crystallites on the twice irradiated surface of InP single crystal it is possible to use the comments to production of semi-spherical hillocks of Si irradiated surface, i.e., the specific sputtering-evaporation mechanism something like evaporation and following vacuum precipitation of evaporated atoms, because the angle distribution of evaporated atoms versus the angle Θ has the form:

$$\frac{N(\Theta)}{N(0)} \approx \cos(\Theta). \tag{3.2}$$

The swelling effect has been observed in [62] for the ionic crystals (LiF and CaF_2) and covalent crystals (SiO_2, $Y_3Fe_5O_{12}$, and $Gd_3Ga_5O_{12}$) caused by influence of high-energy ions, where at fluences of about 10^{13} cm^{-2} sometimes the irradiated layer of insulators cleaved out of the underlying undamaged crystal. In our experiment, the level of mechanical stresses in the semiconductors InP and GaAs irradiated with much higher fluence $F_{\mathrm{Kr}} \times t = 1.3 \cdot 10^{14}$ cm^{-2}, is found to be insufficient to destroy the material. However, the preliminary disordering of crystals by electron irradiation facilitates destruction processes during the following swift ion irradiation.

Here AIII — chemical elements of IIId group of Mendeleev Periodical Table: Ga and In, and BV — elements of Vth group of Mendeleev Periodical Table: P and As.

The observed effects could be explained by the increasing of the volume of double-irradiated parts due to the amorphization process and by the mechanical stresses appearance in the region of swift ions stopping. The parts of the samples covered by a metal foil were not influenced by Kr ions, and in the irradiated parts the ions have been stopped in the crystal at the projected range depth. The free expansion of ion-irradiated volume was limited by neighboring undamaged region, and the irradiated parts are swelled out over the sample surface. The mechanical stresses appear leading to the cracking of double irradiated material regions. As Tables 1 and 2 show, the damage dose due to electron irradiation of InP and GaAs crystals is much lower than damage dose due to ion irradiation. Nevertheless, the effects of swift ion bombardment of crystals previously irradiated with electrons are very considerable and unusual. One can see, using Tables 1 and 2, that the damage dose after electron irradiation in InP and GaAs single crystals (as example, in InP: $D_e^{\mathrm{InP}}(z) = 9.4 \cdot 10^{-5}$ dpa) is much less than the damage dose after irradiation by Kr ions ($D_{\mathrm{Kr}}^{\mathrm{InP}}(z = 0) = 6.9 \cdot 10^{-3}$ dpa and $D_{\mathrm{Kr}}^{\mathrm{GaAs}}(z = 0) = 8.7 \cdot 10^{-3}$ dpa) even near the surfaces, and in Bragg peak (maximum of damage creation) the damage dose is about $7 \cdot 10^3$ times more than after electron irradiation. Damage dose after irradiation by Bi ions is practically two times more near the surface of GaAs single crystal (as an example, $D_e^{\mathrm{GaAs}}(z = 0) = 9.3 \cdot 10^{-5}$ dpa and $D_{\mathrm{Bi}}^{\mathrm{GaAs}}(z = 0) = 1.96 \cdot 10^{-4}$ dpa), and in Bragg peak the damage dose after Bi ions irradiation is practically by two orders more ($D_{\mathrm{Bi}}^{\mathrm{GaAs}}(z = R_p) = 6.8 \cdot 10^{-3}$ dpa). Maybe so high damage dose after irradiation by ^{86}Kr ions with the intensification of damage effect creation after previous electron irradiation is a reason that it was impossible to get good quality transversal split of twice GaAs irradiated by smaller dose of Bi and it allows one to observe cracks only in a layer over projected range of Bi ions (see Fig. 36, *b*, *c*).

To explain the influence of electron irradiation facilitating mechanical destroying of the samples, we have evaluated the sensitivity of the materials under consideration to the electronic energy losses. This property is defined by the parameter $\eta = Q/\Delta H_f$ [132]. Here ΔH_f is the latent heat of fusion, $Q = 0.63E_{\mathrm{inel}}/(\pi\lambda^2)$ is the mean energy density deposited by the ion in a cylinder of radius λ equal to the electron mean free path. If $\eta > \eta_{\mathrm{cr1}} = 1.3$, the lattice is considered as inelastic energy losses sensitive, if $\eta < \eta_{\mathrm{cr2}} = 0.7$, it is insensitive to inelastic energy losses. In the range of $\eta_{\mathrm{cr2}} \leqslant \eta \leqslant \eta_{\mathrm{cr1}}$ the lack of precision of used parameters does not allow any definite conclusion. The calculated mean distances between isolated point defects generated by electron irradiation were chosen as the electron mean free path. The wave functions of free electrons in an ideal crystal represent translational invariant Bloch functions [117, 118]. The presence of vacancies breaks crystal periodicity, and this approximation seems to be reasonable. The mean distances between point defects generated by electron irradiations are equal to 12.1 nm and 12.5 nm for InP and GaAs, correspondingly. These values are comparable with electron mean free paths in metals [133]. As calculations show, for InP $\eta_{\mathrm{Kr}} = 0.88$. For GaAs we have $\eta_{\mathrm{Kr}} = 0.83$, $\eta_{\mathrm{Bi}} = 1.34$ [124]. In all cases η exceeds a lower limit of crystal sensitivity to electronic energy losses $\eta_{\mathrm{cr}} = 0.7$.

In the review [134], the results describing the isotopic disorder influence on kinetic coefficients of semiconductors and alkali-halide crystals (diamond ${}^{12}\mathrm{C}_{1-x}{}^{13}\mathrm{C}_x$, ${}^{7}\mathrm{Li}_{1-x}{}^{6}\mathrm{Li}_x\mathrm{F}$, ${}^{70}\mathrm{Ge}_x{}^{\mathrm{nat}}\mathrm{Ge}_{1-x}$) and models for the calculation of these coefficients changes are presented. Moreover, ^{13}C concentration in a diamond increases from 0.001 up to 10% (four orders of magnitude) at the room temperature ($\sim$ 300 K), the thermal conductivity coefficient decreases in four times. Significant thermal conductivity changes are caused by the change of an isotope atomic weight of lattice atoms (lattice atoms of ^{12}C replacement on isotope atoms ^{13}C, i.e., the relative change of atomic height is about 8% only). In the case of electron irradiation at damage rate $D_e \sim 9.3 \cdot 10^{-5}$ dpa vacancies are formed in InP and GaAs crystals being the centers of excited electron scattering and affecting phonon propagation. This could reduce electron and lattice thermal conductivities and increase the lifetime of an overheated region around heavy-ion trajectories, thus causing additional defects formation and amorphization of the irradiated layer of the crystal.

The influence of previous disordering by MeV electron irradiation on the effects of swift ion interaction with InP and GaAs crystals has been studied [119, 121, 122, 124–126]. It has been shown that previous electron irradiations lead to macrodefect formation during the following irradiation of InP and GaAs with such ions. For low ion irradiation fluences (^{209}Bi ions, $E_{\mathrm{Bi}} = 710$ MeV, $(F_{\mathrm{Bi}} \times t) = 1.0 \cdot 10^{12}$ cm^{-2}) the layer with macrodefects in the form of cracks is formed at the depth near the ion end-of-range. With irradiation fluence increasing (^{86}Kr ions, $E_{\mathrm{Kr}} = 253$ MeV, $(F_{\mathrm{Kr}} \times t) = 1.3 \cdot 10^{14}$ cm^{-2}) the macrodefects evolve, microcracks and breaks are formed on the surface of InP and GaAs crystals [119–127].

We present shortly the main results in the conclusion of the first part of the review. The results of heavy-ion irradiation in the inelastic energy loss region on the structure of some metals, metallic and amorphous alloys, HOPG and semiconductor single crystals Si, GaAs, and InP are presented. It was shown that sputtering coefficient (yield) strongly depends on the state of the irradiated surface and on the density of defects in the crystalline target, whether it is present before the irradiation (point defects, extended defects, etc.) or as a result of accumulation and build-up of defects due to irradiation. The presence of these defects essentially increases the influence of inelastic energy losses of the high-energy heavy ion and hence the sputtering coefficients. Strong inhomogeneity of the sputtering of surfaces by high-energy heavy ions is thus expected. It was shown on the samples of stainless steel and Si, irradiated by swift heavy ions, very clear. The sputtering at the grain boundaries is much greater than at surfaces of grain bodies.

The importance of the sputtering problem in the fields of nuclear engineering, high-energy heavy-ion implantation and processing of novel materials makes it necessary to continue the efforts of similar experimental and theoretical studies on swift heavy-ion irradiation to elucidate the various aspects of the phenomenon.

Thus, the experimental research on swift heavy-ion action on the surface of metals, metallic alloys, amorphous alloys and HOPG in inelastic energy loss region was carried out. The explanation of experimental results is given, too. On the base of data obtained for Ni, Au, and HOPG, we have concluded that track formation and consequently the high evaporation (sputtering) coefficients take place in the case of high-disordered systems or in materials with relatively low concentration of free electrons (like dielectrics and some semiconductors). It has been shown that for conductive materials, when the condition $\tau_L \ll \tau_h$ takes place in low-defect zone, the lattice atoms around the swift heavy-ion trajectory are cold and do not create a hot track. The condition $\tau_L \ll \tau_h$ is disturbed on the boundaries between grains and also in the area with high defect concentration, as one can see for Ni previously irradiated with high fluence (using the so-called «step» method, see Fig. 37) and for previously strongly deformed Au. As a result, when fast heavy ions pass through such areas, hot tracks are created, and the target atom evaporation could take place.

Using the observed surface effects at various solids under irradiation by swift heavy ions with different inelastic energy loss $E_{\text{inel}} = -(\partial E/\partial z)_{\text{inel}}$ and most experimental results of the first part of the review, one can conclude that practically for all materials sputtering coefficients have values higher than follows from elastic sputtering model [135–137].

Expression (1) [138] can be used for the calculation of lattice temperature at solids with high concentration of defects or amorphous ones as was shown above. It is necessary to attract the models of inelastic sputtering [131] with the calculation of temperature effects on the base of Thermal Spike model [17–21, 34, 116–118, 137] for the description of results.

There are some small clusters or better to write small nano- (practically invisible, because here there is low magnification) and micro- (visible) crystallites of InP in Fig. 39, *a*, *b*. Such crystallites could be created under the processes of surface sputtering of InP crystalline semiconductor (see Eqs. (3.1) and (3.2)).

4. SWIFT HEAVY-ION IRRADIATION OF FURTHER SELECTED COMPOUND CRYSTALS. TEM OBSERVATION OF SHI TRACKS IN FURTHER SELECTED COMPOUND CRYSTALS: APATITE AND MONAZITE

Let us discuss TEM studies of 200 MeV Au ion induced tracks in InP, it is the repetitive nature of each registered track, i.e., the registration of disorder in the form of nanoshperes. At a macroscopic continuum level (c.f. the Thermal Spike) we have drawn attention to the fact that, in a classical hydrodynamical picture, this is the equivalent of the need to invoke the well-known Rayleigh instability which implies minimization of interface energy [75].

The hydrodynamical interpretation in SHI interaction with solids can quite generally be very rewarding. For example, it has been used successfully to explain the formation of fullerene at graphite surfaces irradiated by SHI, and also the appearance of narrow «plumes» of sputtered matter ejected from insulating solids. Also significant is the observation, we reported that ion tracks in InP may «interact» with each other if they are spatially close, which is to suggest that the defect «halo» produced in the trajectory of the second ion at least overlaps the defect halo of the first during tracks registration, though neither is sharply defined. And once again — in the limit — multiple track interaction and overlap may give rise to a continuous amorphous layer for the highest ion fluences. It follows directly that the only full explanation of all of our observations lies in the generation of target-specific, point and extended defects, especially the former, and their overall behaviour and dynamic at the atomistic level. We therefore conclude that, for the registration of latent ion tracks in crystalline targets, long standing arguments as to whether the macroscopic Coulomb Explosion or Thermal Spike models will be applied, are now rendered largely redundant. It has already been clearly pointed out that some broad overview of track formation is required such that any *new* «*spike*» must be at least a hybrid of both Thermal and Coulomb Explosion spikes [37].

And sometimes there are even contributions to stopping, and therefore to ranges, from other induced transient phenomena — such as plasma generation [140]. For example, in the case of cluster ion projectiles there are also both nuclear and electronic «*vicinage*» effects (i.e., *vicinity* effects; neighbouring atomistic influences which affects the energy deposition processes) [141]. Good examples of the very basic requirement for fundamental considerations of defect physics in explaining track registration include Si and graphite crystals in which fission fragment or SHI tracks were never found! And recovery is complete in these materials. In Si, for example, this can be clearly attributed to the divacancy [142] and its action during total homoepitaxial recovery within the transient energy deposition time after SHI passage. On the other hand, for materials such as fluorite ($\mathrm{CaF_2}$), there can be no doubt that ion track registration is due to dominant absorption of electronic energy on the F anion cubic sublattice [143–147] as a precursor to the «active» defect in that material which is the $\langle 001\rangle$ directed interstitial crowdion or the V_k centre, that ultimately carries the momentum and energy from the projectile and which is also responsible for the intermittent track structure, in particular, the cuboidal «shaping» of the intermittent Ca segments by the Foreman mechanism [148].

Fleischer [149] has recently argued, on the basis of the lengths of etched natural fission and alpha-particle recoil tracks, that the Thermal Spike model is actually wrong, and that all track lengths and structure are related to primary ionization alone.

However, this may be not correct. Certainly, in ionic crystalline targets, and some others, the nature of the track is entirely due to the deposited energy directly returned to the lattice and not to full ionization, the energy loss of the projectile returns to the lattice in the form of nonradiative transitions in self-annihilation of electron-hole pairs and the self-trapped exciton which decays into V_k centre in $\mathrm{CaF_2}$, for example (in this case it is self-trapped hole on two anions to give an asymmetric complex, i.e., a doubly charged molecule F_2^- or $(F^-–F^-)$ with the bond axis extending along a closed packed $\langle 001\rangle$ anion row in the anion sublattice of $\mathrm{CaF_2}$, they are diffusive and mobile at room temperature along $\langle 001\rangle$ directions of the anion sublattice) [150]. It is also worth remarking here, however, that the Thermal Spike is not entirely without its didactic value, since it does give some classical macroscopic explanation for the apparent widths of a latent tracks, which must necessarily scale in some way with the density of energy deposited in the crystal. Whilst it is obvious to some extent that the only valid explanation of the formation and annealing of latent ion tracks in crystals must be atomistic, and quantum mechanical throughout (the primary electron–phonon interaction, for example), it is to be acknowledged that this requires a major «*mind shift*» — an intellectual step from macroscopic to microscopic, atomistic physics [151, 152]. For example, Szenes is a strong proponent of the Thermal Spike model [153–155], which relies upon equilibrium thermodynamics, classical values of the «continuum» heat conductivity (invariable with temperature and time), the Dulong–Petit law, and (*e*–*p*) coupling factor g as a free parameter.

Szenes also argues that there is no need to resort to an atomistic model, and that such a step is too difficult since our knowledge of target-specific defects and their behaviour is inadequate and they are complex in many systems. It would appear that this is currently and regrettably the majority point of view [65–67].

This raised an important question, namely, are our detailed TEM observations of intermittent 200 MeV Au ion tracks in InP unique to that material? Or do the fundamental propositions that track structure and annealing are «point» defects controlled process, that there is a dominance of surfaces and interfaces as nonsaturable sinks, hold up yet more generally? The decision was therefore taken to attempt, in the limited time available, to widen the experimental base still further by carrying out similar SHI irradiations on chemically and structurally different crystalline targets (apatite and monazite). Collaborations with workers in other laboratories were also initiated.

4.1. SHI Irradiated Apatite. The research world of particle tracks in solids is divided into two main parts; direct observations of latent tracks [156] as in this review and, correspondingly, observations of chemically etched tracks [27]. Observations of etched fission tracks by the more accessible technique of Transmission Optical Microscopy (TOM) essentially yield only two pieces of information. Firstly, there is the simple statistical information of the density of tracks. Secondly, it is possible to measure track lengths and their angular distribution — all other information on the defect condensed matter introduced in the energy loss process being permanently lost in the chemical etching «development» process. Geologists are able to use a comparison of «fossil» spontaneous fission events of ^{238}U with those induced by artificial slow-neutron induced fission of ^{235}U in order to «date» a mineral and therefore the rock containing it by measuring track «lengths» [157, 158]. And it is important to note that such lengths in fact are the combined lengths of the light and heavy fission fragments! Nevertheless, it is clear that a combination of TEM and TOM experimental work holds much promise, and because of this a cooperative research programme exists between workers at the ANU with Dr. R. Jonckheere and colleagues (TU-Bergakademie, Freiberg, Germany). Permission from these colleagues to reproduce yet unpublished joint results relevant to the work described in this thesis is most gratefully acknowledged. The mineral apatite $Ca_5(PO_4)_3$(F, Cl, OH) features centrally in fission track dating applications (Geochronology) and much more controversially, in Geothermometry, where geophysicists surprisingly seem to have omitted to consider the vital effects of ambient pressure on the kinetics of defects in fission track annealing [159, 160].

We primarily restrict ourselves here to observations relevant to the more immediate matter of comparison of tracks in fluoroapatite $Ca_5(PO_4)_3F$ with those in InP. In TEM kinematic diffraction conditions, observations reveal that tracks are sharp and similar to those seen in InP. In slightly thicker crystals, the effects of dynamical diffraction contrast with deviation vector s from the Bragg condition — diffraction vector g (progressively moving perpendicularly away from the extinction contour — the dark band in the micrograph) becomes more apparent in the track images (Fig. 40, *a*, *b*). In particular, it is clear that track images become markedly asymmetric (Fig. 41, *a*) though not necessarily in the

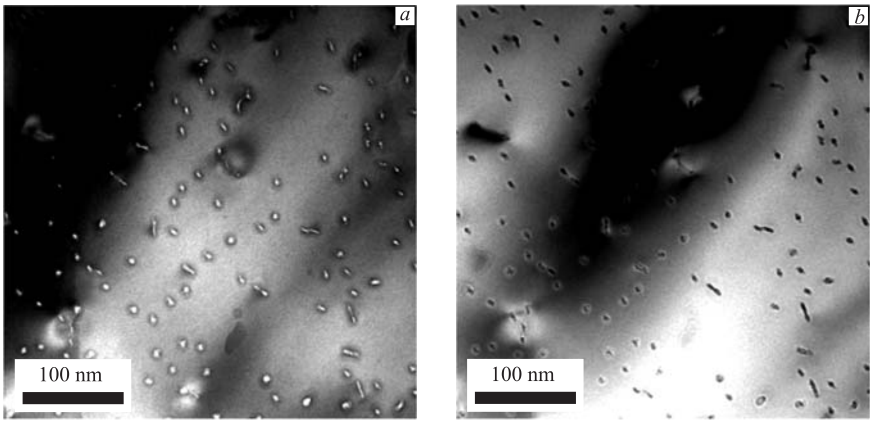

Fig. 40. 200 MeV Au irradiated apatite slightly tilted in TEM under-focused (*a*) and over-focused (*b*) conditions. The fluence is $5.0 \cdot 10^{10}$ cm^{-2}

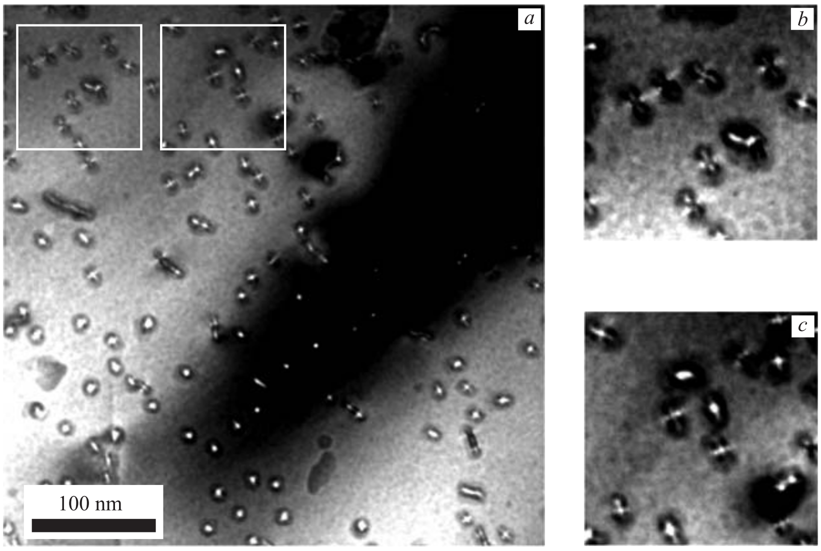

Fig. 41. *a*) 200 MeV Au ion tracks in apatite. Squares *b* and *c* are enlarged at the right, revealing the observed contrast of single tracks in detail

same direction of elongation. In addition, on occasions, these features are strongly enhanced if tracks are fortuitously close as shown in Fig. 41 for the two areas designated *a* and *b*.

On this occasion, however, by tilting the specimen in TEM we are able to reveal the tracks along their axes. In Fig. 42 the sample is tilted by 30° in TEM so that the lengthwise morphologies of tracks are clearly revealed. Here again we have segmented tracks as well as evidence for track bending appear as indicated by the arrows.

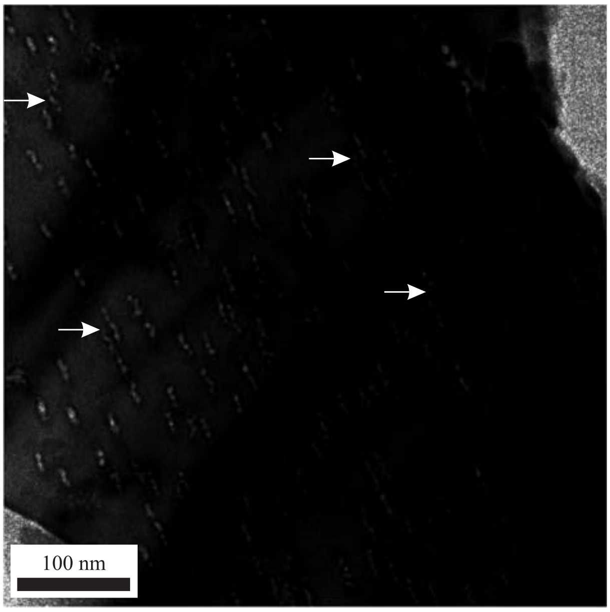

Fig. 42. Apatite sample tilted by 30° in TEM relative to the imaging electron beam, revealing the morphology of 200 MeV Au ion tracks. Arrows point to *bending* tracks

We once again have the familiar Fresnel effect in under- and over-focused TEM images for tilted samples (Fig. 43, *a*, *b*).

Higher magnification micrographs (Fig. 44, *a*, *b*) yield still more detailed information on track morphology.

From our observations, we can draw some specific conclusions:

1) Tracks are intermittent (segmented).

2) Tracks may «*interfere*» and «*bend*» toward each other if spatially close enough.

3) Track segments show a tendency towards polyhedral forms.

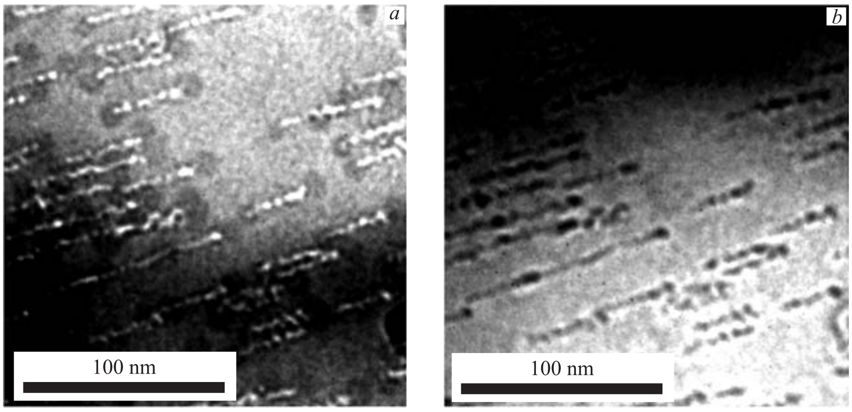

Fig. 43. 200 MeV Au ion tracks in apatite under-focused (*a*) and over-focused (*b*) in a sample tilted to 30° in the TEM

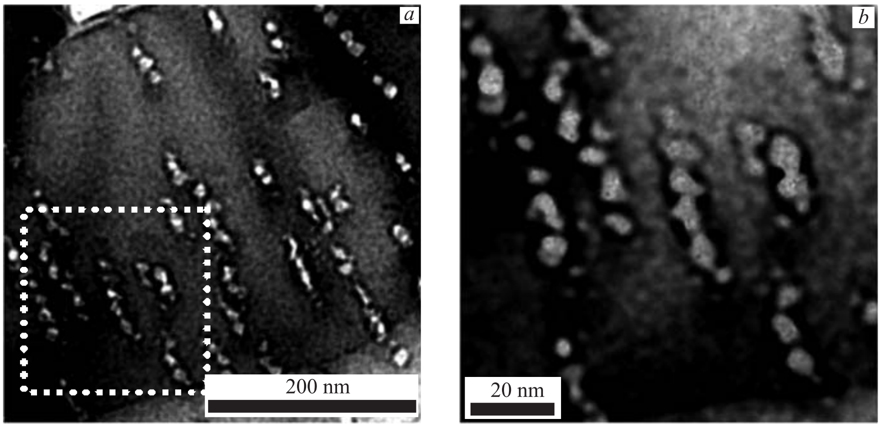

Fig. 44. *a*) TEM of 200 MeV Au ion tracks in apatite; *b*) high magnification of the tracks shown inside the dotted square in *a*, the sample has been tilted to 30° in TEM

These characteristics (1 and 2) are uncannily similar to those for ion tracks in InP, notwithstanding the different basic electronic binding in the two distinctively different crystallographic structures. It is also important to emphasize here that (i) whilst tracks in InP can anneal out completely either by direct heating or under the influence of the imaging electron beam, they do not do so completely in apatite, and (ii) track structure in both materials can be slowly modified as a natural concomitant of experimental TEM work.

Studies of tracks in apatite due to normal incidence irradiation with 30 MeV C_{60} ions have been carried out by Dunlop et al. [161], and although the electronic energy loss processes are considerably more complicated for a cluster projectile, the results being more gross and sharp, the observed tracks are similar to those for 200 MeV Au ion tracks in the same target. Thus, in Fig. 45, *a* and *b* we observe sharp polyhedral track morphology and also conjugal strain (dark contrast) with neighboring tracks. And again, the true segmental and intermittent nature along the tracks is better revealed by tilting the sample to $\sim 30^\circ$ in TEM (Fig. 45, *c*, *d*). The structure is real; it is not due to any vagary of depth-dependent diffraction contrast. The comparison of our tracks in InP with the cluster ion tracks in apatite is even more satisfactory when note is taken of their observations of the influence of the incident 300 keV electron beam. However, the authors [161] do

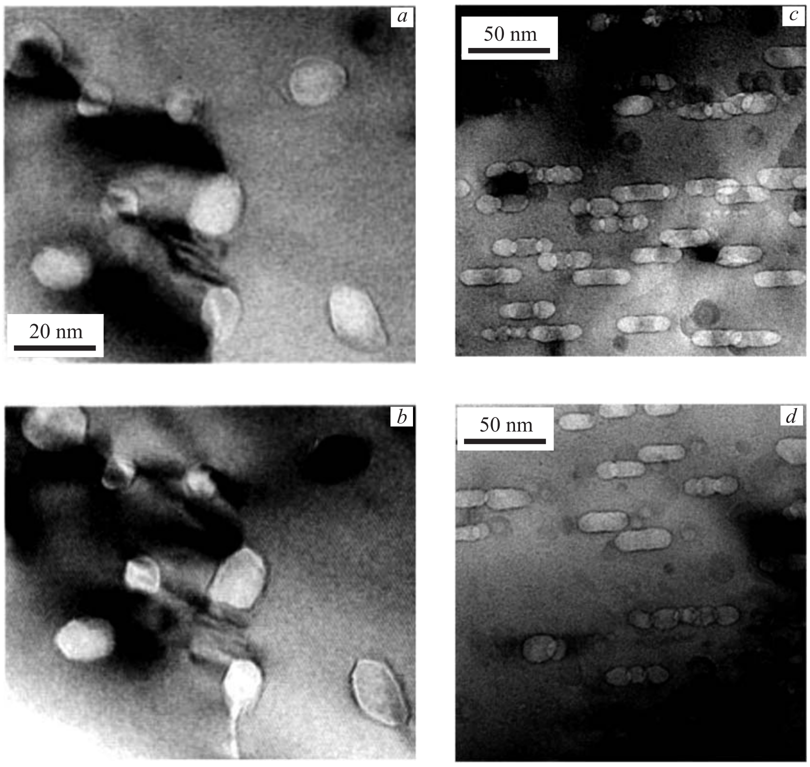

Fig. 45. TEM of apatite irradiated at RT at normal incidence with 30 MeV C_{60} cluster ions: *a*) just after introduction of the sample in TEM; *b*) after exposure to 300 keV electrons to a fluence of $\sim 3.37 \cdot 10^{21}$ cm^{-2}; *c*) sample is tilted 30° in TEM; *d*) closer TEM observation with the sample tilted 30° in the TEM, illustrating the intermittent nature of tracks in apatite [161]

not comment in detail on either the origin of intermittence or the morphology of tracks. However, we believe that the conclusions we make for InP can be carried over intact to the cluster ion stopping physics, and that moving point defects are the controlling feature both during track registration and afterwards.

4.2. SHI Irradiated Monazite. The mineral monazite was chosen for our track studies besides the apatite, simply because in its idealized chemical form ($CePO_4$) it can be considered as an apatite from which the hydroxyl group (OH) and all other anions (F and Cl) are removed, leaving only the phosphate (PO_4) groups. More naturally it occurs in a nonstoichiometric form (Ce, La, Nd, Th, U, Y) PO_4 and in certain geographical areas the isotopes of U are strongly present so that the mineral is detectable by its characteristic gamma radiation. In the present context it was our hope and expectation that track registration and track morphology might differ from that observed in fluoroapatite. Figure 46, *a*, *b* shows once again the sharp intermittency of 200 MeV Au ion tracks in monazite, and though now the polygonal structure of the segments is clearer and sharper than was the case in apatite.

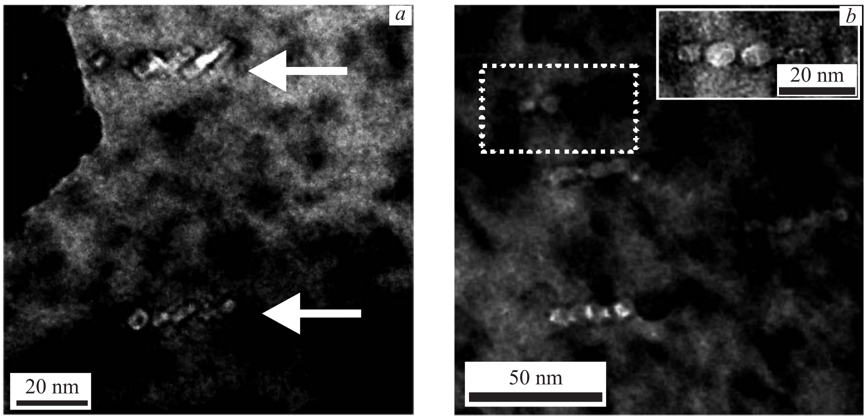

Fig. 46. TEM of 200 MeV Au ion tracks in monazite. *a*) Two ion tracks characterized by faceted segment. *b*) Observation of several ion tracks where the inset shows an enlarged image of single ion track

We have as yet no experimental results for higher ion fluence irradiations but we see no reason to suppose that track bending and interaction will not also occur in natural monazites. We note here the remarkable similarity of the tracks shown with those found earlier by Dunlop et al. [162, 163] for 30 MeV C_{60} cluster ions in fluorite (CaF_2) (see Fig. 47, *a*).

In the case of CaF_2, cited here, we have a clearer understanding of point-defects formation dynamics where one defect may dominate rather than a «*suite of point defects*» [152]. For example, from electron irradiation of CaF_2, which firstly

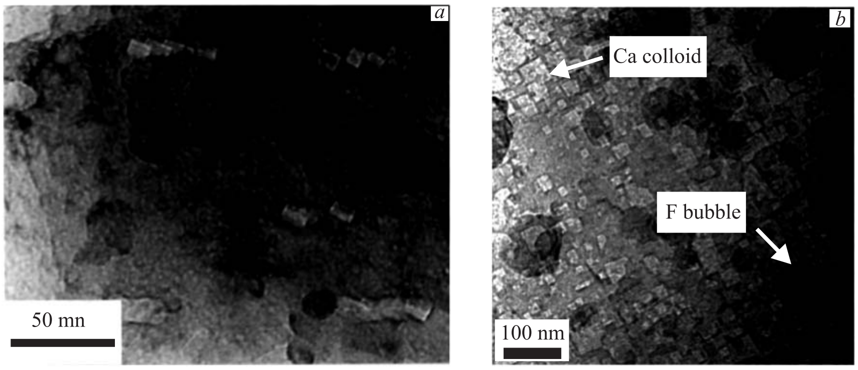

Fig. 47. *a*) TEM of 30 MeV C_{60} cluster ion tracks in CaF_2 — $\{001\}$ faceted cuboidal Ca colloids along the tracks [216]. *b*) Arrays of large faceted Ca colloids in CaF_2 and pockets of F bubbles following *in-situ* 300 keV electron irradiation of CaF_2

generates the primary basic defects in the form of nonionizing excitation of the F anion, i.e., electron-hole pair, and due to the Coulomb attraction, the formation of an exciton is localized and accommodated by means of a lattice distortion to form a metastable self-trapped exciton (STE). The STEs in turn decay into a more stable defects in the anion sublattice of CaF_2, predominantly the mobile V_k centers active along the $\langle 001 \rangle$ directions of the simple cubic anion sublattice. The mobility of V_k centers eventually leads to both an agglomeration of anion voids, i.e., aggregation of F vacancies, and the associated separated aggregation of F interstitials; and the formation of these anion voids thereby leaves the cation sublattice unaltered.

This similarity (only the dimensions of track faceted segments are different) emphasizes the imposition of point defects motion and subsequent rearrangements in the wake of SHI or cluster ions in the aftermath of the compound spike [37].

In fact, the anion voids in CaF_2 lattice can be regarded as excess or an aggregation of Ca rich clusters or more generally as Ca inclusions embedded into the CaF_2 lattice [147]. The formation of the observed Ca colloids in TEM due to the *homogeneous* (nonlocalized) electron irradiation first proceeds from tiny random embryonic anion voids (appearing first as small spots of light contrast), with further electron irradiation these tiny anion voids coalesce and grow accompanied by F bubble formation. These anion voids (Ca inclusions) then arrange in cubic closest packed-structure, i.e., face center cubic structure (f. c. c.), characterized by a small misfit ($\sim 2\%$) wich represents the structure of the Ca sublattice in CaF_2 lattice. This lattice strain minimization through the preferred epitaxial growth at Ca/CaF_2 $\{001\}$ planar boundaries thus gives rise to the TEM observed metallic Ca cuboidal colloids arrays as shown in Fig. 47, *b* and *a* as a string of Ca colloids, as the V_k center eventually carries the energy/momentum away due to huge *localized* ionization energy loss in the wake of the bombarding 30 MeV C_{60} cluster ion leading to the above-discussed scenario and to formation of Ca colloids along the track. Also, attention is drawn to the bubbles of F near the surfaces at the track ends — the dark contrast features in both Fig. 47, *a* and *b* [144–147]. Thus in the case of cluster ion irradiated CaF_2, the array of metallic Ca colloids constituting the observed tracks, comprise the distinct elemental units free of F anions, which define the track morphology and intermittency (i.e., CaF_2 does not amorphize even at the extreme value of electronic energy deposition by 30 MeV C_{60} cluster ions of ~ 47 keV/nm) [163, 164].

Now, as we can see, in limited length sections (by definition) the latent tracks in TEM can frequently be understood if observations of etched tracks in the same materials are made by Transmission Optical Microscopy (TOM). The two techniques, whilst often limited if used alone, are symbiotic if results from each diagnostic technique are compared and contrasted. In Fig. 48, we show natural fission fragments confined tracks (the whole track is confined inside the bulk of material) in a typical chemically etched sample of monazite sample. However, there are some fundamental questions raised. Why are etched ion tracks in monazite continuous, whilst latent tracks by TEM are not? One remarking note is that the former are tracks in the bulk; the latter are tracks in thin crystals or thin foils.

Measurements of bulk *confined* fission track lengths in the TOM — such as those shown in Fig. 48 — were taken both at room and successively increasing annealing temperatures. The results are summarized in Table 3.

Both the properties of the target (monazite) and the projectiles (fission fragments; light and heavy fragments) are shown in the following Table 4.

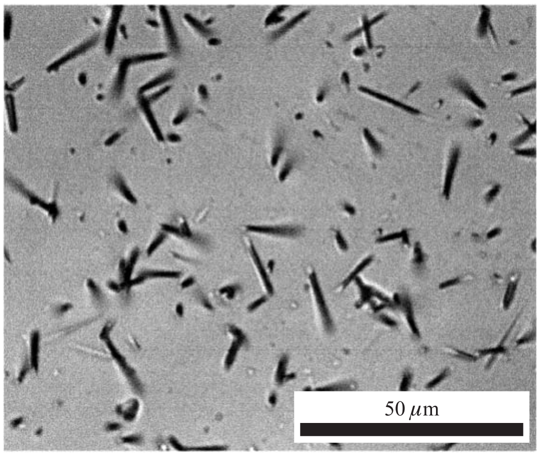

Fig. 48. TOM of chemically etched confined fission fragment tracks in monazite

Table 3. **Data from TOM observations of fission fragments track lengths and densities upon annealing monazite**

Annealing conditions	Mean length of fossil confined tracks, μm	Fossil track density, 10^6 cm^{-2}
Un-annealed	10.0 ± 0.3	5.03 ± 0.14
1 h at 150 °C	9.7 ± 0.2	4.50 ± 0.09
1 h at 175 °C	9.4 ± 0.2	5.31 ± 0.13
1 h at 200 °C	66 ± 0.6	4.14 ± 0.07
1 h at 225 °C	3.3 ± 0.1	2.65 ± 0.09

Table 4. **Properties of monazite (target) and fission fragments (projectiles)**

Monazite CePO$_4$ (density = 5.5 g/cm^3)	Heavy fission fragment	Light fission fragment
Z	53	39
A	138	95
E_0, MeV	69.63	1001
Range, μm	8.0 ± 0.6	9.9 ± 0.5
Track length, μm	17.9 ± 0.9	—

It is important to note that the mean length of fission fragments confined tracks in monazite is $\sim$ (10.0 ± 0.3) μm, whilst the frequently used computer simulation of TRIM and, more recently SRIM [130, 165], predicts a figure of (17.9 ± 0.9) μm (i.e., the total range, which is the sum of both the ranges for heavy and light fission fragments). This profound difference in length by a factor of $\sim$ 0.6 is attributed to projectile assisted prompt anneal process (PAPA) [37] *during* track registration — and as far as we know — is the first direct experimental evidence for that process taking place in a «compound spike». For example, in SHI irradiated Si, the recovery process is profound (i.e., 100%), recovery is complete and not partial — fission fragment tracks were *never* seen in that material, despite the odd report to the contrary in the literature [46]. In the present context we therefore find that partial recovery of track lengths can best be understood in terms of an activated participation of point defects *during* track registration. Subsequent track shrinkage during isochronal anneals at higher temperature merely bears out, of course, that a simple Arrhenius expression for the steady-state thermal activation of characteristic point defects is also responsible for shrinkage and eventual track disappearance, assuming that it is unnecessary to account for the effects of normal ambient laboratory pressure in the overall equation of state.

It is very important to note that proper TOM measurements of etched continuous *confined* track lengths clearly do not suffer from any counter argument based on surfaces and their properties!

On the other hand, it would seem that we *must* indeed look to surfaces in order to understand the track structure and annealing behavior in thin crystals, and this *must* lead us to atomistic point defects for an explanation in physics. It cannot be too frequently emphasized that the TRIM computer code, in which reasonable approximations have served us so well in the world of ion irradiation, can no longer be relied upon. Neither TRIM nor all its recent variants (e.g., SRIM) account for crystallinity, defects, and a free surface. For example, TRIM cannot in any fruitful way be applied to the stopping of cluster projectile ions such as C_{60}. Important «*wake*» stopping physics, *vicinage* effects, and plasma generation are among the many new physical phenomena not accounted or considered [37].

The failure of TRIM and prediction what is in fact observed is too readily ignored because of the implicit attraction that separation of the old ionizing and ballistic energy losses seems to be so readily included. Furthermore, the experimental fact that latent tracks due to such *brutally* ionizing projectiles such as C_{60} ions in CaF_2 are also intermittent (Fig. 47, *a*) is a cogent warning in itself. It is well known that the real (not TRIM predicted) ranges of energetic ions in crystalline solids certainly depend upon collisional opportunities for channeling and blocking — open and closed pathways in the crystalline lattice — and on classical critical angles (the corresponding maximum incident angles for which the incident particle can be steered by the atomic rows inside the crystal, as there is a minimum distance of the approach of the incident particle to the atomic rows when it starts to sense the string potential of atoms constituting the approached rows) which can have a strong effect on electronic and nuclear energy loss processes.

For completeness we show in Fig. 49 the angular distribution for natural fission fragment tracks in monazite where the origin is taken to lie in the basal plane of the crystal. Very little anisotropy can be detected.

We have made it clear therefore, that attention now not only should be taken away from simple macroscopic models of the past, such as the Thermal Spike, and from the range of the so-called delta-electrons, but that defects operating on atomistic levels and the presence of surfaces and/or interfaces are the determining factors not only for shaping the morphology of latent tracks, but also necessary in describing why tracks are not even formed in certain material targets. By implication, the compound spike [37] and its dependence on moving target-specific defects must be invoked and enlarged upon, and it is no coincidence that it is in this kind of atomistic model where we will find adequate explanations in physics of most of the experimental observations in the world of ion track physics.

The action of surfaces and interfaces as sinks and sources for point defects is well known [73, 74]. For a single crystal–vacuum interface — the «strength» of such a semi-infinite surface for point defects varies as (d^{-1}), where d is the depth, or distance from the surface [72, 73]. For thin crystals used in TEM there are two such surfaces to be reckoned with, so that the sink «strength» is proportional

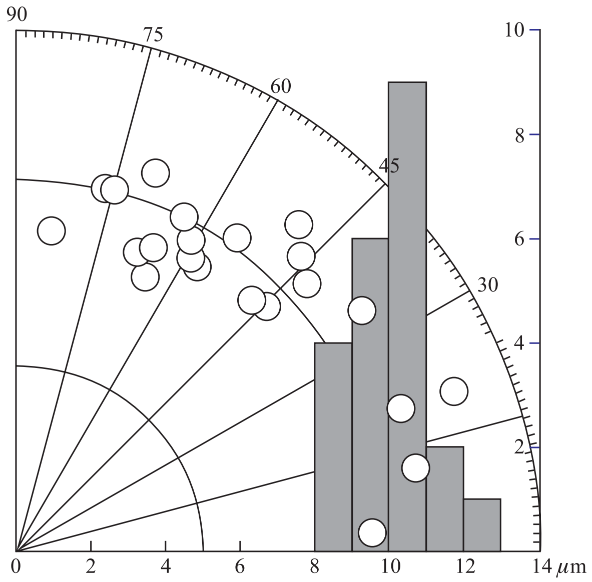

Fig. 49. Measured lengths and angular distribution of etched fission fragments tracks in monazite, the mean length of tracks is 10 μm

to (t^{-2}), where t is the thin foil thickness. It follows that many TEM images of latent tracks registered in thin crystals are strongly susceptible to this huge defect loss during passage of the incident ionizing ion (going in, passing through, and coming out of the crystal). Furthermore, the relevant thicknesses (t_e) for point defects escape are *most often* of a size $\leqslant t_e = (4{-}5)\xi_g$, where ξ_g is the relevant «TEM imaging» extinction distance* for the reflection vector $\mathbf{g}$ in the two-beam approximation. It is for these distances that inelastic scattering into vectors $\mathbf{s}$ becomes paramount. This in turn means that in many cases caution has to be exercised when interpreting ion tracks in thin crystalline targets relative to the bulk. And it has become the custom to assume that energetic ions in solids will leave a continuous latent track which, below a certain critical energy towards end of range, becomes intermittent.

---

[*] ξ_g is a material specific oscillation in the amplitude of diffracted electron beam (in exact Bragg condition) along the thickness of the material, i.e., the electron intensity transfers one time back and forth between the forward (transmitted) and diffracted beam over a distance ξ_g, this periodicity depends on electron energy and the structure factor for the actively diffracting planes and atoms, typical values are $\sim$ few tens of nm for most materials and usual operating reflections and TEM voltages — for example, $\xi_{001} = 47$ nm for InP for 175 keV operating electrons [166].

This is a not unreasonable attractive model, though we would emphatically argue and repeat that reports assuming that the resulting segments are dislocation loops [50, 51] should not do so without carrying out proper *in situ* TEM tilting experiment using known operating Bragg reflecting vectors **g** and determining the real Burgers vector **b**. Certainly, such tracks can be identified by their intermittency but the internal atomistic structure of individual segments, unless it is amorphous, is generally not known and can be experimentally challenging to know.

The intermittent ion tracks to which we have referred — in InP, apatite, and monazite — whilst clearly being due to loss of point defects (whatever the point defects are) to confining surfaces — have a totally different origin and are a function of the escape depth t_e for a particular target, and of the mobility and lifetimes of point defects intrinsic to the specific physical condensed matter characteristics of each single-crystal target! That this must be so, is clear from Fig. 47, a, where the deposited energy density of 30 MeV C_{60} cluster ions into the target (CaF_2) is high (47 keV/nm) [162, 163], and similar effects using SHI at energies well above the Bragg peak in electronic stopping power can be observed. This is revealed by our observations that for the case of monazite the 200 MeV Au ion tracks are intermittent whilst etched fission fragment tracks in bulk monazite observed by TOM are continuous. We conclude that, in general, latent «near surface tracks» or subsurface tracks — in part because of their underlying intermittency — may not only be difficult but may be impossible to chemically etch. Consider, for example, the well-known difficulty of revealing continuous «developed» tracks in fluorite (CaF_2). Evidently, there is a fast hot

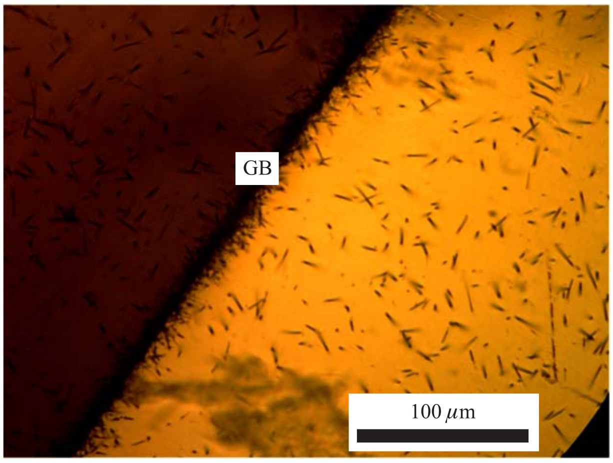

Fig. 50. Fission fragment tracks near a grain boundary (GB) and in the bulk (confined tracks) in monazite

H_2SO_4 etching rate of the first (surface) calcium colloid ER_{Ca}, followed by a much slower etching rate ER_{CaF_2} to be overcome, before the next intermittent segment can be etched at the much swifter etching rate again [167]. Chemical etching of ion tracks in CaF_2 is therefore extremely difficult — it is only possible when many chemically sensitive impurities are present. On the other hand, for materials in which long, well-developed tracks can be seen in the TOM — including apatite and monazite — it is evident that *surface intersecting* tracks are remarkably resistant to prior annealing, whilst confined tracks — inside the bulk away from surface(s) and interface(s) — are shortened by the return and annihilation of intrinsic point defects. It is a normal and proper procedure in geophysical applications to completely ignore tracks intersecting either free surfaces or internal interfaces such as grain boundaries. However, tracks originating at a grain boundary or intersecting the grain boundary region (which might be due to prior aggregation of the natural isotopes of U) can survive annealing, and be developed chemically and are essentially «pinned» there. An example of a density excess of etched fission tracks in monazite at a grain boundary over those in the bulk, is shown in Fig. 50.

4.3. Track Formation in Apatite and Monazite. At first glance, the appearance of polymorphic segments on 200 MeV Au^+ ion tracks in both apatite and monazite seems to be at odds, for example, with the conclusions made for the origin of such features in CaF_2. Certainly, we do not expect V_k centers in either of these minerals. This has been independently confirmed by Stoneham and Itoh [16]. On the other hand, all crystals have angular dependent directional properties, and moving point defects arising from the essential preferential excitation of anion sublattices (not necessarily full ionization) in ionic crystalline matter can certainly be constrained to certain directions by low energy or diffusive collisional mechanisms other than those associated with dynamic *crowdions*.

Such possibilities have emerged in recent calculations (using density-functional theory with the local-density approximation (DFT-LDA)), of the electronic and crystallographic structures of apatites [168], because of the fact that the general mineral class of apatites is notorious for its close affinity for appearing in either hexagonal or monoclinic crystalline forms, depending on the state of stoiochiometry. Natural fluoroapatite, however, is hexagonal. In the atomic structure of fluoroapatite Ca bond to F anions forming a triangular group, these groups arrange into columns that are parallel to the c axis [169, 170]. Figure 51, *a* is a general view of fluoroapatite crystal and a top view of four unit cells along the c axis showing the very important Ca cation triangles fundamental to the structure, where the F anion sits centrally in the plane of the Ca triangles, the O of phosphate groups are also shown. While Fig. 51, *b* shows a close-up top view of the region around the c axis from which it is clear that the two Ca triangles are rotated by 60° around the F anion which lies in the plane of the Ca triangles, these triangles lie at $z = 1/4$ and $z = 3/4$ along the c axis.

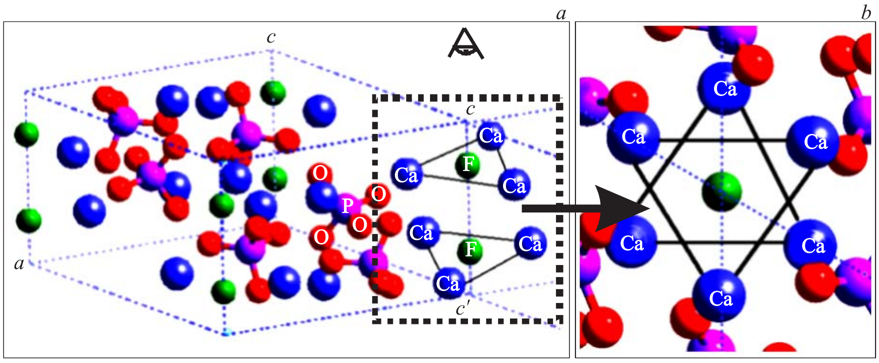

Fig. 51. *a*) A general view of apatite structure (fluoroapatite) including Ca triangles; *b*) a closer top view along the c axis of four unit cells showing two Ca triangles and the F anions in-between

Accordingly, we only have preferential motion along the c axis, and the formation of three-dimensional colloids, which are clearly observed in tracks (see Figs. 42–44 and Fig. 45 for 200 MeV Au ion and 30 MeV C_{60} cluster ion irradiation, respectively, in fluoroapatite). On the other hand, from the microscopic point of view, we have alluded to the fact that Ca colloids forming a cubic superlattice in CaF_2 are not only directly related to $\langle 001 \rangle$ directed anion motion of V_k, but that we must also have in mind a final phase of superlattice formation in which we essentially have simultaneous microscopic internal epitaxy of Ca colloids taking place on the Ca sublattice in CaF_2 itself rendering the cuboidal Ca colloids (the track segments) observable in TEM.

In apatites in general, the anion (F, Cl or OH) arrangement is conveniently characterized by the distance z between the anions and the Ca triangles which lie perpendicular to the c axis. In the case of fluoroapatite $\mathrm{Ca_5(PO_4)_3F}$, for present purposes we simply note that collisional and/or diffusional anion motion along the c axis would be favored, as a sequence of interacting F-anion chain movements along the c axis provided that sufficient energy became available — possibly again from preferential absorption of energy from the projectile (200 MeV Au ion) and later conversion into momentum, followed by sequential displacement movements along the c axis. As it is most easy to disrupt the apatite structure parallel to c axis along the Ca–F triangle group columns (Fig. 52, *a*) rather than in direction in which large amount of energy is required to overcome the bonding forces perpendicular to the c axis where the $(\mathrm{PO_4})$ group and Ca in sixfold coordination with O are bonded to one another and to the Ca–F triangle groups by covalent sharing of O [171]. This would be equivalent to the dynamic crowdion motion of the Foreman mechanism (i.e., focused collisional and replacement sequence — by crowdion interstitials along close-packed atomic rows, whose one-dimensional

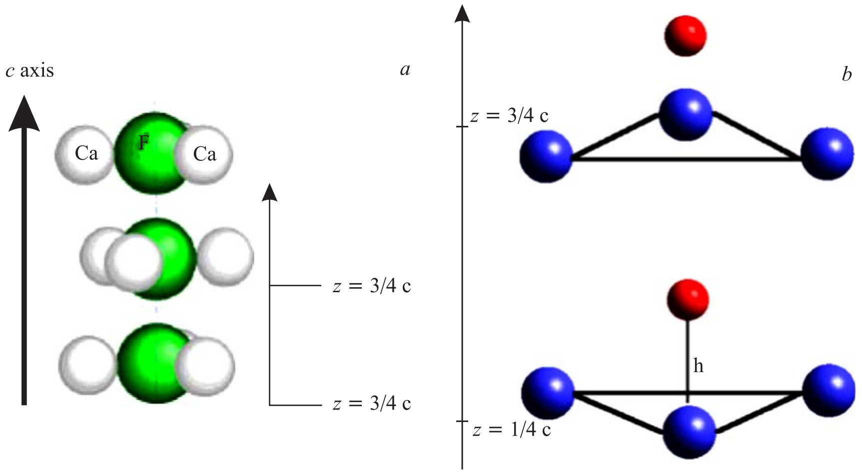

Fig. 52. *a*) Close up view of the region parallel to the c axis where the Ca–F triangle groups form a column along that axis in fluoroapatite; *b*) for $Ca_5(PO_4)_3Cl$ the anions are now Cl and lie outside the Ca triangles

diffusive and preferential migration properties may supply the driving force for voids to form a superlattice having the same structure and orientation as the irradiated lattice) which so clearly operates in the case of CaF_2 [143–147]. Similar anion movement can also occur in chloroapatite $Ca_5(PO_4)_3Cl$ where the Cl anion now is located at a distance $z = 1/2$ along the c axis outside the plan of the Ca triangles as shown in Fig. 52, *b*.

By no means these processes are mutually exclusive. Rather they are natural and self sustaining — in part different ways of looking at the same physical phenomenon — in achieving minimum interface energies *once more* according to the usual and well-understood continuum hydrodynamic phenomena under the general heading of catalytic capillarity [172] and each track is thus regarded as an intermittent heterogeneously nucleated row of faceted metallic Ca colloids along the trajectory.

Caldrin et al. [170] have also calculated the structure of an apatite which they refer to as c-empty, meaning that the c axis is empty of anions and now is a wide open channel of Ca triangles. The results are very interesting in our present context since removal of the F anions produces the *essential* chemical composition of monazite and its crystalline form. It should be kept in mind that the structure of apatites can be viewed as consisting of unconnected PO_4^{-3} tetrahedra with Ca^{2+} in the space between and a column of X^- (e.g., F, Cl and/or OH) anions along the c axis to balance the charge. Claderin et al. [168] also found the c-empty structure to be monoclinic and quite stable. However, all calculated apatites including the c-empty (e.g., monazite) in either hexagonal or monoclinic forms are remarkably stable with very similar binding energies. For completion we note that for c-empty there are two $\mathrm{Ca}_5(\mathrm{PO}_4)_3$ formula units per unit cell, and that the space groups of true fluoroapatite and the c-empty structure are $P6_3/m$ and P_3/m, respectively. The structure of monazite then looks (a close up top view along the c axis of four unit cells) as follows in Fig. 53, where the apexes of the now empty triangles aligned along the c axis are replaced now by cerium Ce cations rather than Ca cations.

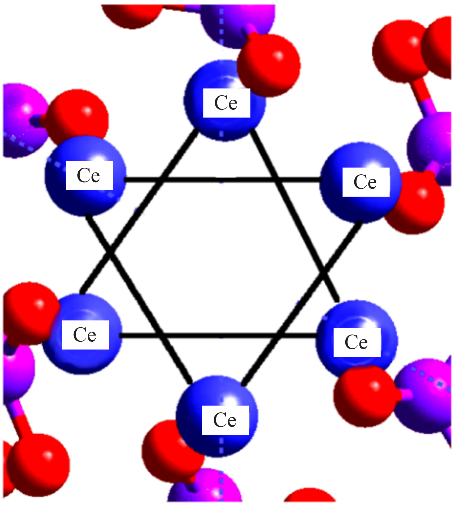

Fig. 53. Top view along the c axis in monazite, the Ca cations are now replaced by Ce cations and the Ce triangles are open now (empty c axis channel) — compare with Fig. 51, *b*

In the case of large electronic ionization damage, as with 200 MeV Au ion tracks, we may propose the following scenario involving point defects formation and recovery at the atomistic level; preferential absorption of ionization energy and the damage takes place, as it does in CaF_2, on the anion sublattice. For apatite this means that we must suppose that the (PO_4) groups are destroyed but reassemble extremely rapidly because of the large chemical affinity of P for O. The F anions can pass as sequential ballistic and then diffusional collisions along the c axis, being «*squeezed-in*» by the triangular Ca channels surrounding that axis. Note that this is similar to the V_k centre mechanism for CaF_2 but not identical to it, though still highly efficient in separating an interstitial from its vacancy. The F anion motion along the c axis, however, is proposed as the preliminary basis for the formation of polyhedral segments of ion tracks in apatite. Additionally we invoke epitaxial growth of Ca colloids associated with the initial general outward c axis motion of the F anions. This means that there is partial recovery or, in other words PAPA, reflected microscopically in the TEM observed segmental nature of track, as described earlier. Now, the application of this structural knowledge to ion tracks in monazite is more profound.

Firstly, we know from ion track etching in monazite that ion track lengths observed by TOM are much shorter than they should be (even if TRIM computations *were* 100% valid). Therefore, invoking the same model as for apatite, it would appear that once again the (PO_4) groups recover quickly after the initial disruption due to the passage of SHI. Now, on the other hand, we have a much more open lattice (empty c axis), so that c axis diffusion of any foreign anions (which can be expected in natural nonstoichiometric crystals) is rapid and unhindered by the presence of intrinsic anions along the c axis channel. Shaping into polymorphic Ce colloids in this case is once again a natural consequence of the overall annealing physics and subsequent epitaxial growth as similarly discussed for the well-known behavior of CaF_2. The much shorter track lengths seen in TOM are, as far as we are aware, the first definitive experimental demonstration of projectile assisted prompted anneal PAPA [37]. And, in this case, it would appear that shorter track lengths are *directly related* with the ionized breaking-up (*probably* similar to a Coulomb explosion spike) followed by very rapid recovery of the (PO_4) groups, after which the c-axis channels are opened again after the initial *chaos* due to the passage of SHI (or fission fragments). It is tempting to consider more generally the part played in ion track formation by (PO_4) groups recovery in all phosphate based minerals, and to relate recovery with the real experimentally observed lengths of unexpectedly short tracks! And also to consider what part might be played, if any, by similar processes taking place in the silica group based minerals of the quite separate and distinct class of silicates (i.e., minerals containing SiO_2 or SiO_4 groups) minerals generally — in muscovite mica, for example.

At the most basic level, neglecting track structure, we might anticipate an In rich «core», simply on the grounds of atomic mass, so that perhaps some simple point defect, such as the P vacancy and/or interstitial, might play a controlling role in both track registration and annealing.

What experiments on apatite and monazite have shown, however, is twofold. Firstly, it is always important to have in mind the primary *sublattice effect*, coupled with both damage and recovery during and aftermath of a compound spike — i.e., in a dynamic energy deposition process which is a composite of several processes far more complex than heretofore assumed. Secondly, for proper descriptions of what happens during energy deposition and recovery at the atomistic level it is necessary to consider the detailed part played by the intrinsic point defects involved in each target material. Therefore, it would appear from all of the TEM observations of tracks in apatite and monazite that intermittency is a *fundamental basic characteristic*, as in our observations in InP.

Probably, it can in this case be safely assumed that the same conclusion carries over to bulk InP and/or other track forming semiconductor materials and that, in the bulk, tracks may be continuous, since point defects are not lost to the surface(s) while if discontinuity arises deeper into the crystal it may be shaped by rather different mechanism such as the charge fluctuation (Komarov's model) discussed earlier; so it is *very important* to emphasize that the intermittent nature of tracks we have described, and the origin of it, is not a simple consequence of what must be expected when ions approach the end of their range, when the electronic stopping power $-(dE/dx)_{\text{inel}}$ falls to a level where continuous registration cannot be maintained by a low effective projectile ion charge $Z_{\rm eff}$. This is clear from the observations of C_{60} cluster ion tracks in both fluorite and apatite, where despite the massive *energy density* deposited, and the huge $Z_{\rm eff}$, the tracks are *still* intermittent. On the other hand, in very real sense it is a basic *lack of point defects availability* which operates in each case. In the first instance, there is loss of defects to the surface. In the second case, the primary screened Coulomb electronic interaction is naturally weak, the defects produced by these means are spatially few in number and the nuclear stopping power $-(dE/dx)_n$ takes over in the final act of ending the energy deposition process in a last burst of kinetic energy removal in which the ion ends its projectile life as a neutral impurity atom inside the lattice.

4.4. Summary. TEM observations of 200 MeV Au ion tracks in both apatite and monazite showed that tracks are segmented with a tendency for polyhedral segments. Drawing similarities between the observed SHI tracks in these materials with observed cluster ion tracks in CaF_2 shows that more comprehensive understanding exists on defect formation and dynamics in that material. A scenario of track formation in both apatite and monazite was proposed based on the crystal structures of apatite and monazite, which emphasizes the importance of point defects and atomistic nature of track formation.

Appendix I

ANALOGUES TO HYDRODYNAMICS IN SEVERAL SOLID STATE PHENOMENA*

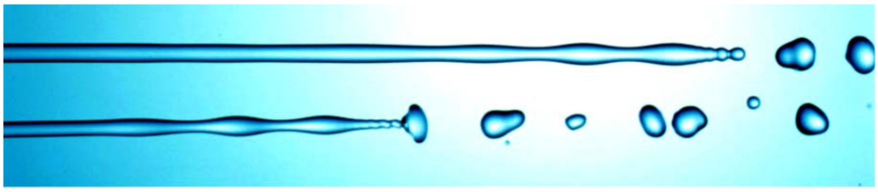

Fig. A.1. Fragmentation due to capillary-driven instability and break-up into droplets of a water jet as was first described theoretically by Lord Rayleigh in 1887. He introduced his seminal work with the following: With respect to instability of capillary force, the principle problem is the determination, as far as possible, of the mode of disintegration of an infinite cylinder, and in particular, of the number of masses into which given length of cylinder may be expected to distribute itself [75]

---

*The illustrative pictures merely draw attention to the beauty and universality of hydrodynamic phenomena such as the Rayleigh instability. For an excellent and clear review of Rayleigh instability, refer to; *Eggers J.* Nonlinear Dynamics and Break-up of Free Surface Flow // Rev. Mod. Phys. 1997. V. 69. P. 865–929. And for a comprehensive review of the theory refer to; *Kull H. J.* Theory of the Rayleigh Instability // Phys. Rep. 1991. V. 206. P. 197–325.

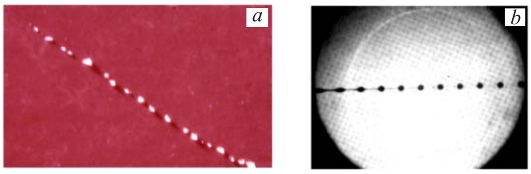

Fig. A.2. *a*) Break-up of a water streamlet upon impact on ceramic tile. *b*) Stroboscopic image of a fast speed ink jet (speed = 9 m/s) ejected from a fine nozzle (diameter = 63 μm) breaking up into droplets of $\sim \lambda/d = 5.3$ (where λ is the droplet diameter and d is the distance between droplets)

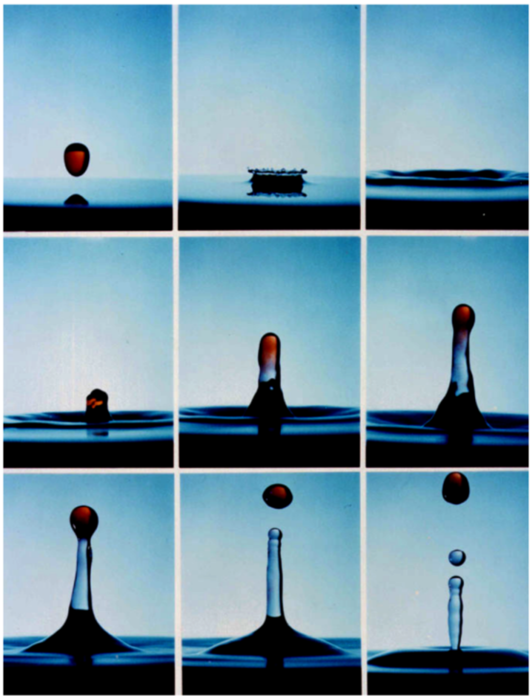

Fig. A.3. This composite of successive pictures (spark photography, exposure time = 5 μs) shows a fluid drop landing on a pool of the same liquid and is the *classical mechanical hydrodynamic analogue* of a swift ion incident upon a solid target. Impact is in the second frame; material is pushed aside and a Rayleigh crown is produced. In the ion-solid interaction case the target first behaves as a true fluid, then as a viscous medium (obeying the Navier–Stokes equation), and finally solidifies as a trough. The emerging «plume» corresponds to the simple process of «sputtering». This hydrodynamic analogue is invoked to explain crater-rim formation in some solids irradiated by cluster ions as shown in the following Fig. A.4. (Courtesy of Prof. J. Field, Cambridge University, UK) [14]

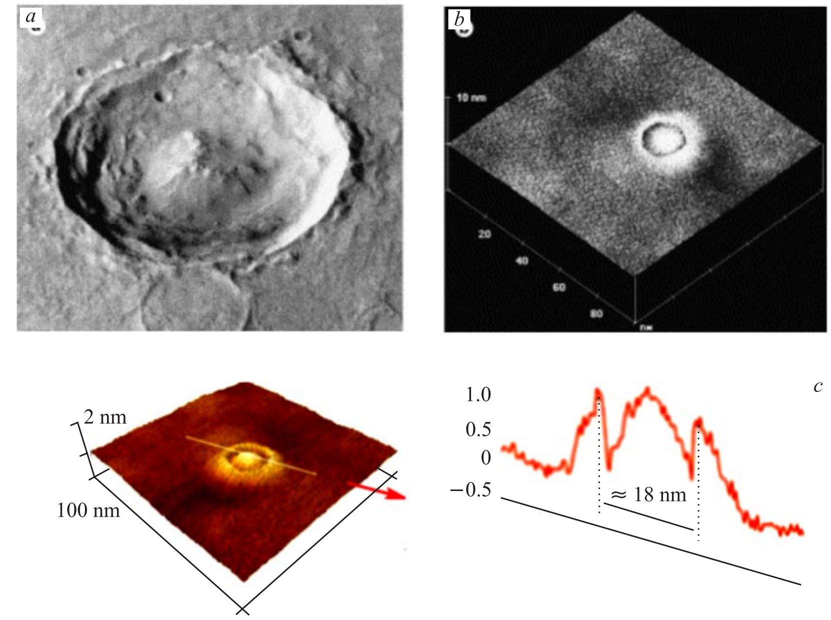

Fig. A.4. Examples of processes invoking complex hydrodynamics of collision like that depicted in the previous figure. The collision is followed by fluid melt and quench. *a*) Macroscopic analogue to the impact of high-velocity collision; in this case the Yuty crater is formed by meteorite impact on Martian surface with diameter of ∼ 18 km as imagined by Viking 1 orbiter. *b*) Nanoscopic analogue presented in the AFM image of a surface track in the form of complex nanoscopic crater (a central bump surrounded by an elevated rim) in (111) Si surface resulting from a single 18 keV/ion Ar_{12} cluster ion impact at normal incidence. *c*) AFM sectional analysis of the rim-to-rim diameter of the crater ∼ 18 nm and rim elevation of ∼ 0.8 nm [173]

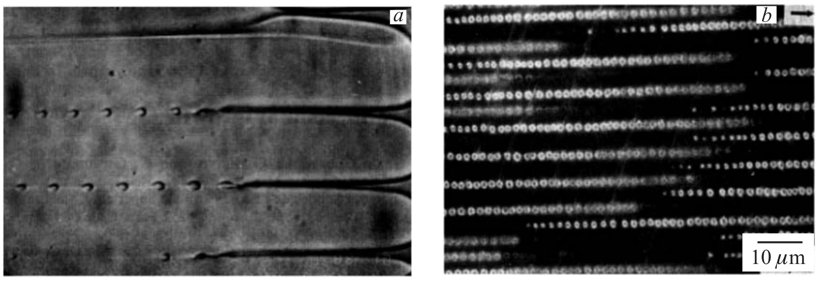

Fig. A.5. *a*) Break-up of liquid grooves during carbon tetra-bromide CBr_4 [173] solidification. *b*) Break-up of aligned rods into spheres during cooperative monotectic growth of zinc-bismuth (Zn–Bi) alloy [174]

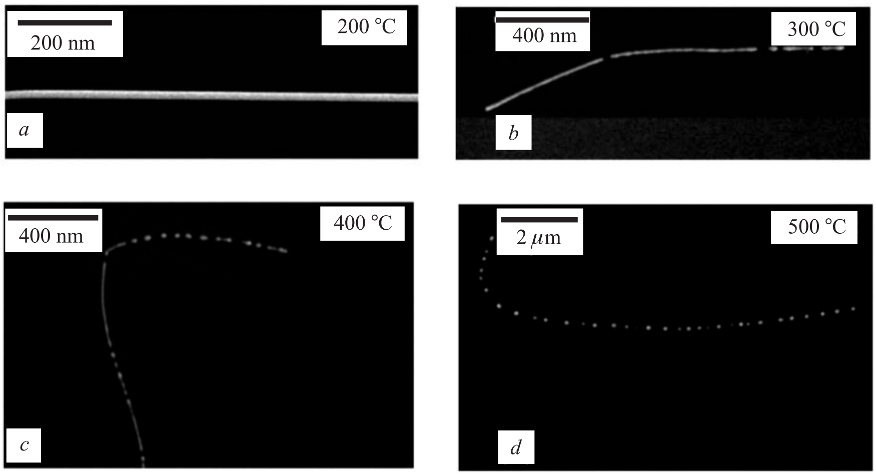

Fig. A.6. High resolution SEM of 25 nm Au wire annealing at different temperatures for 30 min. Wire preserves its shape after annealing at 200 °C (*a*), at 300 °C perturbations start to appear (*b*), at 400 °C the wire fragments into smaller sections (*c*), and finally at 500 °C it transforms to a string of nanoshperes (*d*) [174]

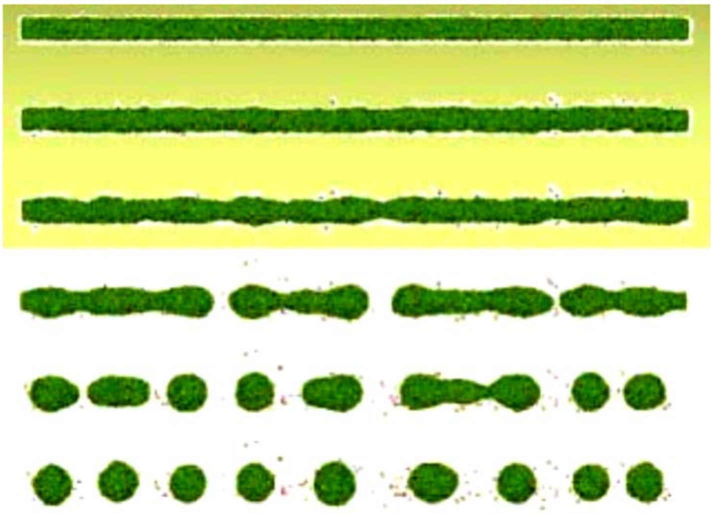

Fig. A.7. MD simulation of Rayleigh-driven instability in ∼ 8 nm Ge nanowire buried in SiO_2 substrate synthesized by ion implantation, the wire breaks-up into nanospheres following thermal treatment [175, 176]

REFERENCES

1. *Alferov Zh. I.* Twice Heterostructures: Conception and Applications in Physics, Electronics and Technology // Usp. Fiz. Nauk. 2002. V. 172, No. 9. P. 1068–1086.
2. *Ledentsov N. N. et al.* Getter-Structures with Quantum Points: Creation, Properties, Laser // Rev. Phys. and Techn. of Semiconductors. 1998. V. 32, No. 4. P. 385–410.
3. *Michuskin V. M., Sysoev S. E., Godeev Yu. S.* Nanostructure Creation by Ion Bombardment of Semiconductors and High-Temperature Superconductors // News of Rus. Acad. of Sci. Ser. Phys. 2002. V. 66, No. 4. P. 588–592.
4. *Bouneau S. et al.* Very Large Gold and Silver Sputtering Yields Induced by keV to MeV Au$_n$ Gold Clusters ($n = 1-13$) // Phys. Rev. B. 2002. V. 65. P. 144106-1–144106-8.
5. *Amirhanov I. V. et al.* Sputtering of Solids by Heavy Ions and Temperature Effects in Electronic and Lattice Subsystems // Part. Nucl. 2006. V. 37, No. 6. P. 837–866.
6. *Komarov F. F.* Defect and Track Formation in Solids Irradiated by Superhigh-Energy Ions. // Usp. Fiz. Nauk. 2003. V. 46, No. 12. P. 1253–1282.
7. *Wang Z. G. et al.* The Sensitivity of Metals under Swift Heavy-Ion Irradiation: A Transient Thermal Process // J. Phys.: Condens. Matter. 1994. V. 6. P. 6733–6750.
8. *Dufour Ch. et al.* // A High-Resistivity Phase Induced by Swift Heavy-Ion Irradiation of Bi: A Probe for Thermal Spike Damage // J. Phys.: Condens. Matter. 1993. V. 5. P. 4573–4584.
9. *Trinkaus H.* Local Stress Relaxation in Thermal Spikes as Possible Cause for Creep and Macroscopic Stress Relaxation of Amorphous Solids under Irradiation // J. Nucl. Mater. 1995. V. 223. P. 196–201.
10. *Davydov A. A., Kalinichenko A. I.* About Mechanical Effects around Thermal Peaks and Fission Fragment Tracks // At. Ener. 1982. V. 53, No. 3. P. 186–187.
11. *Didyk A. Yu. et al.* Damage Distribution in GaAs Single Crystal Irradiated with ^{84}Kr (394 MeV), ^{209}Bi (710 MeV), and ^{238}U (1300 MeV) Swift Ions // Nucleonika. 2008. V. 53, No. 2. P. 77–82.
12. *Khalil A. S., Didyk A. Yu.* RBS and TEM Studies of Indium Phosphide Irradiated with 100 keV Au Ions // Part. Nucl., Lett. 2009. V. 6, No. 6(155). P. 820–830.
13. *Khalil A. S., Didyk A. Yu.* Influence of TEM Low Energy Electron Irradiation on InP Damage Structure, Irradiated Previously by 100 keV Au Ions // Ibid. V. 6, No. 7(156) (in press).
14. *Fink D., Chadderton L. T.* Ion-Solid Interactions: Current Status, New Perspectives // Radiation Effects. 2005. V. 160, Nos. 3–4. P. 67–83.
15. *Kaganov M. I., Lifshitz I. M., Tanatarov L. V.* Relaxation between Electrons and the Crystalline Lattice // Theor. Exp. Phys. 1957. V. 4. P. 1973–1978.
16. *Itoh N., Stoneham M. A.* Materials Modification by Electronic Excitation. London: Cambridge Univ. Press, 2001.

17. *Seitz F., Koehler J. S.* Displacement of Atoms During Irradiation // Solid State Phys. 1956. V. 2. P. 307–312.

18. *Lifshitz I. M.* About Thermal Spikes in Media, Underjoined with Nuclear Irradiation // Dokl. of Acad. Sci. of USSR. 1956. V. 109, No. 6. P. 1109–1111 (in Russian).

19. *Lifshitz I. M., Kaganov M. I., Tanatarov L. V.* The Theory of Relaxation Changes in Metals // At. Ener. 1959. V. 6. P. 391–402 (in Russian).

20. *Kaganov M. I., Lifshitz I. M., Tanatarov L. V.* Relaxation between Electrons and Lattice // J. Exp. Theor. Phys. 1956. V. 31, No. 2(8). P. 232–237 (in Russian).

21. *Gegusin Ya. E., Kaganov M. I., Lifshitz I. M.* The Free Path Electron Length on the Creation of Trajectory Track of Charged Particle in Metal // Fisika Tverd. Tela. 1978. V. 15, No. 8. P. 2425–2428 (in Russian).

22. *Fleischer R. L. et al.* Criterion for Registration in Dielectric Track Detector // Phys. Rev. 1967. V. 156. P. 353–355.

23. *Fleischer R. L., Price P. B., Walker R. M.* Nuclear Tracks in Solids. Berkeley: Univ. of California Press, 1975.

24. *Didyk A. Yu., Varichenko V. S.* Track Structure in Dielectric and Semiconductor Single Crystals Irradiated by Heavy Ions with High Level Inelastic Energy Losses // Nucl. Track and Rad. Meas. 1995. V. 25, Nos. 1–4. P. 119–124.

25. Fundamentals of Ion-Irradiated Polymers / Ed. by Fink D. Springer Series in Materials Science. Berlin: Springer-Verlag, 2004.

26. *Trinkaus H., Ryazanov A. I.* Viscoelastic Model for the Plastic Flow of Amorphous Solids under Energetic Ion Bombardment // Phys. Rev. B. 1995. V. 74, No. 25. P. 5072–5075.

27. *Stampfli P.* Electronic Excitation and Structural Stability of Solids // Nucl. Instr. Meth. B. 1996. V. 107, Nos. 1–4. P. 138–145.

28. *Fleischer R. L.* Tracks to Innovation-Interplay between Science and Technology // Rad. Meas. 1997. V. 28, Nos. 1–6. P. 763–772.

29. *Phillips J. C.* Bonds and Bands in Semiconductors. N. Y.: Acad. Press, 1973.

30. *Komarov F. F.* Defect and Track Formation in Solids Irradiated by Superhigh-Energy Ions // Usp. Fiz. Nauk. 2003. V. 46, No. 12. P. 1253–1282.

31. *Wesch W., Komarov A., Wendler E.* Effect of High Electronic Energy Deposition in Semiconductors // Nucl. Instr. Meth. B. 2004. V. 225, Nos. 1–2. P. 111–128.

32. *Miotello A., Kelly R.* Revisiting the Thermal-Spike Concept in Ion-Surface Interaction // Nucl. Instr. Meth. B. 1997. V. 122, No. 3. P. 458–469.

33. *Houpert C. et al.* Transition from Localized Defects to Continuous Latent Tracks in Magnetic Insulators by High-Energy Heavy Ions: A HREM Investigation // Nucl. Instr. Meth. B. 1989. V. 39, Nos. 1–4. P. 720–723.

34. *Szenes G. et al.* Tracks Induced by Swift Heavy-Ions in Semiconductors // Phys. Rev. B. 2002. V. 65. P. 045206.

35. *Komarov F. F.* Effects of Latent Tracks Formed by High-Energy Ion Implantation in Crystals // Langmuir. 1996. V. 12, No. 1. P. 199–206.

36. *Studer F. et al.* High Resolution Electron Microscopy of Tracks in Solids // Nucl. Instr. Meth. B. 1997. V. 122, No. 3. P. 449–457.

37. *Chadderton L. T.* Nuclear Tracks in Solids: Registration Physics and the Compound Spike // Rad. Meas. 2003. V. 36, Nos. 1–6. P. 13–34.

38. *Rosenbaum H. S.* Microstructures of Irradiated Materials. N. Y.: Acad. Press, 1975.

39. *Gaiduk P. I. et al.* Effect of Alloy Composition on Track Formation in Relaxed $\mathrm{Si}_{1-x}\mathrm{Ge}_x$ // Physica B: Condens. Matter. 2003. V. 340/342. P. 808–812.

40. *Levalois M., Bogdanski P., Toulemonde M.* Induced Damage by High-Energy Heavy-Ion Irradiation at the GANIL Accelerator in Semiconductor Materials // Nucl. Instr. Meth. B. 1992. V. 63, Nos. 1–2. P. 14–20.

41. *Dunlop A., Jaskierowicz G., Della-Negra S.* Latent Track Formation in Silicon Irradiated by 30 MeV Fullerenes // Nucl. Instr. Meth. B. 1998. V. 146, Nos. 1–4. P. 302–308.

42. *Canut B. et al.* Latent Tracks Formation in Silicon Single Crystals Irradiated with Fullerenes in the Electronic Regime // Ibid. P. 296–301.

43. *Colder A. et al.* Latent Track Formation in Germanium Irradiated with 20, 30, and 40 MeV Fullerenes in the Electronic Regime // Nucl. Instr. Meth. B. 2001. V. 174, No. 4. P. 491–498.

44. *Colder A. et al.* Latent Track Formation in GaAs Irradiated with 20, 30, and 40 MeV Fullerenes // J. Appl. Phys. 2002. V. 91, No. 9. P. 5853–5857.

45. *Dammak H. et al.* Tracks in Metals by MeV Fullerenes // Phys. Rev. Lett. 1995. V. 74. P. 1135–1138.

46. *Furuno S. et al.* Tracks of High-Energy Heavy-Ions in Solids // Nucl. Instr. Meth. B. 1996. V. 107, Nos. 1–4. P. 223–226.

47. *Kucheyev S. O. et al.* Lattice Damage Produced in GaN by Swift Heavy Ions // J. Appl. Phys. 2004. V. 95, No. 10. P. 5360–5365.

48. *Scholz R., Vetter J., Hopfe S.* Observation of Latent Heavy-Ion Tracks in GeS by Transmission Electron Microscopy // Rad. Effects & Defects in Solids. 1991. V. 126. P. 275–278.

49. *Vetter J.* TEM Investigations of Heavy-Ion Latent Tracks // Rad. Meas. 1995. V. 25, Nos. 1–4. P. 33–38.

50. *Gaiduk P. I. et al.* Discontinuous Tracks in Relaxed $\mathrm{Si}_{0.5}\mathrm{Ge}_{0.5}$ Alloy Layers: A Velocity Effect // Appl. Phys. Lett. 2003. V. 83, No. 9. P. 1746–1748.

51. *Wesch W. et al.* 593 MeV Au Irradiation of InP, GaP, GaAs, and AlAs // Nucl. Instr. Meth. B. 2006. V. 242, Nos. 1–2. P. 363–366.

52. *Gaiduk P. I., Komarov F. F., Wesch W.* Damage Evolution in Crystalline InP During Irradiation with Swift Xe Ions // Nucl. Instr. Meth. B. 2000. V. 164/165. P. 377–383.

53. *Herre O. et al.* Formation of Discontinue Tracks in Single Crystalline InP by 250 MeV Xe Ion Irradiation // Phys. Rev. B. 1998. V. 58, No. 8. P. 4832–4837.

54. *Wesch W. et al.* Damage Formation in InP due to High Electronic Excitation by Swift Heavy Ions // Nucl. Instr. Meth. B. 1998. V. 146, Nos. 1–4. P. 341–349.

55. *Komarov F., Gaiduk P., Kamarou A.* Damage Evolution and Track Formation in Crystalline InP and GaAs during Swift Kr and Xe Ion Irradiation // Vacuum. 2001. V. 63, No. 4. P. 657–663.

56. *Komarov F. F. et al.* Track Formation in Germanium Crystals Irradiated with Superhigh-Energy Ions // Vacuum. 2003. V. 70, Nos. 2–3. P. 75–79.

57. *Komarov F. F., Komarov A. F., Mironov A. M.* Influence of Initial Charge and Charge State Fluctuations on High-Energy Ion Ranges and Track Formation // Nucl. Instr. Meth. B. 1999. V. 148, Nos. 1–4. P. 159–163.

58. *Belyi V. A., Komarov F. F.* Model of Noncontinuous Track Formation in InP under Swift Ion Implantation // Nukleonika. 1999. V. 44, No. 2. P. 375–380.

59. *Komarov F. F., Belyi V. A.* Fluctuation Mechanism of Formation of Discontinuous Tracks by Fast Ions in Solids // J. Exp. Theor. Phys. 2002. V. 95, No. 2. P. 316–324.

60. *Gaiduk P. et al.* Wurtzite InP Phase Formation during Swift Xe-Ion Irradiation // Nukleonika. 1999. V. 44, No. 2. P. 189–193.

61. *Gaiduk P. et al.* Wurtzite InP Formation during Swift Xe-Ion Irradiation // Phys. Rev. B. 2000. V. 61, No. 23. P. 15785–15788.

62. *Zhu Y. et al.* Structures and Effects of Radiation Damage in Cuprate Superconductors Irradiated with Several-Hundred-MeV Heavy Ions // Phys. Rev. B. 1993. V. 48, No. 9. P. 6436–6450.

63. *Riedel C., Spohr R.* Statistical Properties of Etched Nuclear Tracks. I: Analytical Theory and Computer Simulation // Rad. Effects. 1979. V. 42. P. 69–75.

64. *Studer F., Toulemonde M.* Irradiation Damage in Magnetic Insulators // Nucl. Instr. Meth. B. 1992. V. 65, Nos. 1–4. P. 560–567.

65. *Costantini J. M. et al.* High-Energy Heavy-Ion Irradiation Damage in Yttrium Iron Garnet // Ibid. P. 568–575.

66. *Meftah A. et al.* Swift Heavy Ions in Magnetic Insulators: A Damage-Cross-Section Velocity Effect // Phys. Rev. B. 1993. V. 48, No. 2. P. 920–926.

67. *Belyi V. A, Komarov F. F.* Fluctuation Mechanisms for Formation of Discontinuous Tracks by Fast Ions in Crystals // Techn. Phys. 1998. V. 43, No. 9. P. 1048–1050.

68. *Betz H. D.* Charge States and Charge-Changing Cross Sections of Fast Heavy Ions Penetrating through Gaseous and Solid Media // Rev. Mod. Phys. 1972. V. 44, No. 3. P. 465–539.

69. *Nordlund K. et al.* Defect Clustering during Ion Irradiation of GaAs: Insight from Molecular Dynamics Simulations // J. Appl. Phys. 2001. V. 90, No. 4. P. 1710–1117.

70. *Yoshiie T., Kiritani M.* Destination of Point Defects and Microstructural Evolution under Collision Cascade Damage // J. Nucl. Materials. 1999. V. 271/272. P. 296–300.

71. *Bocquet J. L., Doan N. V., Martin G.* A New Formulation of Sink Strengths under Steady Irradiation: Recombination and Interference Effects // Philos. Mag. 2005. V. 85, Nos. 4–7. P. 559–567.

72. *Doan N. V., Martin G.* Elimination of Irradiation Point Defects in Crystalline Solids: Sink Strengths // Phys. Rev. B. 2003. V. 67. Art. No. 134107.

73. *Ishino S.* A Review of *in situ* Observation of Defect Production with Energetic Heavy Ions // J. Nucl. Materials. 1997. V. 251. P. 225–236.

74. *Ohtsuka H. et al.* Radiation Defects in Nanostructured Materials // Eur. Phys. J. D. 2001. V. 16. P. 309–311.

75. *Rayleigh J. S. W.* On the Stability of Jets // Proc. of the London Math. Soc. 1878. V. 10. P. 4–13.

76. *Toimil Molares M. E. et al.* Fragmentation of Nanowires Driven by Rayleigh Instability // Appl. Phys. Lett. 2004. V. 85, No. 22. P. 5337–5339.

77. *Kolb F. M. et al.* On the Morphological Instability of Silicon/Silicon Dioxide Nanowires // Appl. Phys. A. 2005. V. 80. P. 1405–1408.

78. *Komarov F. et al.* Peculiarities of the Track Formation in InP and GaAs Crystals // Vacuum. 2005. V. 78 P. 353–359.

79. *Nicholas F. A., Mullins W. W.* Surface-Interface and Volume Diffusion Contributions to Morphological Changes Driven by Capillary // Trans. of the Amer. Inst. of Mining, Metallurg. and Petrol. Engin. 1965. V. 233, No. 10. P. 1840.

80. *Thompson P. C. et al.* Shock Wave Generation in Thin Foils Using Lasers and Ion Beams // J. Phys. D: Appl. Phys. 1981. V. 14. P. 1215–1223.

81. *Bringa E. M. et al.* Metals Far from Equilibrium: From Shocks to Radiation Damage // Nucl. Instr. Meth. B. 2003. V. 202. P. 56–63.

82. *Weber W. J.* Models and Mechanisms of Irradiation-Induced Amorphization in Ceramics // Nucl. Instr. Meth. B. 2000. V. 166/167. P. 98–106.

83. *Hecking N., Heidemann K. F., Kaat E. T.* Model of Temperature-Dependent Defect Interaction and Amorphization in Crystalline Silicon during Ion Irradiation // Nucl. Instr. Meth. B. 1986. V. 15. P. 760–764.

84. *Ridgway M. C. et al.* Solid Phase Epitaxial Growth of Amorphized InP // Appl. Phys. Lett. 1991. V. 58, No. 5. P. 487–489.

85. *Turos A. et al.* Damage Buildup and Recovery in III–V Compound Semiconductors at Low Temperatures // Nucl. Instr. Meth. B. 2005. V. 1–2, No. 240. P. 105–110.

86. *Srivastava P. C., Ganesan V., Sinha O. P.* AFM Study of Swift Gold Ion Irradiated Silicon // Nucl. Instr. Meth. B. 2002. V. 187, No. 2. P. 20–230.

87. *Srivastava P. C., Ganesan V., Sinha O. P.* AFM Studies of Swift Heavy Ion-Irradiated Surface Modification in Si and GaAs // Rad. Meas. 2003. V. 36, No. 1–6. P. 671–674.

88. *Srivastava P. C., Ganesan V., Sinha O. P.* Evidence of Plastic Flow and Recrystallization Phenomena in Swift ($\sim$ 100 MeV) Si^{+7} Ion-Irradiated Silicon // Nucl. Instr. Meth. B. 2004. V. 222, Nos. 3–4. P. 491–496.

89. *Klaumunzer S., Shumacher G.* Dramatic Growth of Glassy $Pd_{80}Si_{20}$ during Heavy-Ion Irradiation // Phys. Rev. Lett. 1983. V. 51, No. 21. P. 1987–1990.

90. *Hou M., Klaumunzer S., Shumacher G.* Dimensional Changes of Metallic Glasses during Bombardment with Fast Heavy Ions // Phys. Rev. B. 1989. V. 41, No. 2. P. 1144–1157.

91. *Singh J. P.* Scanning Probe Microscopic Studies of Swift Heavy Ion Irradiated Semiconducting and Semimetallic Surfaces. Ph.D. Thesis. Jawaharlal Nehru Univ., 2001.

92. *Volkert C. A.* Stress and Plastic Flow in Si during Amorphization by Ion Bombardment // J. Appl. Phys. 1991. V. 70, No. 7. P. 3521–3527.

93. *Volkert C. A., Polman A.* Radiation-Enhanced Plastic Flow of Covalent Materials during Ion Irradiation // Materials Research Symp. Proc. 1992. V. 235. P. 3–14.

94. *Cliché L., Roorda S., Masut R. A.* Viscosity of Amorphous InP during Room Temperature Structural Relaxation // Nucl. Instr. Meth. B. 1996. V. 96, Nos. 1–2. P. 319–322.

95. *Bhadra R. et al.* Elastic Properites of Si during Amorphization // Phys. Rev. B. 1998. V. 38, No. 17. P. 12656–12659.

96. *Demkowicz M. J., Argon A. S.* High-Density Liquid-Like Component Facilitates Plastic Flow in Model Amorphous Silicon System // Phys. Rev. Lett. 2004. V. 93, No. 2. Art. No. 025505.

97. *Clichér L., Roorda S., Masut R. A.* Persistent Room-Temperature Relaxation of InP Amorphized and Compacted by MeV Ion Beams // Appl. Phys. Lett. 1994. V. 65, No. 14. P. 1754–1756.

98. *Chicoine M. et al.* Directional Effects during Ion Implantation: Lateral Mass Transport and Anisotropic Growth // Phys. Rev. B. 1997. V. 56, No. 3. P. 1551–1560.

99. *Hedler A., Klaumunzer S., Wesch W.* Amorphous Silicon Exhibits a Glass Transition // Nature Materials. 2004. V. 3. P. 804–809.

100. *Van Dillen T. et al.* Ion Beam-Induced Anisotropic Plastic Deformation of Silicon Microstructures // Appl. Phys. Lett. 2004. V. 84, No. 18. P. 3591–3593.

101. *Singh J. P. et al.* Nanoscale Defect Formation on InP Surface by Swift Gold Ion Impact // Nucl. Instr. Meth. B. 2001. V. 179. P. 37–41.

102. *Schmuki P. et al.* Surface Topography of GaAs (100) after Focused Ion Beam Implantation of Si^{++} // Appl. Phys. Lett. 1997. V. 70, No. 10. P. 1305–1307.

103. *Singh J. P. et al.* Temperature-Dependent Roughness of Electronically Excited InP Surfaces // J. Appl. Phys. 2001. V. 90, No. 12. P. 5968–5972.

104. *Didyk A. Yu., Dmitriev S. N., Vutsadakis V.* Spatial Overlapping of Holes in Nuclear-Track Membranes with Different Angular Distributions // High Energy Chem. 2003. V. 37, No. 2. P. 89–95.

105. *Gibbons J. F.* Ion Implantation in Semiconductors. II. Damage Production and Annealing // Proc. of the Inst. of Electrical and Electronics Engin. 1972. V. 60, No. 9. P. 1062–1096.

106. *Colin J., Lesueur D., Grilhe J.* Free Surface Deformation of Irradiated Solids // Philos. Mag. A. 2001. V. 81, No. 4. P. 857–866.

107. Glassy Metals II. Topics in Applied Physics / Eds.: Beck H., Guntherdot H. J. V. 53. Berlin: Springer Verlag, 1983.

108. *Brazhkin V. V., Broughton J. Q., Wooten F.* On the Nature of Amorphous-to-Amorphous and Crystal-to-Amorphous Transitions under High Pressure // J. Noncrystalline Solids. 1997. V. 212. P. 49–54.

109. *Feldman J. L., Broughton J. Q., Wooten F.* Elastic Properties of Amorphous Si and Derived Debye Temperatures and Grüneisen Parameters: Model Calculation // Phys. Rev. B. 1991. V. 43, No. 3. P. 2152–2158.

110. *Kluge M. D., Ray J. R.* Elastic Constants and Density of States of a Molecular-Dynamics Model of Amorphous Silicon // Phys. Rev. B. 1988. V. 37, No. 8. P. 4132–4136.

111. *Mathioudakis C., Kelires P. C.* Softening of Elastic Moduli of Amorphous Semiconductors // J. Noncrystalline Solids. 2000. V. 266/269. P. 161–165.

112. *Brazhkin V. V. et al.* Elastic Softness of Amorphous Tetrahedrally Bonded GaSb and $(Ge_2)_{0.27}(GaSb)_{0.73}$ Semiconductors // Phys. Rev. B. 1997. V. 56, No. 3. P. 990–993.

113. *Testardi L. R., Hauser J. J.* Sound Velocity in Amorphous Ge and Si // Solid State Commun. 1977. V. 21, No. 11. P. 1039–1041.

114. *Sharma R. P. et al.* Crystalline to Amorphous Transformation in GaAs during Kr Ion Bombardment: A Study of Elastic Behavior // J. Appl. Phys. 1989. V. 66, No. 1. P. 152–155.

115. *Zuk J., Kiefte H., Clouter M.* Investigation of Ion-Implanted GaP Layers by Brillouin Scattering // J. Appl. Phys. 1993. V. 73, No. 10. P. 4951–4954.

116. *Didyk A. Yu.* Radiation Influence of Heavy Ions on Chromium-Nickel Steel at High Temperature // Metals. 1995. No. 3. P. 128–135 (in Russian).

117. *Yavlinskii Yu. N.* Track Formation in Amorphous Metals under Swift Heavy-Ion Bombardment // Nucl. Instr. Meth. B. 1998. V. 146. P. 142–146.

118. *Toulemonde M., Dufour C., Paumier E.* Transient Thermal Process after a High-Energy Heavy-Ion Irradiation of Amorphous Metals and Semiconductors // Phys. Rev. B. 1992. V. 46, No. 22. P. 14362–14369.

119. *Vlasukova L. A. et al.* Peculiarities of Surface Structure Changes in Single Crystals InP and GaAs, Irradiated with High Energy Electrons and Ions // Izv. of RAS. Ser. Phys. 2006. V. 70, No. 8. P. 1178–1181 (in Russian).

120. *Vlasukova L. A. et al.* Changes of Surface Structures in GaAs, Irradiated with High-Energy Electrons and ^{86}Kr Ions // J. Surface Investigations. X-ray, Synchrotron and Neutron Techniques. 2006. No. 8. P. 34–40 (in Russian).

121. *Vlasukova L. A. et al.* Influence of Electron and Krypton Heavy-Ion Irradiation on Swelling and Sputtering of InP Single Crystal // Ibid. No. 1. P. 50–58 (in Russian).

122. *Amirkhanov I. V. et al.* Sputtering of Solids by Heavy Ions and Temperature Effects in Electronic and Lattice Subsystems // Part. Nucl. 2006. V. 37, No. 6. P. 837–866.

123. *Amirhanov I. V. et al.* Investigation of Heat Processes in Materials under Irradiation by Swift Heavy Ions in Frame of General Thermal Spike Model // Crystallog. Rep. 2006. No. 51, Suppl. 1. P. S32–S43.

124. *Didyk A. Yu. et al.* Surface Structure Changes of InP and GaAs Single Crystals Irradiated with High-Energy Electrons and Swift Heavy Ions // Nukleonika. 2006. V. 51, No. 2. P. 105–109.

125. *Didyk A. et al.* Structure Changes in InP and GaAs Crystals Irradiated with Electrons and Swift Heavy Ions // Vacuum. 2007. V. 81. P. 1175–1179.

126. *Khalil A. S. et al.* Surface Modifications by Swift Heavy Ion Irradiation of Indium Phosphide // Part. Nucl., Lett. 2008. V. 5, No. 5(147). P. 481–487.

127. *Didyk A. Yu. et al.* Damage Distribution in GaAs Single Crystal Irradiated with ^{84}Kr (394 MeV), ^{209}Bi (710 MeV), and ^{238}U (1300 MeV) Swift Ions // Nukleonika. 2008. V. 53, No. 2. P. 77–82.

128. *Herre O. et al.* // Phys. Rev. B. 1998. V. 58. P. 4832.

129. *Gaiduk P. I., Komarov F. F., Wesch W.* // Nucl. Instr. Meth. B. 2000. V. 164–165. P. 377.

130. *Biersack J. P., Haggmark L. G.* // Nucl. Instr. Meth. B. 1980. V. 174. P. 257.

131. *Baranov I. A. et al.* Inelastic Sputtering of Solids by Ions // Usp. Fiz. Nauk. 1988. V. 156, No. 3. P. 476–511 (in Russian).

132. *Wang Z. G. et al.* The S_e Sensitivity of Metals under Swift-Heavy-Ion Irradiation: A Transient Thermal Process // J. Phys.: Condens. Matter. 1994. V. 6. P. 6733–6750.

133. *Baranov I. et al.* Sputtering of Nanodispersed Targets of Gold and Desorption of Gold Nanoclusters (2–100 nm) 6 MeV Au_5 Cluster Ions // Nucl. Instr. Meth. B. 2002. V. 193. P. 809–815.

134. *Zhernov A. P., Inyushkin A. V.* // Usp. Fiz. Nauk. 2002. V. 172. P. 573 (in Russian).

135. *Smentkowski V. S.* Trends in Sputtering // Progress in Surface Science. 2000. V. 64. P. 1–58.

136. *Sigmund P.* Sputtering by Ion Bombardment: Theoretical Concepts // Sputtering by Particle Bombardment. 1. Physical Sputtering of Single Element Solids / Ed. R. Behrisch N. Y., 1981. Ch. 2.

137. *Sigmund P., Claussen C.* Sputtering from Elastic-Collision Spikes in Heavy-Ion-Bombarded Metals // J. Appl. Phys. 1981. V. 52, No. 2. P. 990–993.

138. *Yavlinskii Yu. N.* // Rad. Effects and Def. in Solids. 2000. V. 153. P. 75–91.

139. *Chadderton L. T., Biersack J. P., Koul S. L.* Discontinues Fission Tracks in Crystalline Detectors // Nucl. Tracks and Rad. Meas. 1988. V. 15. P. 31176.

140. *Cruz S. A. et al.* A Simple Model for Latent Track // Rad. Meas. 2003. V. 36. P. 145.

141. *Arista A. N. R.* Stopping Power of Molecules and Clusters // Nucl. Instr. Meth. B. 2000. V. 164. P. 108–138.

142. *Linnors J., Elliman R. G., Brown W. L.* Divacancy Control of Balance between Ion Beam Induced Epitaxial Crystallization and Amorphization of Si // J. Materials Res. 1988. V. 3. P. 1208–12011.

143. *Chadderton L. T., Johnson E., Wohlenberg T.* Observation of a Regular Void Array in Natural Fluorite Irradiated with 100 keV Electrons // Physica Scripta. 1976. V. 13. P. 127.

144. *Chadderton L. T., Johnson E., Wohlenberg T.* A Mechanism for the Formation of an Ordered Void Array on the Anion Sublattice in Fluorite // Rad. Effects. 1976. V. 28. P. 111.

145. *Chadderton L. T., Johnson E., Wohlenberg T.* Void Lattices // Comments on Solid State Phys. 1976. V. 7. P. 125.

146. *Chadderton L. T., Johnson E., Wholenberg T.* Void Lattices in Fluorite // Micron. 1980. V. 11. P. 247.

147. *Johnson E., Chadderton L. T.* Anion Voidage and the Void Superlattice in Electron Irradiated Ca F_2 // Rad. Effects. 1983. V. 79. P. 183–223.

148. *Foreman J.* AERE Harwell Report. AERE R-7135. 1972.

149. *Fleischer R. L.* Are Tracks Caused by Thermal Spikes? // Intern. Nucl. Track Soc. Newslett. 2005. V. 5, No. 2. P. 3–4.

150. *Yang X. et al.* Low Energy Electron-Beam-Induced Recrystallization of Continuous GaAs Amorphous Foils // Materials Sci. and Engin. B. 1997. V. 49. P. 5–13.

151. *Chadderton L. T.* Tracks and Thermal Spikes: A Comment // Intern. Nucl. Track Soc. Newslett. 2006. V. 6, No. 1. P. 8–11.

152. *Chadderton L. T.* Track Formation // On Track: The Newsletter of Intern. Fission-Track Community. 2000. V. 10, No. 21. P. 5–8.

153. *Szenes G.* Information Provided by a Thermal Spike Analysis on the Microscopic Processes of Track Formation // Nucl. Instr. Meth. B. 2002. V. 191. P. 54–58.

154. *Szenes G.* Thermal Spike Model of Amorphous Track Formation in Insulators Irradiated by Swift Heavy Ions // Nucl. Instr. Meth. B. 1996. V. 116. P. 141–144.

155. *Szenes G.* Thermal Spike Analysis of Latent Track Formation in Magnetic Insulators // Rad. Meas. 1995. V. 25, Nos. 1–4. P. 39–42.

156. *Chadderton L. T., Torrens I.* Fission Damage in Crystals. London: Methuen, 1969.

157. *Gallagher K., Brown R., Johnson C.* Fission Track Analysis and Its Application to Geological Problems // Ann. Rev. of Earth and Planetary Sci. 1998. V. 26. P. 519–572.

158. *Tagami T., O'Sullivan P. B.* Fundamentals of Fission-Track Thermochronology // Rev. in Mineralogy and Geochem. 2005. V. 58. P. 19–47.

159. *Vidal O., Wendt A., Chadderton L. T.* Experimental Evidence for the Pressure Dependence of Fission Track Annealing in Apatite // Earth and Planetary Sci. Lett. 2002. V. 201. P. 593–607.

160. *Vidal O., Wendt A., Chadderton L. T.* Further Discussion on the Pressure Dependence of Fission Track Annealing in Apatite: Reply to the Critical Comment of Kohn et al. // Earth and Planetary Sci. Lett. 2003. V. 215. P. 307–316.

161. *Jaskierowicz G., Dunlop A., Jonckheere R.* Track Formation in Fluoroapatite Irradiated with Energetic Cluster Ions // Nucl. Instr. Meth. B. 2004. V. 222. P. 213–227.

162. Reproduced with kind permission of Dr. A. Dunlop and Prof. L. Chadderton.

163. *Jensen J., Dunlop A., Della-Negra S.* Tracks Induced in CaF_2 Induced by MeV Cluster Irradiation // Nucl. Instr. Meth. B. 1998. V. 141. P. 753–762.

164. *Jensen J., Dunlop A., Della-Negra S.* Microscopic Metallic Inclusions Generated along the Path of Clusters in CaF_2 // Ibid. V. 146. P. 399–404.

165. *Ziegler J. F., Biersack J. P., Littmark U.* The Stopping and Range of Ions in Solids. Ser. «Stopping and Ranges of Ions in Matter». N. Y.: Pergamon Press, 1984. V. 1.

166. http://www.srim.org

167. *Nishino K. et al.* Intensity Measurements of Equal-Thickness Fringes in TEM Images of Wedged-Shaped GaAs and InP Crystals by a Slow-Scan CCD Camera // J. Electron Microscopy. 1994. V. 43. P. 198–202.

168. *Jocnkoheer R.* Personal Commun. to L. T. Chadderton and A. Khalil.

169. *Claderin L., Stott M. J., Rubio A.* Electronic and Crystallographic Structure of Apatites // Phys. Rev. B. 2003. V. 67. P. 134106.

170. *Hughes J. M., Cameron M., Crowley K. D.* Crystal Structure of Natural Ternary Apatite: Solid Solutions in the $Ca_5(PO)_4X$ (X = F, Cl, OH) System // Amer. Mineralogist. 1990. V. 75. P. 295–304.

171. *McConnell D.* Apatite: Its Crystal Chemistry, Mineralogy, Utilization, and Geological and Biological Occurrences. N. Y.: Springer Verlag, 1973.

172. *Paul T. A., Fitzgerald P. G.* Transmission Electron Microscopic Investigation of Fission Tracks in Fluoroapatite // Amer. Mineralogist. 1992. V. 77. P. 336–344.

173. *Popok V. N., Prasalovich S. V., Campbell E. E. B.* Complex Crater Formation on Silicon Surfaces by Low-Energy Ar_n^+ Cluster Ion Implantation // Surface Sci. 2004. V. 566/568. P. 1179–1184.

174. *Majumdar B., Chattopadhyay K.* The Rayleigh Instability and the Origin of Rows of Droplets in the Monotectic Microstructure of Zinc–Bismuth Alloys // Metallurg. and Materials Trans. A. 1996. V. 27. P. 2053–2057.

175. *Karim S. et al.* Morphological Evolution of Au Nanowires Controlled by Rayleigh Instability // Nanotechnology. 2006. V. 17. P. 5954–5959.

176. *Muller T., Heinig K. H., Schmidt B.* Template-Directed Self-Assembly of Buried Nanowires and the Pearling Instability // Materials Sci. and Engin. C. 2002. V. 19. P. 209–213.